UNIVERSITAS BERGENSIS

DEPARTMENT OF PHYSICS AND TECHNOLOGY

Master Thesis in Nuclear Physics

Thermal Neutron Detection Efficiency of a Gadolinium-Based Silicon Pixel Sensor

---

Author: Lena Setterdahl
Supervisor: Dieter Roherich
Co-supervisors: Ganesh Tambave & Pierluigi Piersimoni

November 20, 2020

Abstract

Well acquainted with charged particle tracking, ALPIDE's potential in the field of neutron detection has yet to be explored. ALPIDE is a silicon semiconductor sensor designed for particle-tracking in high energy particle physics experiments, explicitly developed to upgrade the Inner Tracking System (ITS) part of the ALICE experiment CERN. ALPIDE's charged particle detection efficiency exceeds 99.99%.

By combining a particle sensor (such as ALPDIE) with a neutron converter, neutrons can be detected indirectly. Among solid-state neutron converters, the highest neutron detection has been observed with gadolinium (Gd) because of its exceptionally high neutron-capture cross-section.

This thesis is a "proof-of-principle" study which aims to assess the feasibility of ALPIDE as a neutron imaging sensor when coupled with a natural-Gd converter foil. The neutron detection efficiency of a Gd-based ALPIDE scheme was calculated based on experimentally collected and simulated data.

With the Monte Carlo simulation toolkit Geant4, the Gd-based ALPIDE scheme was simulated in a thermal-neutron flux. Numerous simulations were performed where the scheme's and neutron source's features were slightly modified to study parameters of the neutron detection efficiency. Achieved with a back-irradiated thinned-down ALPIDE exposed to a thermal-neutron beam, the highest simulated detection efficiency was 18%. The lowest simulated detection efficiency was 5%, and achieved with a standard ALPIDE chip exposed to an isotropic thermal-neutron flux.

Experimental data was collected in an approximately isotropic mixed-energy neutron and gamma flux, which included thermal neutrons. The thermal neutrons were obtained by thermalizing (with plastic blocks) the fast-neutron flux of a F-18 producing PET (Positron Emission Tomography) cyclotron. The Neutron Survey Meter A480 performed control measurements of the thermal-neutron (and fast-neutron) flux (count). Two methods were used to calculate the neutron detection efficiency of the Gd-based ALPIDE setup. The experimentally obtained neutron detection efficiency of the Gd-based ALPIDE was (3.19±0.01)% and (1.50±0.05)%.

The "proof-of-principle" study confirmed neutron detection possible with the Gd-based ALPIDE.

Acknowledgements

I would first like to thank my supervisors, professor Dieter Roherich, doctor Pierluigi Piersimoni and doctor Ganesh Tambave for their support and guidance.

Thank you Dieter, for providing me with this incredibly interesting project. It has made this year one of great learning.

I wish to show my gratitude to Pierluigi and Ganesh, for always having an open door I can pop my head through. Words cannot begin to describe how grateful I am for the helpful and engaging conversations we've had this year.

I am indebted to everyone who so generously gave their time to guide me through the difficult and consuming task of simulations. A special thanks goes to the Geant4 collaboration, who helped solve one of the great head scratchers of this study.

Thank you to all my peers, for the multiple years we have shared at the university together. A special mention to Minh Chi, Emilie and Ingrid, who have been there with and for me from the very start.

Finally, I must express my profound gratitude to my parents, Stephan Setterdahl and Kristin Setterdahl, who have provided me with unconditional love and unwavering support throughout my life. They sparked a joy for the natural sciences and math at a very young age that has only grown stronger with the years. I would not be where I am today without them.

Citation Principles

The citation principles of this thesis are as follows: Citations listed before any punctuation will always refer to the last statements. Those listed after the ending punctuation of a paragraph may refer to several statements in the section.

Contents

List of Figures

List of Tables

Chapter 1

Introduction

The importance of neutron detection has grown considerably in the last decade, due to the availability of high-intensity spallation neutron sources for material science and biochemical imaging. Electrically neutral, neutrons do not participate in ionizing processes, which tends to be a fundamental principle of radiation detectors. However, combining a radiation detector with a neutron sensitive material in which neutrons induce ionizing radiation allows the detector to observe neutrons indirectly. [1]

He-3 is the most popular conversion material of neutron counters found on the market [2]. For many years the supply of He-3 outweighed its demand. After the terrorist attack of 11/09/01, border security against smuggled nuclear and radiological material increased, and so did the demand for neutron detectors and He-3. At the same time, medical applications requested He-3 for the polarized He-3 medical imaging technique. The size of He-3 stockpiles dwindled and resulted in a worldwide shortage, which severely affected the cost of He-3. The need for alternative methods to He-3 proportional counters has, therefore, become a leading matter of research in contemporary nuclear instrumentation. [3]

Gadolinium (Gd) is a possible alternative conversion material. At a cost approximately 30 times lower, Gd is significantly cheaper then He-3 [2]. It also possesses other characteristics desirable in a neutron converter material, such as a high reaction energy and a high thermal neutron capture cross-section [2]. A high reaction value ensures that reaction products are energetic enough to escape the converter material and deposit a meaningful amount of energy in the detector's sensor. A high neutron capture cross-section increases neutron detection probability and is an essential parameter of a detector's neutron detection efficiency. Other desirable traits of converter materials are low gamma sensitivity, low stopping power in the eyes of reaction products, and reaction products with a characteristic energy spectrum. A high neutron-capture cross-section is useless if the reaction products cannot escape the converter foil. [1]

Gd-neutron capture displays one of the highest observed thermal-neutron capture cross-section than any known stable isotope. With its cross-section of 48800 barns (9 times greater than He-3), sufficient neutron capture and escape of reaction products are achievable with a few μm of Gd. Gd-neutron capture's reaction products are promptly-emitted gamma rays and internal conversion electrons (ICEs). The prompt-gamma rays have energies up to 8 MeV, and the ICEs have discrete energies up to hundreds of keV. Byproducts of ICE emission are x-rays and Auger electrons which have discrete energies up to tens of keVs. The energy spectrum of the reaction products feature peaks characteristic of neutron capture in Gd and can be exploited to detect neutrons. [2]

Another active topic of research in radiation detection is the evolution of light, portable detectors. Semiconductor detectors are superb candidates in this context, with high density and photon attenuation of dense solids, restricting the volume needed for neutron-induced particles to generate a signal. Thanks to their high stopping power, they have an excellent energy resolution and, combined with a Gd converter foil, they can be used to classify the characteristic peaks associated with Gd-neutron capture. [2]

ALPIDE is a semiconductor particle sensor developed for high energy physics (HEP) experiments at CERN. ALPIDE has a high charged particle detection efficiency (99.99%) [4]. Mostly used for charged particle tracking, ALPIDE's potential as a neutron detector is undocumented. In theory, coupling ALPIDE with a Gd converter foil would make it sensitive to neutrons. This thesis is a "proof-of-principle" study that demonstrates ALPIDE's feasibility as a neutron detector. The setup's concept was for the foil to convert thermal neutrons into radiation the ALPIDE could detect. By knowing the number of thermal neutrons absorbed in the foil and the number of neutrons detected due to ICEs detection, the neutron detection efficiency could be calculated. The application of ALPIDE as a neutron imaging sensor for European Spallation Senter (ESS) was kept in mind.

The thesis is structured as follows: **Chapter 1** gives a brief introduction on the topic of neutron detection, Gd as a neutron converter material, and the thesis' objective. **Chapter 2** presents the radiation physics deemed necessary to understand the fundamental processes that take place inside a Gd-based neutron detector, which includes neutron, electron and gamma interactions with matter. Chapter 2 also presents the general working of semiconductors and introduces ALPDIE, the semiconductor used in this thesis. **Chapter 3** is dedicated to Gd-neutron capture, the main topic of this thesis. **Chapter 4** presents simulation studies and **Chapter 5** presents a physical experiment with a

Gd-based ALPIDE neutron detection scheme. **Chapter 6** discusses and interprets the results of the simulation studies and the experiment. Lastly, **Chapter 7** concludes the thesis study.

Chapter 2

Background

Knowing how and which interactions take place inside a detector makes it possible to predict its response to radiation as well as interpreting its measurements. For a Gd-based neutron detector, particles of interest are first and foremost neutrons and secondly, reaction products of Gd-neutron capture, electrons and photons. This chapter gives an introduction to neutron, electron and photon interactions with matter, providing a ground understanding of the fundamental physics which may occur around and within the neutron detection scheme in question. The last two sections of the chapter give an introduction to semiconductor detectors and a description of ALPIDE.

2.1 Particle Penetration in Matter

There are several ways to describe the distance a particle travels in a material. The three distance concepts referred to in this thesis will be mean-free-path, projected range, and Continuous-Slowing-Down-Approximation (CSDA) range. All three depend on particle energy and material properties. Consider the case depicted in Figure 2.1 where a particle enters a material, experiences n scattering events before eventually stopping in the material.

The **mean-free-path** X_m of the particle is defined as the average distance it travels between scattering points. That is, the mean of all the straight-lined paths along which the particle is free of interactions.

$$X_m = \frac{x_1 + x_2 + \cdots + x_n}{n} \tag{2.1}$$

The mean-free-path concept is useful when discussing particles prone to absorption and

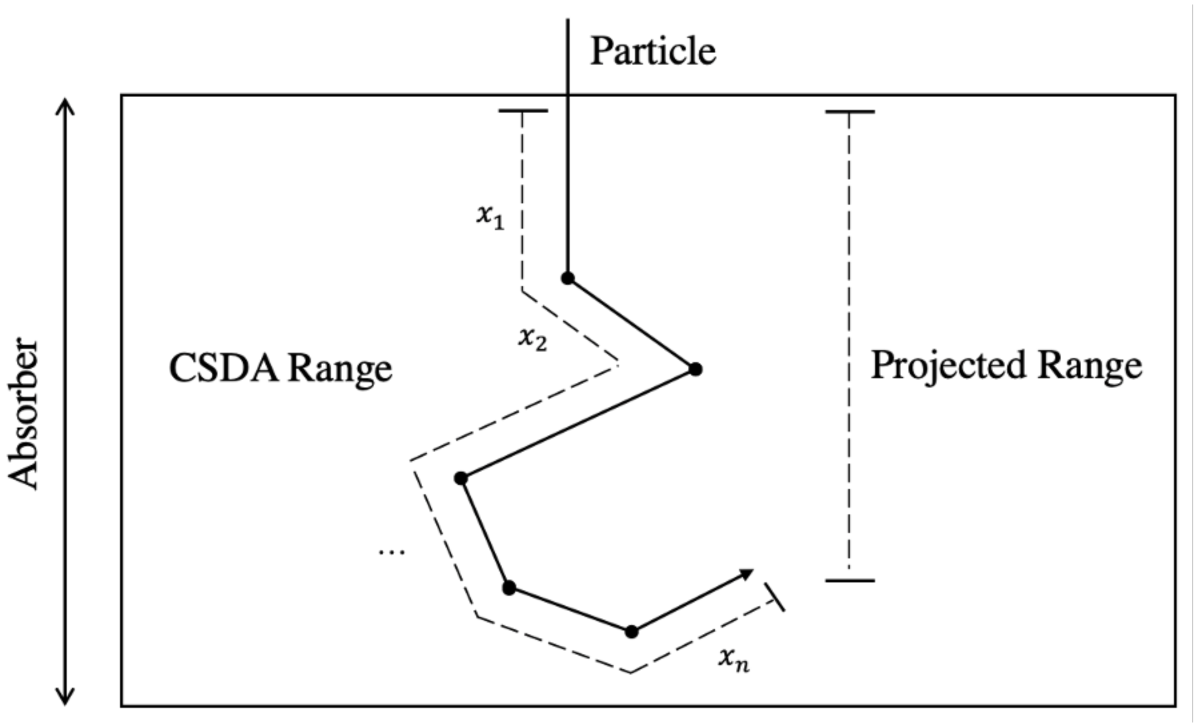

Figure 2.1: Distances used to describe a charged particle entering an absorbing material scattering x_n times before stopping. Also applicable for neutrons, as they behave similarly.

calculating particles' absorption probability in a material (2.2.4).

The particle's **projected range** is the depth the particle reaches as it comes to a halt in the absorber [5]. It is the absolute distance traveled by the particle in the absorber and is measured along the particle's initial direction. It can be experimentally determined by firing a beam of particles at the desired energy through different absorbing material thicknesses and measuring the fraction of transmitted to incident particles [6].

CSDA range describes the average path length traveled by the particle in the absorber material. Assuming continuous energy loss and thus continuous slowing down, integrating over average energy loss dE/dx (see Bethe-Bloch in subsection 2.3.1) gives the particle's CSDA range [5]. Typically, CSDA is given in units g/cm^2 (distance per material density unit) but can easily be converted into cm by dividing by the material density ρ.

$$CSDArange[cm] = \frac{CSDArange[g/cm^2]}{\rho[g/cm^3]} \tag{2.2}$$

While the CSDA range gives information on the total distance traveled by the particle, it does not reveal how deep the particle penetrates (like the projected range). In the case of a few scattering events, the CSDA range is a good approximate to the projected range. However, if the particle experiences multiple scattering events (section 2.3.3), the CSDA range is greater than the projected path.

2.2 Neutron Interactions With Matter

Neutrons are subatomic particles with zero net charge and a mass comparable to that of a proton. A single neutron constitutes three quarks, one up and two down. The composite quarks cause the neutron's lack of electric charge, the positive charge of its up quark ($+2/3e^1$) cancels the negative charge of its two down quarks (2x-1/3e).

Due to lack of charge, neutrons interact with matter mostly via nuclear interactions. Figure 2.2 lists the different types of interactions a neutron can have with matter. For this thesis, the most interesting neutron interactions are elastic scattering, inelastic scattering, and radiative capture. The following subsections provide a comprehensive introduction to these processes. This chapter does not cover the less relevant interactions fission, charged particle emission, and neutron emission, as these do not strictly relate to the thesis' topic.

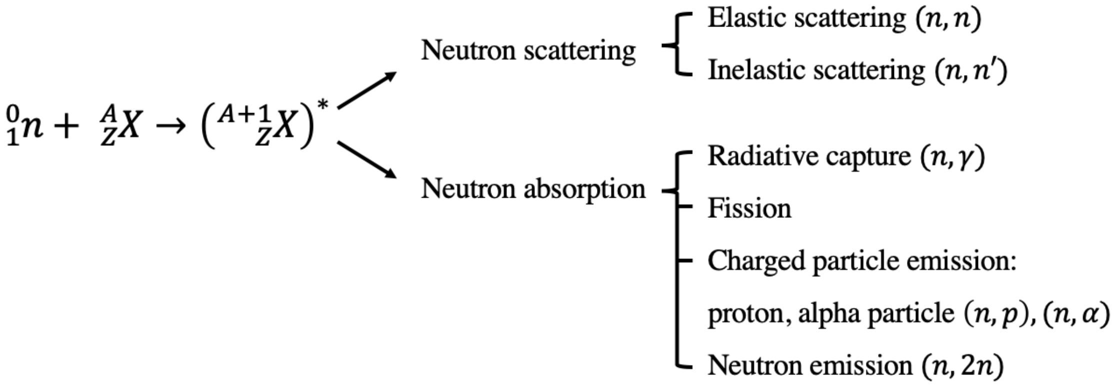

Figure 2.2: Neutron interactions with matter. Reproduced from [7]

2.2.1 Elastic Scattering (n, n)

Since a neutron's net charge is zero, it does not have to overcome any Coulomb barrier. This allows even low energy neutrons to get very close to a nucleus and scatter elastically off of it. Elastic scattering changes neutron trajectory while conserving the combined neutron and nucleus kinetic energy. Figure 2.3 depicts the cross-section of elastic scattering for materials of various atomic mass. The elastic cross-section categorizes into two types of scattering: potential and resonance.

Resonance scattering is the less common of the two and depends on incident neutron energy. Depicted in Figure 2.4a, the process involves a nucleus absorbing and re-emitting

---

[1] e: elementary charge = 1.602·10^{-19} C

a neutron, not necessarily the same neutron. The neutron kinetic energy is the same before and after the event, but the emitted neutrons' velocity vector points in a different direction than the incident neutrons'. After absorbing the incident neutron, the nucleus increases its atomic mass by one unit and becomes an excited compound nucleus. For resonance scattering to occur, the incident neutron energy must create the compound nucleus in one of its excited states. It is for these specific neutron energies the elastic cross-section experiences resonance. The energy of the compound nucleus' excited state can be obtained by adding the neutron binding energy and the resonance energy of the target nucleus.

The more common form of elastic scattering is potential. It relates to the elastic cross-section for lower neutron energies, typically below 1 MeV, where a neutron scatters off a nucleus' surface by the short-range nuclear force. The potential cross-section is nearly constant and proportional to the nuclear radius R:

$$\sigma_{el} = 4\pi R^2 \tag{2.3}$$

The scattered neutron alters its direction of motion and transfers a portion of its kinetic energy to the nucleus in the process.

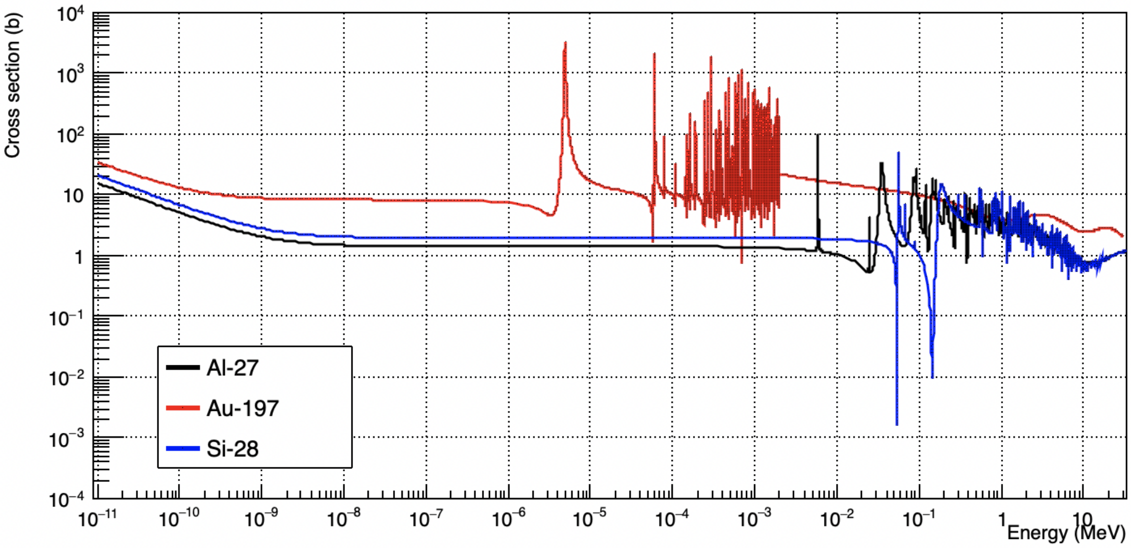

Figure 2.3: Neutron elastic scattering cross-section for nuclei of various atomic mass. Proportional to nuclear radius R, elastic scattering cross-section is higher for Gold (Au-197) than the smaller nuclei, silicon (Si-28), and aluminum (Al-27). Also, because of the larger atomic number, cross-section resonance occurs at lower energies for Au-197. Generated from nuclear data library ENDF/B-VIII.0 [8]

The ratio of the recoil nucleus' energy to the incident neutron energy can be derived by applying the momentum and energy conservation laws of classical mechanics:

$$\frac{\Delta E}{E_N} = 1 - \left(\frac{A-1}{A+1}\right)^2 \tag{2.4}$$

where E_N is the initial neutron energy, ΔE is the recoil energy, and A is the atomic mass number of the target nucleus. From equation 2.4, it is apparent that the energy transfer depends on the number of nucleons (A) inside the nucleus. Inside materials of low atomic mass, neutrons lose significant amounts of energy and are effectively slowed down by elastic scattering. That is why materials such as water and paraffin are often used to slow down and thermalize neutrons.[7]

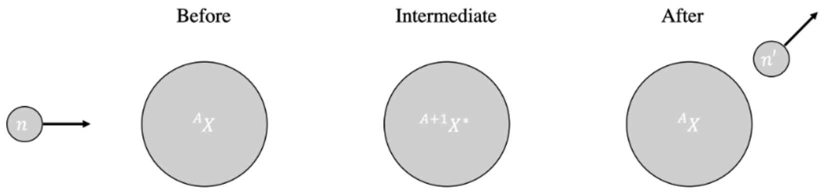

(a) Resonance elastic scattering: a neutron is absorbed and re-emitted. The neutron energy is conserved.

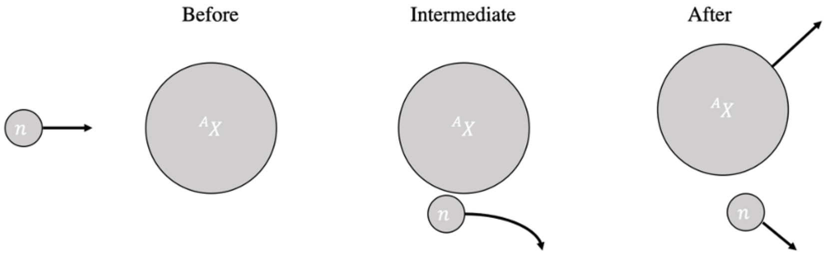

(b) Potential elastic scattering: a neutron scatters of the nuclear surface. The neutron energy is reduced.

Figure 2.4: Neutron scattering. Reproduced and modified from [7].

2.2.2 Inelastic Scattering (n, n')

Inelastic scattering changes neutron kinetic energy. Similar to resonance scattering, inelastic scattering involves absorbing and re-emitting a neutron. Unlike resonance scattering, the emitted neutron of inelastic scattering has a reduced kinetic energy due to the nucleus absorbing some of the incident neutron's energy. The energy transfer excites the compound nucleus, and the nucleus can decay by emitting a neutron and gamma rays. Inelastic scattering depends on incident neutron energy for the same reason as resonance scattering, and the neutron energy must generate a compound nucleus in one of its excited states. In general, heavier nuclei have more energy levels, and the first excited state is lower than for light nuclei [9]. Consequently, the inelastic cross-section is zero up to a certain threshold energy, illustrated in Figure 2.5. Nuclear excitation energy increases with decreasing atomic mass. Because of this, neutrons are more probable of inelastic scattering with heavier nuclei. The minimum excitation energy for high to moderate mass nuclei lie in the range of 0.1-1 MeV and is higher for low mass nuclei. Lighter nuclei like aluminum (Al-27) and silicon (Si-28) display higher energy thresholds than, for instance, gold (Au-197), which has a relatively high atomic number. [7]

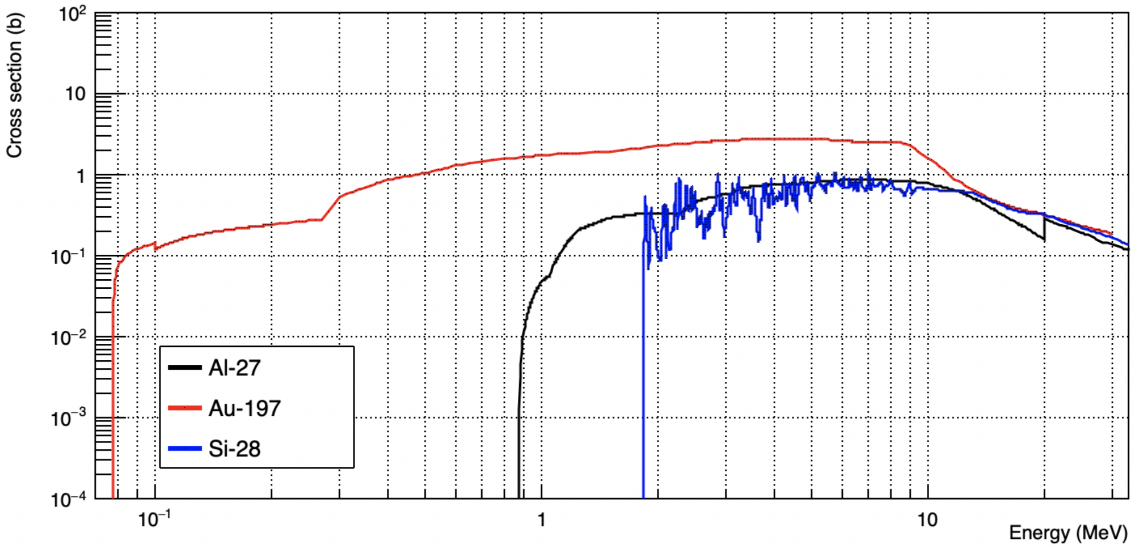

Figure 2.5: Inelastic scattering cross-section of aluminum (Al-27), silicon (Si-28), and gold (Au-197). Higher mass nuclei like gold display a lower threshold energy due to a lower first excitation state. Generated from nuclear data library ENDF/B-VIII.0 [8].

Thermal Neutrons

In matter, neutrons are either scattered, absorbed, or escape the material. In a material that does not absorb neutrons, and assuming that all neutrons remain inside the volume in question, the only interaction possible is scattering. Neutrons experience energy loss with each scatter event, which causes them to slow down. Neutrons with kinetic energy less than the energy corresponding to the materials' thermal motion may gain energy from the collision. When the probability of energy loss is the same as energy gain, the neutrons are in thermal equilibrium. With scattering being the only neutron interaction, the neutrons conform to the atom's thermal motion. The atomic energy follows a Maxwellian-Boltzmann distribution (Maxwellian distribution), and it is useful to assume the same distribution for the thermalized neutrons. The Maxwellian velocity distribution of thermal neutrons per unit volume and unit velocity interval is

$$\frac{n(v)}{n} = \frac{4\pi v^2}{(2\pi kT/m)^{3/2} e^{-mv^2/2kT}} \tag{2.5}$$

where

n: thermal neutron population per unit volume

m: neutron rest mass
T: temperature in K
k: Boltzmann constant

One can express the most probable neutron velocity v_P by setting the derivative of $n(v)$, with respect to neutorn velocity v, equal to zero

$$\frac{dn(v)}{dv} = e^{-\frac{mv^2}{2kT}} \frac{4\pi vn}{(2\pi kT/m)^{3/2}}(2 - \frac{mv}{kT}) = 0 \tag{2.6}$$

so that

$$v_P = \sqrt{\frac{2kT}{m}} \tag{2.7}$$

which corresponds to the most probable neutron energy $E_P = \frac{mv_P^2}{2} = kT$. When speaking of thermal neutrons, room temperature, 20°C (293 K), is typically implied and corresponds to the most probable neutron speed 2200 m/s and energy 0.025 eV. [7]

2.2.3 Radiative Capture (n, γ)

Radiative capture reactions start with the absorption of a neutron and, in most of the reactions, result in the emission of one or several gamma rays. Radiative capture is also referred to as "neutron capture". In a neutron-capture reaction, a nucleus merges with a neutron and forms an excited compound nucleus. The excited nucleus rids itself of excess energy by emitting prompt-gammas rays, as Figure 2.6 illustrates. Radiative capture transpires for neutrons of all energies.

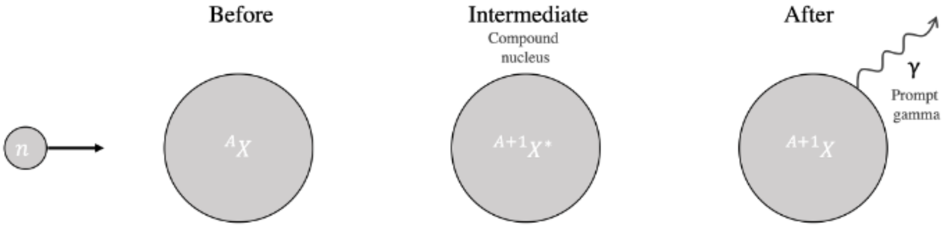

Figure 2.6: Radiative Capture. A neutron-excited nucleus radiating gamma.

The probability of neutron capture depends on neutron energy. As a function of neutron energy, neutron-capture cross-sections indicates three appropriately labeled energy regions: the low-, intermediate- and high-energy region (which Figure 2.7 illustrates). The **low-energy region** ($1/v$-region) extends up to 0.5 eV - also known as the *Cadmium cut-off* energy because of Cadmium's characteristic and sudden drop in cross-section at this

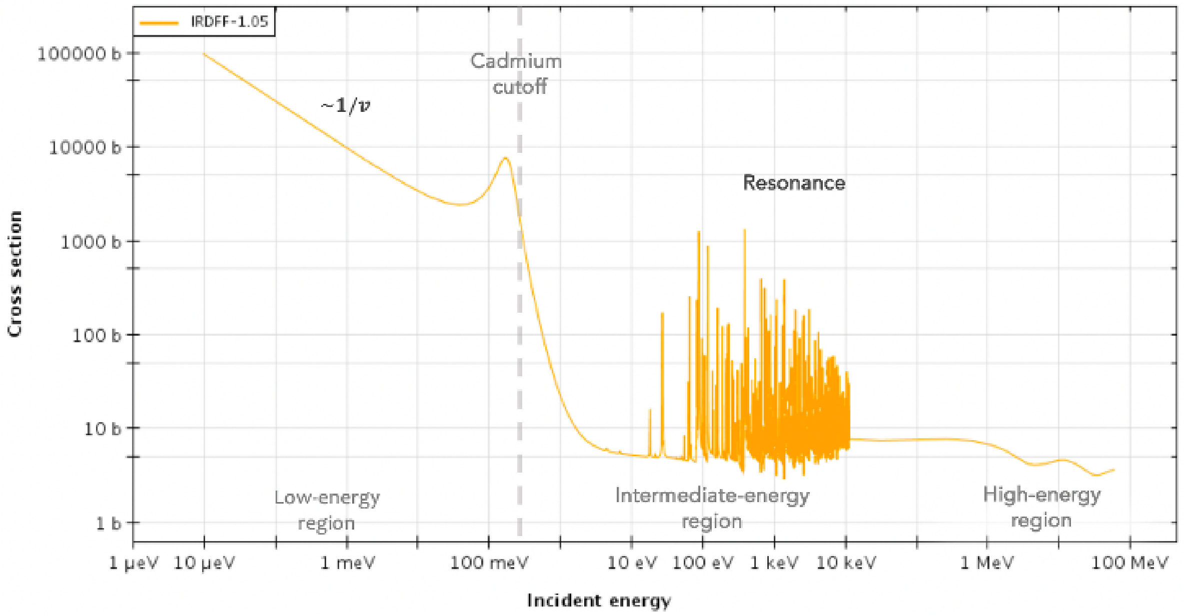

Figure 2.7: Neutron cross-section of Cd-113, from the CENDL-3.2 Nuclear Data Library [8]

value. For most low-energy neutrons, the probability of capture is inversely proportional to the square root of the neutron energy. Since kinetic energy is a function of neutron speed v, this means that σ_γ is proportional to $1/v$. Capture becomes more probable the closer a neutron is and the more time it spends near a nucleus. Slower neutrons take more time to pass the nucleus and are thus more likely captured. The **intermediate-energy region** starts where the low-energy region ends (at 0.5 eV) and stretches up to 100 keV. Spanning over energies for which the cross-section typically experiences resonance, the intermediate-energy region is also known as the resonance-region. The locations of the cross-section's resonance peaks are comparable to the energy levels of the compound nucleus.

The probability of forming a compound nucleus increases drastically when the incident neutron energy results in the compound nucleus being in one of its excited states. The likelihood of neutron capture lessens with higher energies in the **fast-energy region**. The cross-section quickly and continuously drops to smaller values, and the probability of elastic scattering takes over. The majority of neutrons are created with energies of the fast-region (200 keV-20 MeV) and are called fast neutrons. [7]

Once captured, the neutron and its kinetic energy become a part of, and excites, the absorbing nucleus. Wanting to transcend to a more stable state, the excited nucleus releases energy through gamma-ray decay. Gamma transitions are the most probable de-excitation process for a nucleus transitioning from highly energetic states. As the nucleus descends towards lower energy states, a second decay mode, known as internal conversion, becomes increasingly probable. Internal conversions result in the emission of inner-shell electrons. Due to electron vacancies caused by internal conversion, the atom to which the nucleus belongs radiates x-rays and Auger electrons.

Gamma-Ray Decay

An excited nucleus releases one or more gamma rays

$$^{A+1}X^{*} \rightarrow {}^{A+1}X + \gamma \tag{2.8}$$

If only one gamma is emitted, the gamma gains all of the nucleus' excess energy. If several gamma rays are released, the nucleus undergoes multiple gamma transitions before reaching ground state and the emitted gammas take on energies from a few keVs up to several MeVs. The transition energy (E_T) of an intermediate transition is equal to the energy difference in the final and initial nuclear energy state

$$E_T = E_{final} - E_{initial} \tag{2.9}$$

The energy diagram of a hypothetical nucleus and gamma transitions between its energy levels are illustrated in Figure 2.8. Because they are discrete, low-lying levels have a known spin and parity and are easily distinguishable. As the nuclear energy increases, so does the nuclear level density. Highly energetic levels eventually become indistinguishable from one another and resemble a continuum. In the currently discussed figure, the dotted lines mark energy levels within the quasicontinuum, and uninterrupted lines mark levels within the discrete domain. There is no clear boundary between the continuous and discrete domain, but rather a smooth transition between the two [10]. The highest energy level represents neutron-capture state, and the lowest level represents ground state. Neutron-capture and ground state are indicated by bold uninterrupted lines. Arrows indicate transitions from one level to another. A nucleus may transition once or several times before it reaches ground state. Transitions can occur between (1) states in the continuous domain, (2) states in the discrete domain, or (3) between the two. Each energy level features a distinct spin and parity, and during a transition, both must be conserved. Symbols J[2] and π represent spin and parity, respectively, and are usually presented together as spin-parity J^{π}. The parity of the radiated photon is the difference in parity of the initial and final transition states. The initial and final energy state's total angular momentum can be labeled as $J_i\hbar$ and $J_f\hbar$ and change in the spin as $\Delta J = \hbar(J_f - J_i)$. The minimum angular momentum of a photon is one unit, and thus the transitions where $\Delta J = 0$ are forbidden. Possible values of the released gamma lie

---

[2] Although often referred to as spin, whose actual symbol is S, the symbol J represents the total angular momentum ($J = L + S$) where L denotes orbital angular momentum.

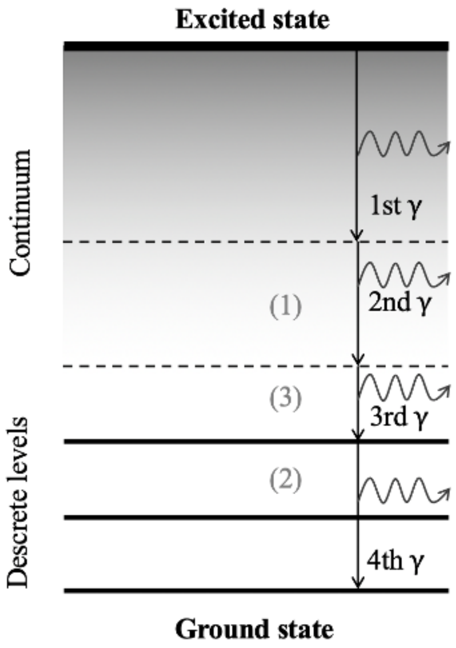

Figure 2.8: De-excitation of an arbitrary nucleus from neutron-capture state towards ground state via multiple gamma transitions. Reproduced and modified from [10].

in the range

$$|J_f - J_i| \leq \Delta J \leq (J_f + J_i) \tag{2.10}$$

An alternative (and increasingly probable) de-excitation mode known as internal conversion presents itself as the nucleus approaches states of lower energies. [11]

Internal Conversion

Internal conversion (IC) results in the direct emission of an orbital electron. IC and gamma-ray decay are competing processes. The ratio of IC decay rate λ_{ICE} to gamma decay rate λ_γ can be described by the internal conversion coefficient (ICC) α:

$$\alpha = \frac{\lambda_{ICE}}{\lambda_\gamma} \tag{2.11}$$

The coefficient becomes small in cases where gamma decay is preferred and large when IC is preferred. IC's probability depends on the electron shell (K, L, M, ...), and each shell, therefore, has respective coefficients (α_K,α_L,α_M, ...). Transition levels of lower energy favor internal conversion. Inner shell electrons, such as those from the K-shell, are more likely to interact directly with the nucleus since their wave function has a finite probability of penetrating the nucleus. The probability of IC in a shell becomes less likely the further away it lies from the nucleus. In other words, internal conversion heavily relies on the atomic electron density inside the nucleus. Consequently, nuclear interactions with the K-shell are more likely than with the L-shell, than the M-shell, and so on. The total ICC is the ratio of the total number of ICEs to gamma-rays emitted by a nucleus, and is a sum of shell coefficients:

$$\alpha = \sum_i \alpha_i \ , \ i = K, L, M, ... \tag{2.12}$$

Available transition energy (E_T) and the binding energy ($E_{bi,i}$) of a shell determines the ICE's energy

$$E_{ICE} = E_T - E_{bi,i} \tag{2.13}$$

The emitted ICE leaves behind a vacancy that is filled by atomic electrons, and leads to x-ray and Auger electron emission. [11]

X-rays and Auger Electrons

An atom releases x-rays when higher lying electrons descend and fill a lower lying electron vacancy. An electron descend from subshell p and filling a vacancy in a lower subshell $m(<p)$ releases an x-ray with an energy equal to the difference in binding energy of the electron subshells p and m

$$E_{x-ray} = E_T = E_{bi,p} - E_{bi,m} \tag{2.14}$$

On the other hand, the electron's transition energy may go into freeing an electron of an intermediate subshell n, where n lies between shell m and p. This is called an Auger electron and has energy equal to the difference in the transition energy and its initial binding energy.

$$E_{Ae^-} = E_T - E_{bi,n} \tag{2.15}$$

2.2.4 Neutron Absorption Probability

A beam of N_0 neutrons traversing an target material will be stripped of neutrons due to neutron interactions. The number of neutrons N passing through an absorbing material is given by Lambert-Beers law, which states that

$$N = N_0 e^{-\mu x} \tag{2.16}$$

The absorption coefficient μ is characteristic of the material and neutron energy, and is inversely proportional to a neutron's mean-free-path X_m. The chance of a neutron escaping the absorber is the ratio of escaped neutrons to incident neutrons (N/N_0) and the absorption probability p can be expressed as

$$p = 1 - \frac{N}{N_0} = 1 - e^{-\frac{x}{X_m}} \tag{2.17}$$

Figure 2.9 illustrates the absorption probability as a function of absorber thickness. The probability of being absorbed increases when the absorber thickness is large relative to the X_m, 60% neutrons are absorbed after only one mean-free-path and after two, more than 80% are absorbed. [7]

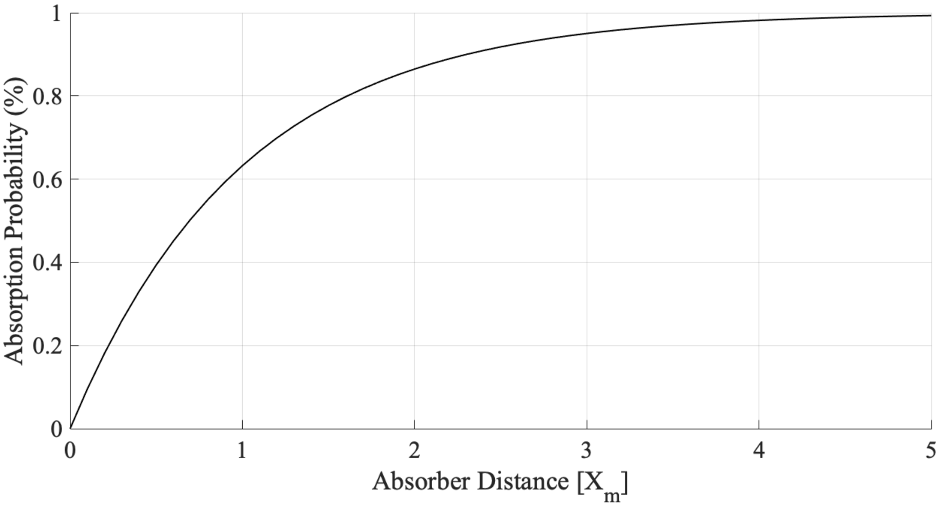

Figure 2.9: Neutron absorption probability as a function of distance, in units X_m. Nearly all neutrons are absorbed after 5 X_m. (Equation 2.17 plotted with MATLAB)

2.3 Electron Interactions With Matter

The total energy loss of an electron interacting with matter can be expressed as the sum of two energy loss terms:

$$\left(\frac{dE}{dx}\right)_{tot} = \left(\frac{dE}{dx}\right)_{col} + \left(\frac{dE}{dx}\right)_{rad} \tag{2.18}$$

where $(dE/dx)_{col}$ is collisional loss and $(dE/dx)_{rad}$ is radiation loss. The approximate ratio of the two loss terms is

$$\frac{(dE/dx)_{rad}}{(dE/dx)_{col}} \approx \frac{EZ}{700} \tag{2.19}$$

which states that radiative loss is only serious in heavy material with a large atomic number Z and/or for high electron energies E in units of MeV. [12]

Figure 2.10 illustrates the total energy loss as a function of electron energy and shows that collision loss varies logarithmically and radiation loss linearly with energy. Electrons with relatively low energies mainly lose energy through collisions and as energy steadily increases, radiational loss becomes more significant. [6]

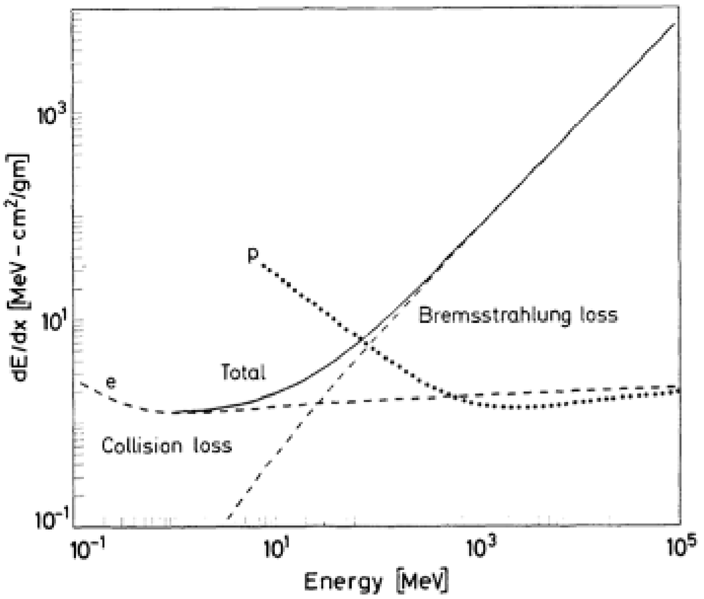

Figure 2.10: Total energy loss of an electron in Copper. A proton's total energy loss is plottet for comparison. [6]

2.3.1 Collision Loss and Bethe-Bloch Formula

Electrons lose energy through inelastic collisions with atomic electrons. The collisional loss can be modeled by the Bethe-Bloch formula, which gives the average energy loss per unit length of charged particles. The formula assumes heavy incident particles (e.g., protons and ions) but, with some modifications, is also applicable to electrons. The modifications must consider the small electron mass, scattering effects, and collisions between identical particles. The Bethe-Bloch formula corrected for electrons is:

$$-\frac{dE}{dx} = K\rho\frac{Z}{A}\frac{1}{\beta^2}\left[\ln\frac{\tau^2(\tau+2)}{2(I/m_ec^2)^2} + F(\tau) - \delta - 2\frac{C}{Z}\right] \tag{2.20}$$

where the colliding electron's kinetic energy is represented by τ, in units of m_ec^2;

$$F(\tau) = 1 - \beta^2 + \frac{\frac{\tau^2}{8} - (2r+1)\ln 2}{(\tau+1)^2} \tag{2.21}$$

$$K = 2\pi N_a {r_e}^2 m_e c^2 = 0.1535\, MeV cm^2/g$$

r_e: classical electron radius $= 2.817 \times 10^{-}13\, cm^2/g$
m_e: electron mass
N_a: Avogadro's number $= 6.022 \times 10^{23}\, mol^{-1}$
I: mean excitation potential
A: atomic weight of absorbing material
$\beta =$ p/c of the incident particle
δ: density correction
C: shell correction
ρ: density of absorbing material
Z: atomic number of absorbing material

Two factors that effect energy loss are the electron speed v and the atomic number Z of the reacting material. High-Z material are more effective than low-Z material in slowing down electrons. In equation (2.20) the relationship between energy loss and incident kinetic energy becomes apparent; the average energy loss is inversely proportional to speed (i.e., $dE/dx \propto 1/v$) and slower electrons lose more energy.

Applying conservation of energy and momentum, the maximum allowed energy transfer in a single collision W_{max} can be derived with basic kinematics and is

$$W_{max} = T_e/2 \tag{2.22}$$

where T_e is the incident electron kinetic energy. An electron can lose up to half of its energy in a single collision.

2.3.2 Radiation Loss

In addition to collisions, electrons experience energy loss through radiative processes. From electromagnetic theory, any accelerating charged particle must radiate energy. An electron attracted by the electric field of a nucleus accelerates and radiates electromagnetic waves known as bremsstrahlung. Radiative losses can occur anywhere along the electron track [12]. Bremsstrahlung emission depends on the strength of the nuclear electric field. Because of this, the electrons surrounding a nucleus play an important role "screening" the interacting electron from the full electric field strength. The quantity ξ represents the screening effect

$$\xi = \frac{100 m_e c^2 hv}{E_0 E Z^{1/3}} \tag{2.23}$$

where E_0 is the initial total electron energy; E is the final total electron energy; and hv the emitted photon energy $(E - E_0)$, all in units of MeV.

The linear radiative energy loss is

$$-\left(\frac{dE}{dx}\right)_{rad} = NE_0\Phi_{rad} \tag{2.24}$$

where N is the atomic density (atoms per cm^3) and Φ_{rad} is

for $1 \ll hv \ll \frac{1}{\alpha Z^{1/3}}$ and no screening ($\xi \gg 1$):

$$\Phi_{rad} = 4Z^2r_e^2\alpha\left(ln\frac{2E_0}{m_ec^2} - \frac{1}{3} - f(Z)\right)$$

for $hv \gg \frac{1}{\alpha Z^{1/3}}$ and complete screening ($\xi \approx 0$):

$$\Phi_{rad} = 4Z^2r_e^2\alpha\left(ln(183Z^{-1/3}) + \frac{1}{18} - f(Z)\right)$$

where α is 1/137, the fine structure constant; and $f(Z)$ Coulomb corrections

$$f(Z) \approx a^2[(1+a^2)^{-1} + 0.20206 - 0.0369a^2 + 0.0083a^4 - 0.002a^6] \tag{2.25}$$

and $a = Z/137$. [6]

2.3.3 Backscattering of Low-Energy Electrons

Electrons not only experience inelastic collisions but also elastic collisions from nuclei. Since electron mass is comparably negligible to a nucleus, it is assumed that no energy transfer takes place and that the electron energy stays intact. An electron colliding elastically with a nucleus typically experiences a small angular deflection. Experiencing multiple scattering events, an electron traveling in a material builds up a net deflection from its initial trajectory as it zigzags its way through, as illustrated by Figure 2.11.

Multiple Coulomb scattering involve an average number of scattering events greater than 20 events. In such cases, one can apply statistical methods to the problem and acquire a probability distribution for the net angle of deflection as a function of the thickness of material traversed. Most of these methods model small-angle scattering (angles of $\approx 30°$) and are inapplicable for slow electrons, where $\beta < 0.05$, and large-Z materials.

Electrons are especially exposed to large-angle deflections because of their small mass, so much so that the accumulated effect can be a 180° net deflection as the electron comes out of the material in the opposite direction that it entered. This is referred to as backscattering and is illustrated in Figure 2.12. The effect is largely present for low energy electrons and increases in higher Z materials.

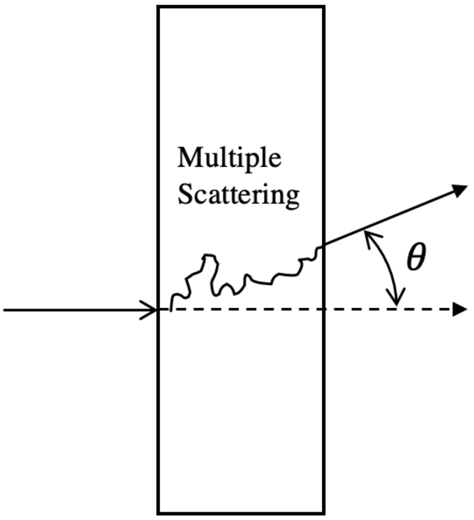

Figure 2.11: Multiple scattering resulting in a deflection θ. Inspired from [6].

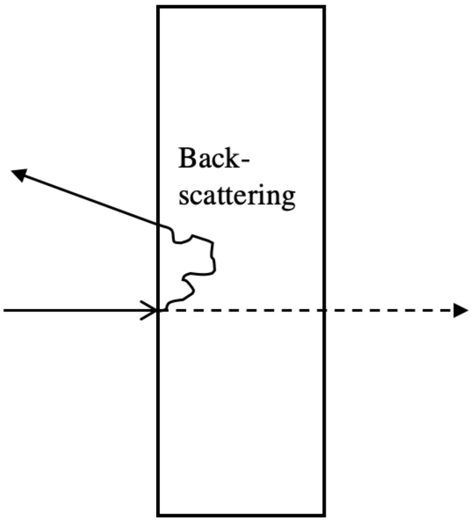

Figure 2.12: Backscattering due to multiple large-angle scattering. Inspired from [6].

The fraction of backscattered electrons to incident electrons is described by the backscattering coefficient η and may be expressed as

$$\eta = \frac{a_1}{a_2 + a_2\tau^{a_3}} \tag{2.26}$$

where T is energy; a_1,a_2,a_3 are functions of Z, the atomic number of the material; and b_i $(i = 1, 2, \ldots, 8)$ are constants independent of Z.

$$\begin{aligned}
\tau &= T/m_ec^2 \\
a_1 &= b_1exp(-b_2Z^{-b_3}) \\
a_2 &= b_4 + b_5Z^{-b_6} \\
a_3 &= b_7 - b_8/Z
\end{aligned}$$

Figure 2.13 illustrates the backscattering coefficient, as a function of energy, which takes on an S-shaped curve. The probability of backscattering increases in heavier materials and is dependent on the incident angle, where particles traveling parallel to the surface normal are less probable of turning around than those traveling at an angle to the normal. [13]

Backscattering poses a problem in detectors which rely on electron-induced signals. Depending on detector material and geometry, a large fraction of incident electrons will be lost owing to the effect and will consequently drastically reduce the efficiency of the device. [6]

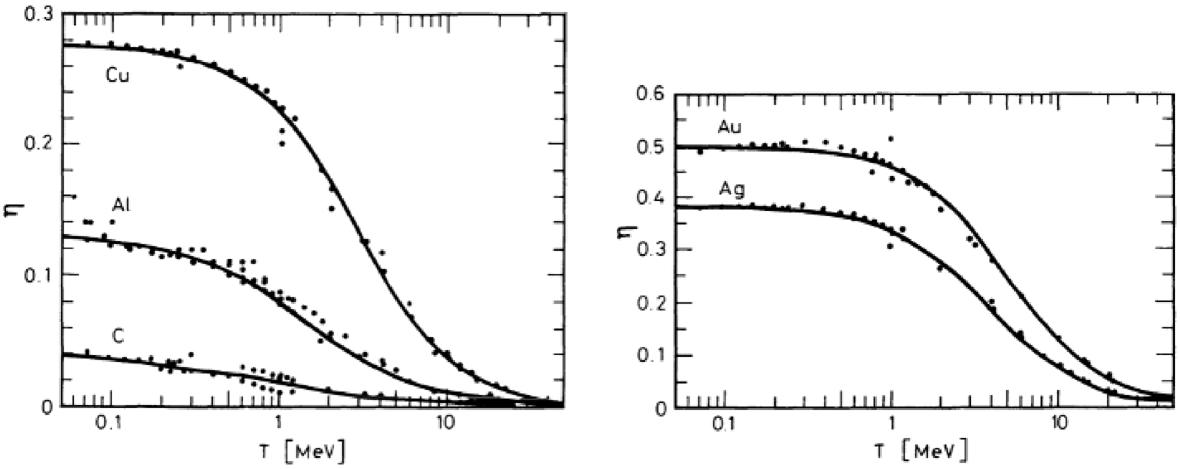

Figure 2.13: Backscattering coefficient η vs. electron energy in various Z material. From [13].

2.3.4 Energy Straggling

Charged particles in matter will lose energy mainly from inelastic collisions with atomic electrons. The mean linear energy loss (dE/dx) can be calculated with the Bethe-Bloch formula (equation 2.20). It gives a good approximation to the average energy loss (dE/dx) of a mono-energetic particle beam. However, it does not provide information on the various amounts of energy lost by the beam's individual particles. Because particle scattering is a statistical phenomenon - following a probability distribution - the number of collisions made by same-energy particles differs, and the same goes for the amount of energy lost. The small variation in energy loss is known as energy straggling. [6]

A mono-energetic beam striking an absorber exits with a shifted and a spread-out energy distribution. If each particle lost exactly dE/dx (average beam loss), the final beam energy would merely be shifted dE/dx lower than the initial. In actuality, the exiting beam shows a spread out and shifted version of the discrete incident beam-energy. The spreading out of energies is strictly related to the varying energy loss of the individual beam particles. For heavy-charged particles (heavier than one atomic unit) penetrating relatively thick (compared to the particles' projected range) absorbers, the energy loss takes on a Gaussian shape. A Gaussian fit is applicable when the number of collisions is large (which is when absorber thickness is large compared to particle range). This approximation stems from the Central Limit Theorem in statistics, which states that the sum of N random variables (e.g., particle collisions), subject to the same statistical probability, converges towards that of a Gaussian-distributed variable as N approaches infinite (a vast number of collisions). [6]

As the absorber slims down and the number of charged particle collisions decreases, a Landau distribution becomes a more appropriate fit. In a slim absorber, traversing

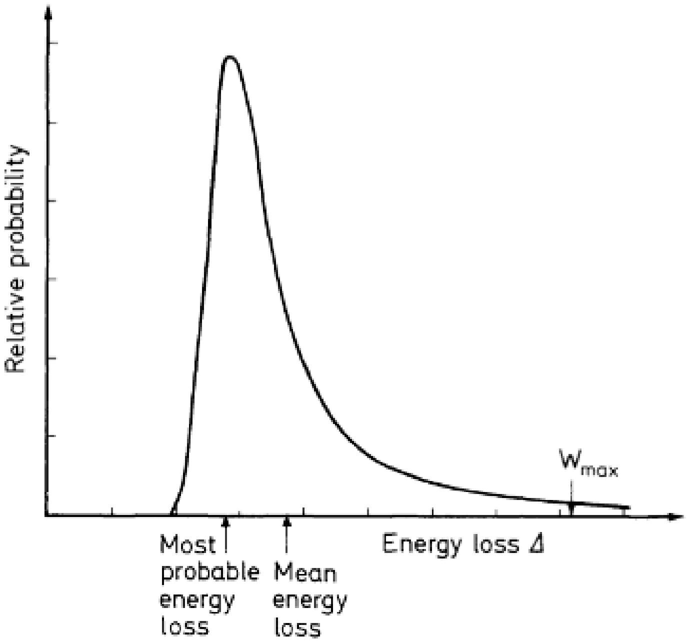

Figure 2.14: Landau distribution: the typical energy loss distribution of electrons passing through a thickness of matter. From [6].

particles scatter less, and the majority lose smaller energy portions than for the thick absorber case. The probability of losing a large amount of energy is less in a single-collision, but still noticeable, and results in a right-skewed distribution. These large-energy loss cases cause an asymmetrical distribution where the most probable loss lies at low energies in front of a tail of less probable higher-energy losses. The Landau-shaped distribution appears as a right-skewed distribution with a tail on the right of the peak. The energy distribution shape also depends on particle energy. Particles with high energies typically have a large range, and so a fixed-thickness absorber becomes thinner with higher particle energy. Traversing the same absorber, the energy loss of fast particles shows a Landau distribution, while slower particles lean towards a Gaussian distribution. With higher particle speed, the probability of low energy transfer events increase; the Landau distribution, illustrated in Figure 2.14, shifts further to the right and grows a longer tail. [6]

The energy-loss of electrons is similar to that of heavy charged particles passing a thin absorber. Because of their small mass, electrons suffer from multiple scattering in thin absorbers. Electrons are also capable of significant energy loss in single collisions. The rare high loss events add a long tail to the distribution. The Landau model works well for most materials and electron energies [14]. [6]

2.4 Photon Interactions With Matter

Photons interact differently with matter than charged particles do. The most relevant photon interactions with matter are Compton scattering, photoelectric absorption, and pair production. Cross-section σ describes the probability of a photon interacting with matter and is the cross-sectional sum of photon interactions:

$$\sigma = \sigma_{photo} + \sigma_{compt} + \sigma_{pair} \tag{2.27}$$

Figure 2.15 illustrates the photon cross-sections as functions of photon energy.

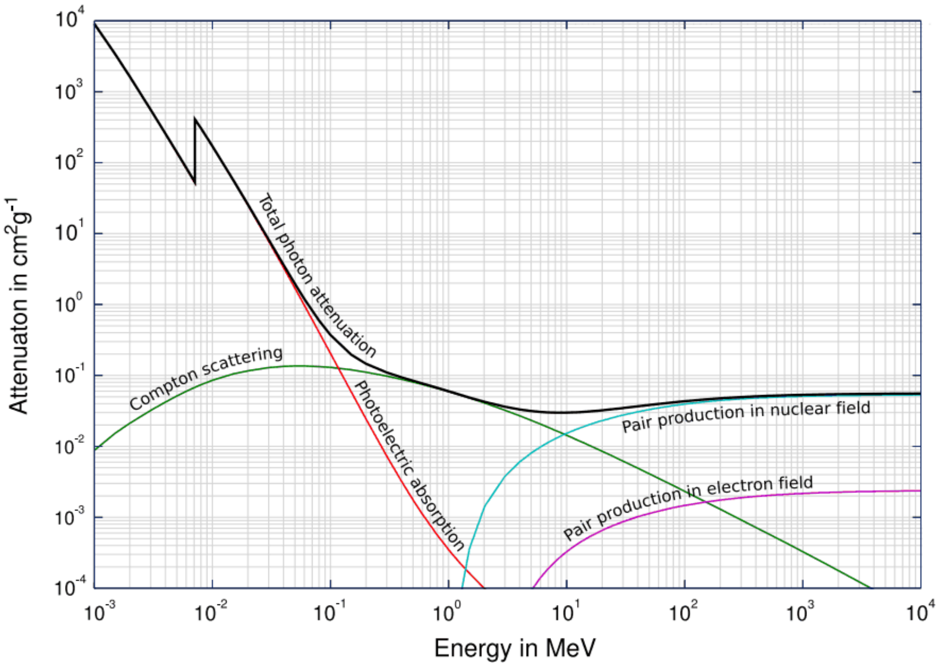

Figure 2.15: The total, photoelectric absorption, Compton, and pair-production cross-section of iron as a function of photon energy. [15]

2.4.1 Photoelectric Absorption

Photoelectric absorption describes an event where an atom completely absorbs a photon. The atom is more energetic after it has absorbed the photon energy and kicks out an atomic electron (a photoelectron). Atoms absorbing photons of ample energy are more likely to emit strongly bound inner-shell electrons (e.g., K-shell electrons). The photoelectron has a kinetic energy equal to the difference between the photon's energy (hv)

and the binding energy (E_b) of the shell it vacates:

$$E_{e^-} = hv - E_b \tag{2.28}$$

In the wake of the emitted photoelectron is an electron vacancy. This vacancy is immediately replaced by a higher shell electron or filled by a free electron of the material. An electron transitioning to a lower shell results in characteristic x-ray emission where the transmitted x-ray energy is

$$E_{x-ray} = E_{b_2} - E_{b_1} \tag{2.29}$$

the difference in binding energy of the final (b_2) and initial (b_1) electron shell. There is no general expression for the cross-section which covers all materials and energies, but a rough approximation is

$$\sigma_{photo} \propto \frac{Z^n}{E_\gamma^{3.5}} \tag{2.30}$$

where n = 4 for relatively low photon energies and n = 5 in the relativistic region. Photoelectric absorption is the primary interaction process of relatively low-energy photons and intensifies in heavier materials. Figure 2.16 shows the photoelectric absorption cross-section decreasing with higher energies. [16]

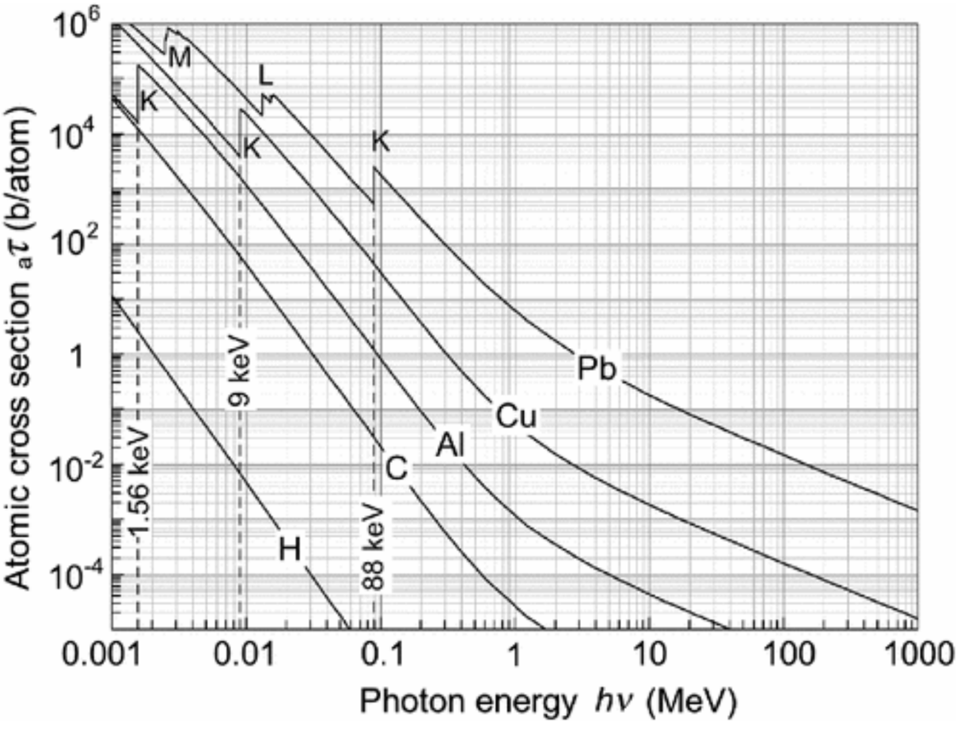

Figure 2.16: Photoelectric absorption cross-section as a function of energy for various material. From [16]

2.4.2 Compton Scattering

Figure 2.17 (left) illustrates a Compton scattering event between an incoming photon and a free electron. Electrons found in matter are atomically bound. The electron's binding energy becomes negligible if the photon energy is large and it can be considered as an essentially free electron. Compton scattering conserves energy and momentum. The electron gains the energy lost by the photon.

After collision the new photon energy is

$$hv' = \frac{hv}{1 + \gamma(1 - \cos\theta)} \tag{2.31}$$

where $\gamma = \frac{hv}{m_e c^2}$, hv is the initial photon energy and θ is the photon scatter angle after collision. The transfer energy is

$$T = hv - hv' = hv\frac{\gamma(1 - \cos\theta)}{1 + \gamma(1 - \cos\theta)} \tag{2.32}$$

With the above expressions one sees the dependence of final photon energy on the photon scattering angle. Photons whose trajectories are drastically altered (i.e. large θ) show greater energy loss. That is, with greater photon scattering angle more energy is transferred to the electron. All scattering angles are possible and the electron energy gain ranges from zero to a large portion of the photon energy. A head-on collision where incident angle is 0° and the scattering angle is 180° yields the largest possible energy transfer

$$T_{max} = hv\frac{2\gamma}{1 + 2\gamma} \tag{2.33}$$

Figure 2.17 (right) depicts the energy distribution of recoil electrons. The sharp drop after maximum recoil energy is known as the *Compton edge.*

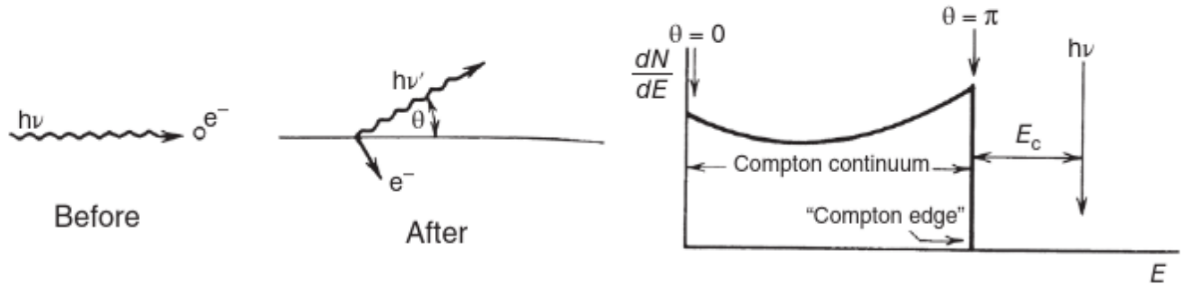

Figure 2.17: Left: The geometry of Compton scattering. Right: Compton recoil electrons' energy distribution. At maximum recoil energy, the sharp drop is known as the Compton edge. From [11].

The differential electronic cross-section per unit solid angle $d_e\sigma_C^{KN}/d\Omega$ (i.e., the cross-section as a function of particle angle) is stated by the Klein-Nishina formula. The total cross-section per electron can be derived by integrating over all scattering angles

$$_e\sigma_C^{KN} = 2\pi r_e^2 \left\{ \frac{1+\gamma}{\gamma^2}\left[\frac{2(1+\gamma)}{1+2\gamma} - \frac{1}{\gamma} ln(1+2\gamma)\right] - \frac{1}{2\gamma} ln(1+2\gamma) - \frac{1+3\gamma}{(1+2\gamma)^2}\right\} \{cm^2/electron\} \tag{2.34}$$

The probability of Compton scattering increases with the number of available electrons in a material and the atomic Compton cross-section is

$$_a\sigma_C^{KN} = Z(_e\sigma_C^{KN}) \tag{2.35}$$

Multiplying the differential electronic cross section $d_e\sigma_C^{KN}/d\Omega$ by the fractional energy of the Compton recoil electron $(E_K^C/h\upsilon)$ and integrating over all scattering angles θ yields the electronic energy transfer cross-section

$$\begin{aligned}(_\mathrm{e}\sigma_\mathrm{C}^\mathrm{KN})_\mathrm{tr} = 2\pi r_\mathrm{e}^2 & \frac{2(1+\varepsilon)^2}{\gamma^2(1+2\gamma)} - \frac{1+3\gamma}{(1+2\gamma)^2} - \frac{(1+\gamma)(2\gamma^2-2\gamma-1)}{\gamma^2(1+2\gamma)^2} \\ & - \frac{4\gamma^2}{3(1+2\gamma)^3} - \left[\frac{1+\gamma}{\gamma^3} - \frac{1}{2\gamma} + \frac{1}{2\gamma^3}\right] \ln(1+2\gamma).\end{aligned}$$

Figure 2.18 illustrates how the probability of Compton scatter $(_e\sigma_C^{KN})$ lessons with higher photon energy and that energy transfer to the Compton electron starts out low for low photon energies, reaches peak value, and decreases with decreasing electronic cross-section as photon energy increases. [16]

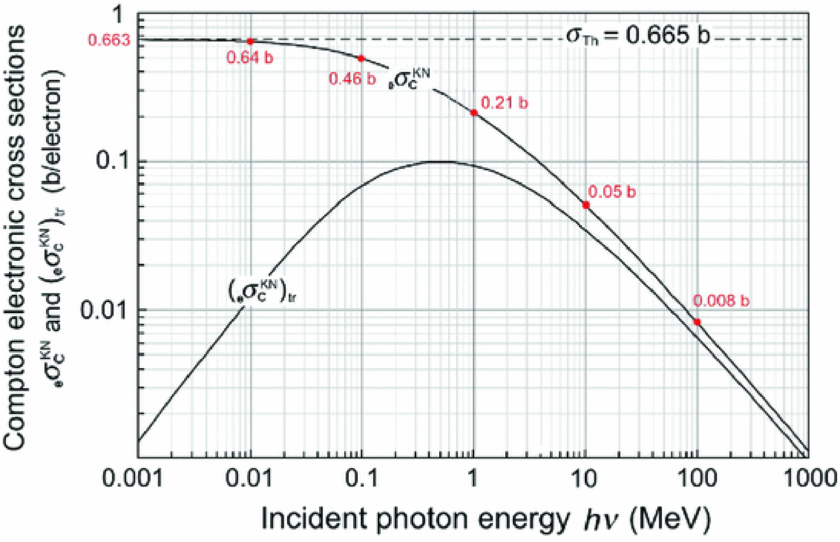

Figure 2.18: Determined from Klein–Nishina equation, Compton electronic cross-section $(_e\sigma_C^{KN})$ *for a free electron as a function of incident photon energy. Also displayed is Compton electronic energy transfer cross-section* $(_e\sigma_C^{KN})_{tr}$*. [16]*

2.4.3 Pair Production

When the incident photon energy hv surpasses twice the rest-mass energy of an electron ($2m_ec^2$ =1.02 MeV), the production of an electron-positron pair becomes energetically possible. During pair production, the photon interacts with the Coulomb field of a nucleus and is completely absorbed. The effect requires the conservation of energy, charge, and momentum. The photon's momentum is distributed to the particle pair and to the nucleus near which the interaction occurs. Ignoring the exceedingly small energy transfer to the absorber nucleus, the energy distributed to the produced electron and positron is expressed as

$$E_{PP} = hv - 2m_ec^2 \tag{2.36}$$

All distributions of the available energy are equally probable, except the case where one of the particles runs away with all of the energy, and the other left with none. The average energy transfer to each particle is half the available energy: $E_{PP}/2$.

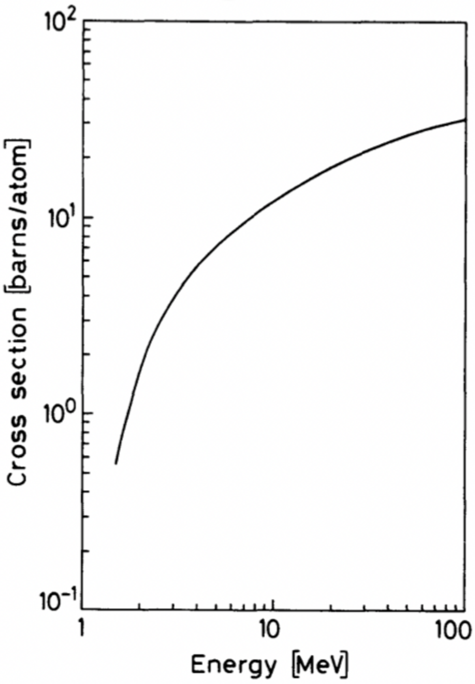

Figure 2.19: Cross-section of pair production in lead. From [12].

The cross-section of pair production differs depending on incident photon energy and whether nuclear screening is accounted for. As a function of γ and Z, the cross-section is

$$\sigma_{pair} = \alpha r_e^2 Z^2 P(\gamma, Z) \tag{2.37}$$

The fine structure constant α is $1/137$ and P is a complicated function of photon energy

$\gamma = hv/(m_e c^2)$ and atomic number Z:

$$1 << \gamma << \frac{1}{\alpha Z^{1/3}} \text{ and no screening:} \quad P(\gamma, Z) = \frac{28}{9} ln(\gamma) - \frac{218}{27} \qquad \{cm^2/atom\} \tag{2.38}$$

$$\gamma >> \frac{1}{\alpha Z^{1/3}} \text{ and complete screening:} \quad P(\gamma, Z) = \frac{28}{9} ln\left(\frac{183}{Z^{1/3}}\right) - \frac{2}{27} \{cm^2/atom\} \tag{2.39}$$

Nuclear screening becomes effective for very high photon energies (hv >20 MeV). Leaving screening effects aside, it becomes apparent from equation (2.37) and (2.38) that the cross-section is proportional to Z^2. Figure 2.19 illustrating its cross-section, pair production is the predominant mode of interaction for photons of relatively high energies.

Figure 2.20 shows the three photon cross-section's dependence on photon energy hv and atomic number Z of the absorbing material. Marked in the plot, three areas indicate the range in which photoelectric effect, Compton scattering, and pair production dominates. The lines separating the areas indicate Z and hv values for which the two neighboring effects are equal.

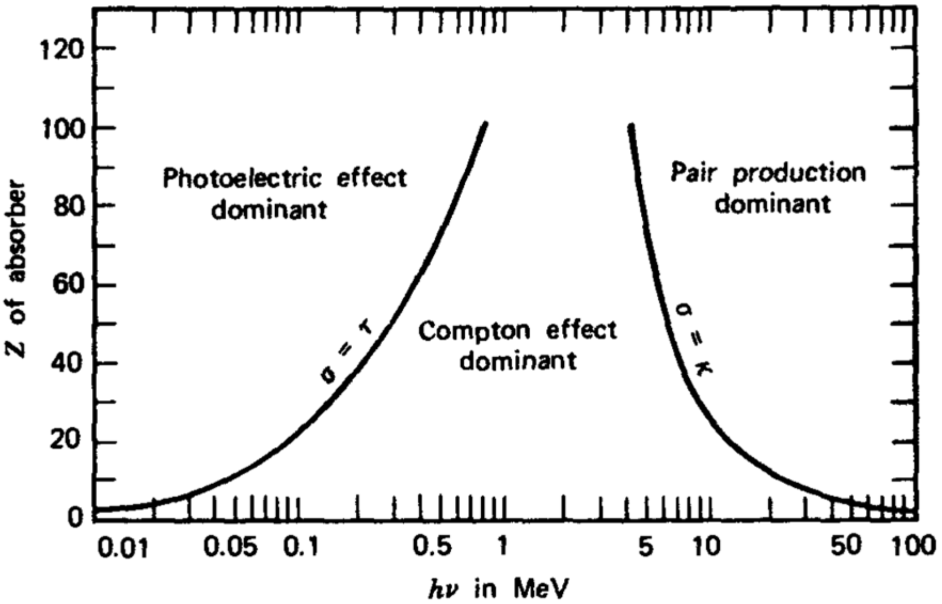

Figure 2.20: Dominant processes of photon interaction as a function of energy and atomic number. From [12].

2.5 Semiconductor Detectors

Semiconductor detectors use solid semiconducting material to detect ionizing radiation (like electrons and photons). Semiconducting material's electrical conductivity lies between that of conductors (such as metals) and insulators (such as plastics), hence the name "semi"-conductor. At absolute zero (0 K), semiconductors resemble insulators, prohibiting electrical currents, and with increasing temperatures, resemble conductors, which promote electrical currents. A semiconductor gains conductive properties when the material's energy increases (e.g., by increasing temperature or ionization), and atomic electrons are excited so that they flow freely between atoms and form an electric current.

An energy band diagram represents the energy levels of an atomic structure and helps illustrate its conductive properties. Its vertical axis corresponds to an atomic electron's total energy and horizontal axis to the electron's positions in the atomic structure. Electrons bound to the atom are found in the valence band, and free electrons are found in the conduction band. A semiconductor's valence band and conduction band are separated by a band-gap, which indicates forbidden electron energies. For a semiconductor's valence electron to exist in the conduction band, it must gain energy equal to or greater than the energy corresponding to the band-gap's width ΔE. Usually, the band-gap of semiconductors are less than 5 eV, typically 1 eV. [12]

One way valence electrons can gain energy is through excitation by ionizing radiation. Ionizing radiation entering a semiconducting material interacts with the material's atoms and excites valence electrons such that they jump to the conduction band and are free to roam the material. The excitation of electrons results in electron holes in the atom, a process known as electron-hole pair production. Without an electrical field to separate the them, the generated charges are prone to recombine. An electric field can be created, and charge collection becomes possible by introducing different impurity atoms to the semiconductor material, a process known as doping.

A p-n junction is the interface between two types of semiconductor materials, p-type and n-type, depicted in Figure 2.21. A P-type semiconductor is doped with electron acceptor atoms and has an excess of mobile holes, and an n-type semiconductor is doped with electron donor atoms and has an excess of mobile electrons. When the two types are fused together, holes of the p-type attract the mobile electrons of the n-type. The electrons diffuse and combine with the holes, canceling out each other's charge. Similarly, the p-type's mobile holes diffuse towards the n-side and combine with its electrons. In the process of charge diffusion, atoms near the junction are depleted of mobile charge carriers and lose their neutrality; part of the n-side becomes positive, and part of the p-

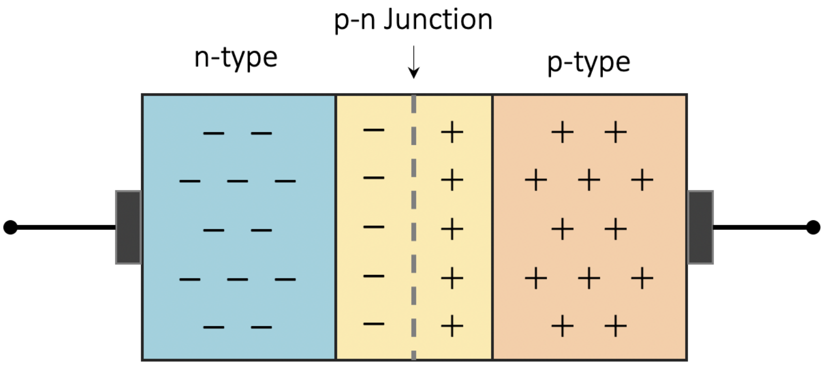

Figure 2.21: A p-n junction with open-circuited terminals (no external voltage). Modified from [17].

side becomes negative, creating a space charge region or depletion region. Consequently, an electric field arises across the depletion region that opposes the process of charge diffusion. The electric field increases as charge accumulate on respective sides. When the field reaches a magnitude that the mobile charge carriers can no longer overcome, diffusion stops, and an equilibrium state is reached. To cross the depletion region, a mobile charge carrier of either side now requires extra energy to overcome the potential barrier created by the depletion region's electric field. Promoting current in one direction but not the other, the p-n junction functions as a diode.

In a circuit, a p-n junction can be used to detect ionizing radiation. Ionizing radiation traversing the depletion region generates electron-hole pairs along its path. The depletion region's electric field hinders the generated charge from recombining and carries it away in opposite directions, electrons towards the n-side and holes towards the p-side. Attaching electrodes to each side of the p-n junction enables its integration into an electrical circuit, which can be used to register the generated charge.

The thickness of the depletion region represents the detector's sensitive volume. Applying reverse bias, an external voltage, to the junction can expand the depletion region's thickness. Many semiconductor detectors are operated with reverse bias, and with a sufficiently large bias, the depletion region can be expanded through the full thickness of semiconductor substrate, creating a fully depleted detector.

Electron-hole pairs are the information carriers of semiconductors and generate a signal when registered by the detector's readout electronics. The generated signal carries information on the energy transferred by the ionizing radiation, and several signals over some time provide information on the radiation's intensity.

Semiconductors' advantage lies with their comparably small ionization energy. About 3 eV is required to produce an electron-hole pair in silicon, a semiconducting material.

For comparison, the ionization energy needed to generate an ion-electron pair in a standard gaseous detector is 30 eV, ten times more. Hence, for a certain amount of energy transferred in the detector's sensitive volume, the number of information carriers is ten folds in the case of semiconductors. Producing more information carriers per unit energy, semiconductors show a higher energy sensitivity than gas detectors. Furthermore, semiconductors' small ionization energy requires less material of the sensitive volume to generate sufficient information carriers and allow for more compact detector designs.

As the number of electron-hole pairs is energy-related, a semiconductor detector can observe ionizing radiation's energy. Photons easily penetrate semiconductor materials such as silicon and rarely deposit their full energy to the material. It is, therefore, difficult to obtain information on the photons' full energy. However, with a sufficiently thick sensitive volume such that photon interaction is of a certain probability, the semiconductor becomes a radiation counter and counts the number of incident photons, and observe the photon intensity. More often used for charged particle detection, these detectors are used for measuring particle energy, given the particles are entirely stopped, and deposit all their kinetic energy in the detector's sensitive volume.

When it comes to detecting neutrons with semiconductors, the neutrons cannot directly generate a signal in the detector due to its lack of ionizing features but must do so indirectly by creating ionizing radiation that can. Neutron conversion can be achieved with a neutron converter material that absorbs (captures) neutrons and generates charged particles and photons. [12]

Probable for all energies, neutron capture has the highest probability in the thermal energy range. While the energy distribution of the neutron produced particles is measurable, the captured neutron's energy is lost in the process of conversion. The simplest form of neutron measurement involves recording a number of signals proportional to the number of captured neutrons. Neutron detectors used for such measurements are called neutron monitors. [18]

The neutron detector of this thesis is essentially a neutron monitor. It implements a gadolinium (Gd) converter foil and a silicon semiconductor, ALPIDE, to count the number of neutrons incident on the detector.

2.6 The ALPIDE Sensor

Alice Pixel Detector (ALPIDE) is a monolithic active pixel sensor (MAPS) based on TowerJazz 180 nm CMOS technology. It was designed for high energy particle physics experiments, specifically for the upgrade of the Inner Tracking System (ITS), a part of the ALICE experiment at CERN. Since 2012, several prototypes of the ALPIDE have been developed. The final, optimized chip was validated in 2016 after substantial test-beam campaigns that show performance values beyond the requirements set by the ITS upgrade listed in Table 2.1. The chip has a high detection efficiency, short dead time, and excellent spatial resolution for tracking charged particles. [4]

Table 2.1: ALPIDE performance [4].

Parameters	
Chip dimensions ($mm \times mm$)	15×30
Spatial resolution (μm)	5
Detection efficiency	$> 99\%$
Fake hit probability ($\text{evt}^{-1}\text{pixel}^{-1}$)	$<< 10^{-5}$
Power density (mW/cm^2)	~ 35
Integration time (μ s)	10
NIEL[a]radiation hardness[b](1 MeV n_{eq}/cm^2)	1.7×10^{13}

[a] NIEL: nonionizing energy loss [19].

[b] 10× the radiation exposure inside inner barrel of ITS integrated over 6 years of operation.

2.6.1 Pixel Features

A cross-sectional view of a pixel is illustrated in Figure 2.22. The sensor is realized on a silicon substrate on which a highly resistive epitaxial layer (the sensitive volume) is grown. The possible thicknesses of the sensitive volume ranges from 18 μm to 30 μm. (The chip used in this thesis had a 25 μm thick sensitive volume.) P-wells are placed into the epitaxial layer. A potential barrier forms where the heavily p-doped (P++) substrate and (P+) wells meet the lightly p-doped (P-) epitaxial layer. Electrons (e) are vertically confined by the potential barriers and diffuse laterally across pixels.

The ALPIDE chip is based on the 180 nm CMOS technology of TowerJazz. An important design feature is the deep p-well which shields n-wells of the pMOS transistor from the active layer. This prohibits diodes and n-wells from competing in collecting electrons. The feature allows the full use of CMOS circuitry in the epitaxial layer without impairing charge collection.

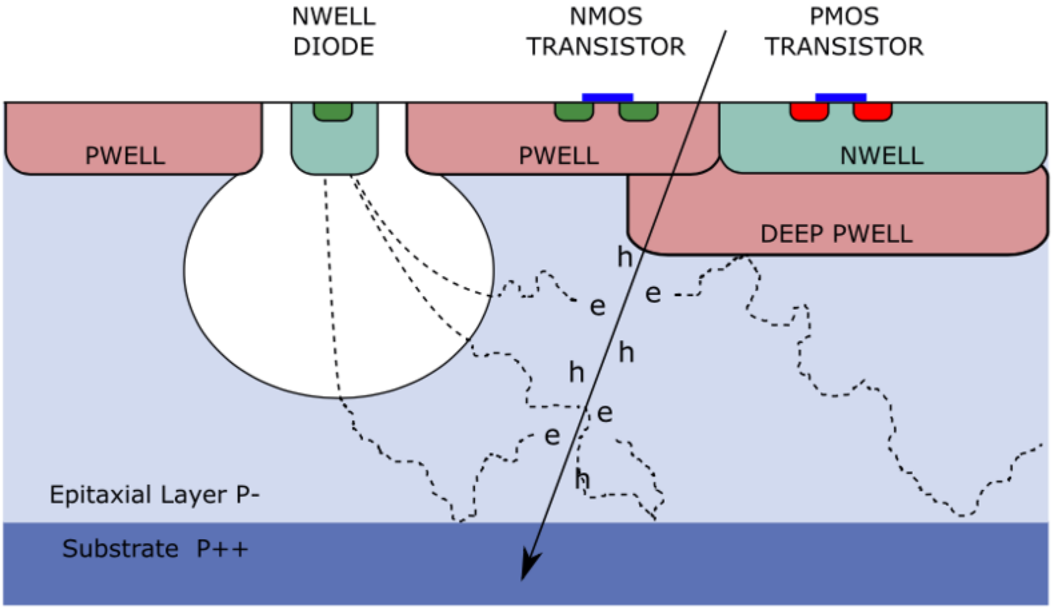

Figure 2.22: Schematic view of ALPIDE and its corresponding charge collection. [4]

The n-well diode, the sensing element of the pixel, is surrounded by a depletion volume. Moderate reverse bias can be applied to the substrate to increase the depletion volume and improve charge collection. [20]

The epitaxial layer is, for the most part, free of electric fields and the charge is left to thermally diffuse in the sensitive volume until it is collected by the diode or recombines with the atomic structure [21].

2.6.2 Chip Layout

An illustration of the chip's sensitive surface area is depicted in Figure 2.23. ALPIDE measures 15 mm by 30 mm, and contains more than five hundred thousand pixels, organized into 512 rows and 1024 columns. The pixel matrix is grouped into 32 sections with 16 columns in each (16 col/sect x 32 sect = 512 col). Each pixel has a surface area of 29.24 μm $\times$ 26.88 μm and a sensing diode (diameter $\sim 2\mu$m) approximately 100 times smaller than the pixel area. The peripheral region (1.2×30 mm^2) implements analog biasing, control, readout and interfacing functionalities [4].

Readout is controlled at the chip periphery. Sections are read out simultaneously and columns sequentially. For every double-column, there is a dedicated priority encoder. Priority encoders are responsible for generating hit pixel addresses and sending said addresses to the periphery.

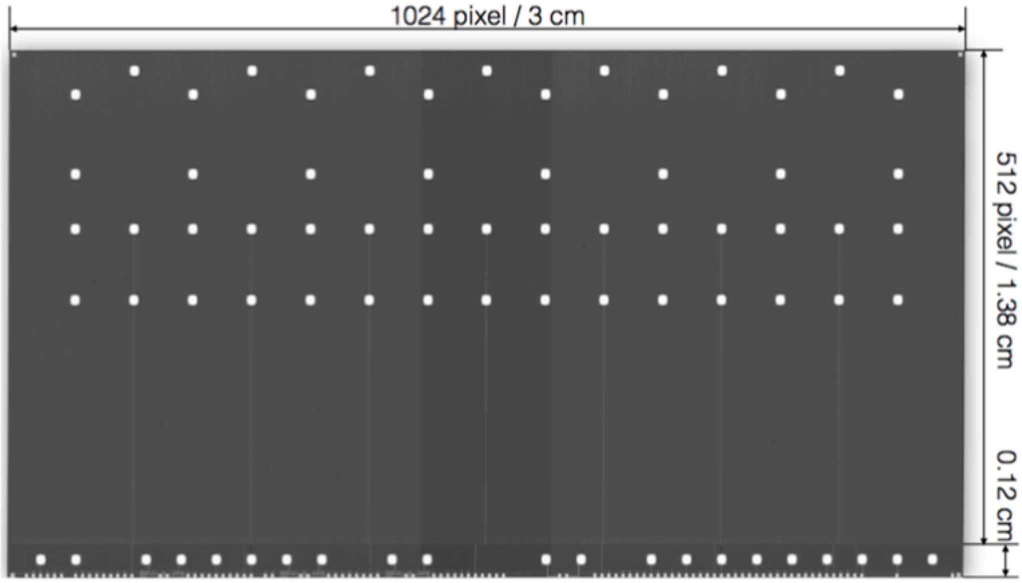

Figure 2.23: Top view of ALPIDE's pixel surface and its dimensions [22].

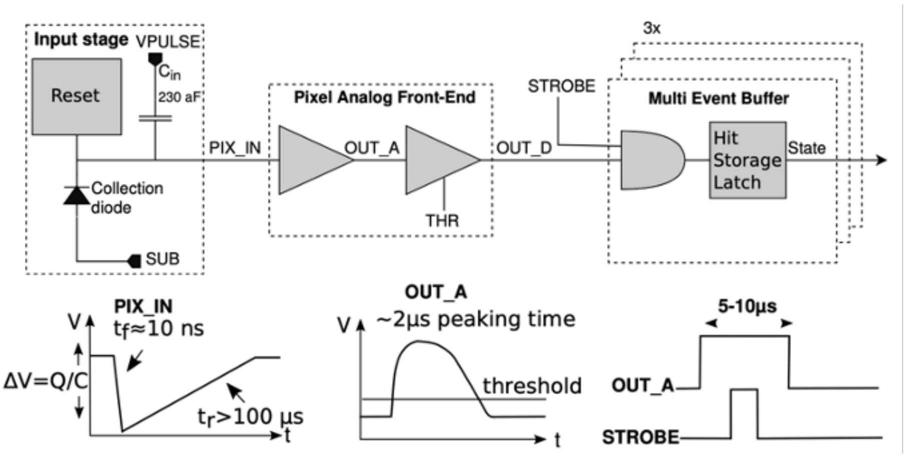

Figure 2.24: Block-diagram of an ALPIDE pixel's circuit stages [23].

2.6.3 Signal Generation and Processing

Each pixel embodies a collection diode and a front-end circuit. The in-pixel circuit, as shown in Figure 2.24, comprises an input stage, an analog front-end and a digital front-end. When hit by ionizing radiation, the sensitive volume generates electron-hole pairs. The generated electron charge accumulates around the collection diode and induces a voltage signal in the input stage. The continuous signal travels to the analog front-end where it is shaped and amplified by an amplifier. The amplifier works as a delay line, with a peaking time of 2 μs, and enables ALPIDE to be run in trigger mode [4]. A comparator is also part of the analog front-end circuit. The comparator has two analog inputs OUT_A and THR and a digital binary output OUT_D. If the amplified signal OUT_A exceeds a fixed threshold voltage THR the comparator outputs a pulse

OUT_D. The period of the output is typically 5-10 μs.

The pulse continues to the digital front-end where it encounters a STROBE signal. The STROBE signal provides a framing interval which is programmable and typically in order of a few μs. The time frame between consecutive STROBE signals is kept as short as possible, in order of ns. It is distributed globally to all pixels and can be activated either internally or externally. If the pulse from the analog front-end coincides with a window hit information is latched on to one of the three in-pixel memory cells. These memory cells are in-pixels data storage elements also known by the collective term multi-event buffer (MEB). MEB can store up to three hits simultaneously, one per buffer (memory cell). The chip's operation mode is determined by STROBE trigger settings. Continuous mode implements internal triggers while trigger mode relies on external provocation to generate a STROBE signal.[23]

A unit of ionizing radiation may activate several adjacent pixels within the same STROBE interval. These pixels define a cluster. The cluster size is the number of pixels in the cluster and depends on the amount of charge generated. Larger clusters form if more pixels are fired, and more pixels are fired with more generated charge. A heavily ionizing radiation unit which deposits large amounts of energy and consequently generates a great deal of charge, thus result in a large cluster [22]. [24]

Chapter 3

Gadolinium-Neutron Capture

Gadolinium (Gd) is well known for its high neutron-capture cross-section, and in neutron detection, for its reaction products' characteristic energy spectrum. From the perspective of thermal neutrons, natural Gd's cross-section attributes to Gd-155 and Gd-157. This chapter describes the process of thermal-neutron capture in these isotopes and features of the resultant reaction energy spectrum.

3.1 Capture Cross-Section

The cross-section of neutron capture in Gd with respect to neutron energy is illustrated in Figure 3.1. Like for most neutron-capture reactions, cross-section of Gd-neutron capture is a function of energy, following the $1/v$-law in the slow neutron region. The probability of neutron capture becomes increasingly probable for slower neutrons. Thermal neutrons display a much greater capture probability than fast neutrons.

The thermal-neutron cross-section of natural Gd is given by the weighted sum of isotopic cross-sections ($\sigma_{A,w}$), the absolute cross section (σ_A) weighted by the atomic fraction of ${}^{A}_{64}$Gd in natural Gd,

$$\sigma = \sum_A \sigma_{A,w} = 48800 \pm 150\, b \tag{3.1}$$

The atomic fraction of Gd isotopes in natural Gd and their neutron-capture cross-section are listed in Table 3.1. Among any stable isotope, the largest observed thermal-neutron cross-section belongs to Gd-157. Isotope Gd-157 and Gd-155 collectively contribute 99.99% to the total cross-section. Simplified, natural Gd interaction with thermal neutrons is a "two-absorbing isotope system" consisting of Gd-155 and Gd-157. [2]

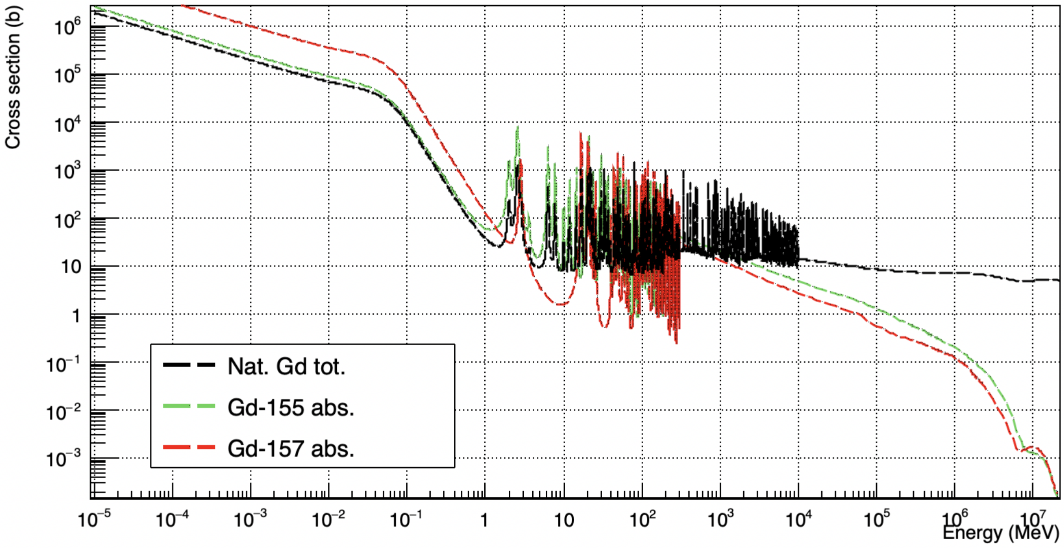

Figure 3.1: Neutron absorption cross-section of Gd-155, Gd-157 and natural Gd. Generated with nuclear data library ENDF/B-VIII.0 for Gd-155 and Gd-157, and IRDFF-II for natural Gd. [8]

Table 3.1: Cross-section and abundance of Gd-isotopes [2].

Gd-isotope	Atomic fraction (%)	Cross-section σ_A(b)	Weighted cross-section $\sigma_{A,w}$ (b)
Gd-152	0.2±0.01	735±20	1.47±0.04
Gd-154	2.18±0.03	85±12	1.85±0.26
Gd-155	14.80±0.12	60900±500	9013±74
Gd-156	20.47±0.13	2.4±0.2	0.49±0.04
Gd-157	15.65±0.02	25400±800	39751±125
Gd-158	24.84±0.07	2.2±0.2	0.55±0.05
Gd-160	21.86±0.19	1.4±0.3	0.31±0.07

3.2 Reaction Equation

Since isotopes Gd-157 and Gd-155 are responsible for most of the neutron captures in natural Gd, it is worth studying their corresponding nuclear reaction equation:

$$n +^{155}_{64} Gd \rightarrow^{156}_{64} Gd^{*} \rightarrow^{156}_{64} Gd + \gamma + ICE(Q = 8.5MeV) \tag{3.2}$$

$$n +^{157}_{64} Gd \rightarrow^{158}_{64} Gd^{*} \rightarrow^{158}_{64} Gd + \gamma + ICE(Q = 7.9MeV) \tag{3.3}$$

Once a Gd nucleus has absorbed a neutron, it exists in an excited energy state from which it decays by gamma-transition, resulting in prompt gamma (γ) and ICE emission. Byproducts of the decay are Auger electrons and x-rays prompted by vacancies left

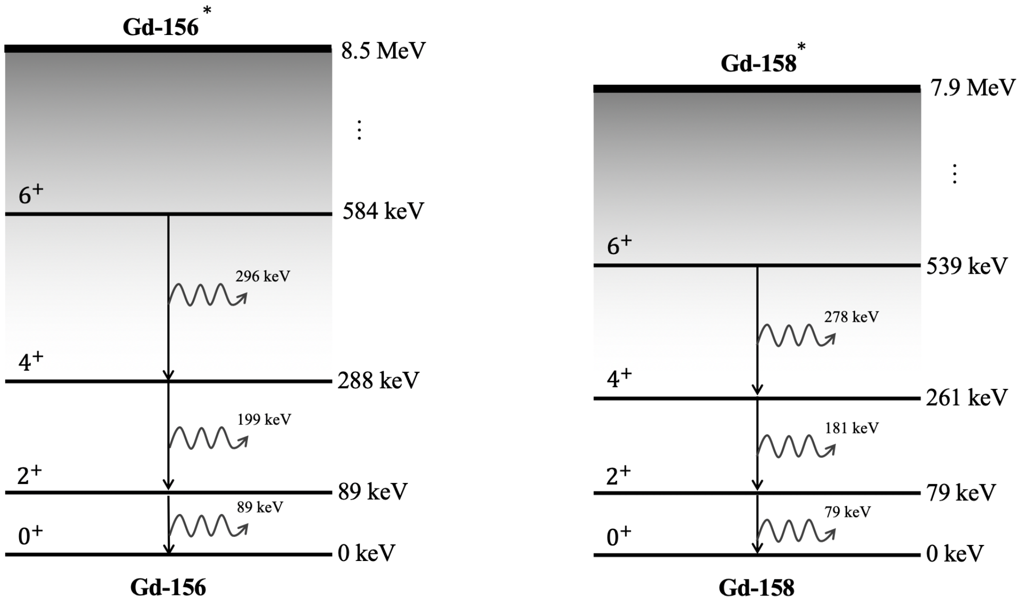

Figure 3.2: Nuclear energy level diagram of Gd-156 and Gd-158, and corresponding gamma-transition energies. Reproduced and modified from [26].

behind by ICEs. The Q-value (Q) represents the net energy released from the nuclear reaction. This energy is distributed as kinetic energy among product particles. Due to the Gd nuclei's large mass, compared to a photon (massless) and an electron, the nucleus recoil energy is neglectable [11, p. 219]. Meaning, gamma-rays and ICEs share most of the energy.

3.3 Reaction Energy Spectrum

From $Gd(n, \gamma)$ capture, the excitation energy is distributed among reaction products; prompt-gamma rays carry roughly 99% of the energy, and the ICEs receive what remains [25]. The excitation energy of Gd-156* and Gd-158* is 8.5 MeV and 7.9 MeV, respectively. The energy distribution of the reaction products ranges up to the Q-value. Emitted prompt gammas take on energies from the whole spectrum, while ICE and byproducts feature energies in the lower end, near hundreds of keVs.

The energy distribution of prompt gammas and ICEs is closely related to the nuclear structure of Gd-156 and Gd-158. The nuclear energy-level diagrams of the Gd-isotopes in question are illustrated in Figure 3.2.

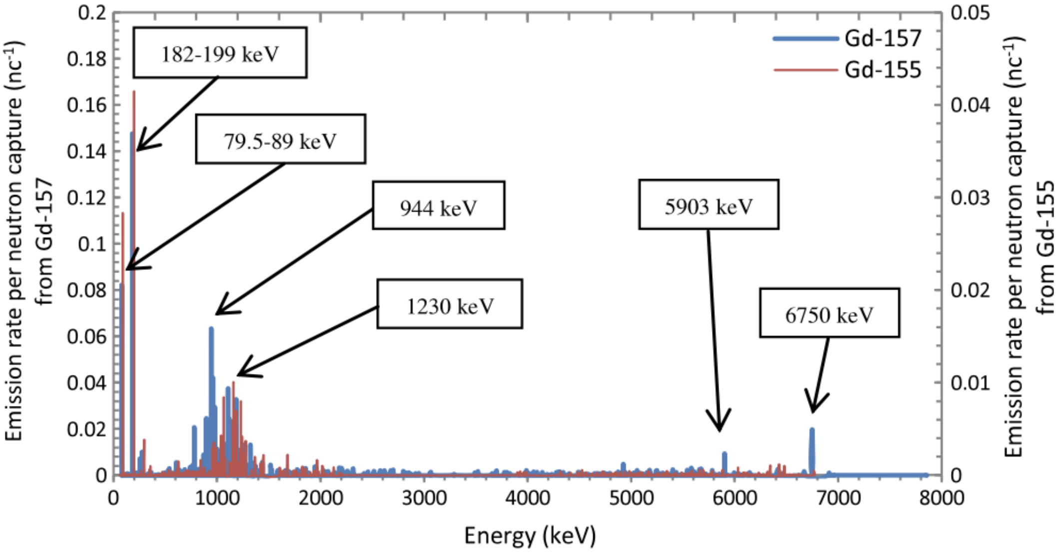

Figure 3.3: Discrete energy spectrum with emission rate per capture in the vertical axis; Gd-157 (left) and Gd-155 (right) [2].

3.3.1 Prompt-Gamma Rays

In Figure 3.3, a representation of the prompt-gamma energy spectrum is presented. Prompt-gamma energies span over several thousands of keV. The most common energies are part of a set, a collection of two distinct energies, which contains energy doublet γ_1 and γ_2. The least energetic of the two, γ_1, corresponds to the transitions from first to ground state ($2^+ \rightarrow 0^+$); and the more energetic, γ_2, to the transition from second to first excited state ($4^+ \rightarrow 2^+$). For Gd-156* and Gd-158* this energy doublet is {88.97 keV, 199.22 keV} and {79.51 keV, 181.94 keV}, respectively. The emission probability of γ_1 and γ_2 from Gd-156* is stated in Table 3.2 and from Gd-158* in Table 3.3. Other transition energies are also present during de-excitation. These are distributed over thousands of keVs and are less prominent than the gamma doublets. [2]

3.3.2 Internal Conversion Electrons

Alternatively, the atom can de-excite through internal conversion (IC) and emit ICEs. In Gd excited by neutron capture, ICE emission is most probable for transitions from first to ground state ($2^+ \rightarrow 0^+$) and second to first state ($4^+ \rightarrow 2^+$). These transitions are responsible for 96.7% of the energy carried by ICEs after capture in Gd-157 and similarly for Gd-156, and happen to be the same transitions from which the discrete gamma-ray doublets originate.

Transition levels of lower energy favor ICE emission over gamma-decay. Transitions of

Gd-158* from the lowest transition level (2^+) are more than 3 times more likely of ICE emission than gamma-decay. De-excitations from higher states are less prone to IC. At the third transition level (6^+), Gd-158* exhibits an ICE emission rate 10 times lower than that of gammas.[26]

Table 3.2: Calculated emission rates and nuclear data for Gd-156 [26].

Gamma energy (keV)	Gamma emission rate (nc^{-1})	Electron shell	ICC α	ICE energy (keV)	ICE emission rate in natural Gd (nc^{-1})
89	0.14	K	1.6	0.39	0.04
		L	1.9	0.81	0.05
		M	0.44	88	0.01
199	0.28				
		K	0.16	149	<0.01
		L	0.06	191	<0.01
		M	0.01	198	<0.01
296	0.03	K	0.05	246	<0.01
Total					0.11

Table 3.3: Calculated emission rates and nuclear data for Gd-158 [26].

Gamma energy (keV)	Gamma emission rate (nc^{-1})	Electron shell	ICC α	ICE energy (keV)	ICE emission rate in natural Gd (nc^{-1})
79	0.1	K	1.21	29	0.1
		L	3.3	71	0.27
		M	0.76	78	0.06
181	0.21				
		K	0.2	131	0.03
		L	0.084	173	0.01
		M	0.018	180	<0.01
278	0.05	K	0.1	228	<0.01
Total					0.48

3.3.3 X-rays and Auger Electrons

Vacancies in the atomic structure appear after ICE emission and are filled by atomic electrons from higher shells than the vacancy, resulting in x-rays and Auger electrons.

From gadolinium-neutron capture, x-rays and Auger electrons are radiated in the range 0-50 keV. Table 3.4 lists the emission energies and their probabilities for x-rays and Auger electrons from capture in natural Gd. The most frequently emitted x-ray, with an emission rate of 0.47 nc^{-1} (per neutron capture), have an energy of 43 keV. Auger electrons worth noting are those with energy 35 keV (0.08 nc^{-1}) and 5 keV (0.21 nc^{-1}). In comparison to x-rays, they are less frequent and less energetic. [2]

Table 3.4: X-ray and Auger electron (Ae^-) emission rate from capture in natural Gd [2].

Reaction product energy (keV)	Emission rate (nc^{-1})	Reaction product nature
4.8	0.207	Ae^-
6.1	0.053	x-ray
6.7	0.033	x-ray
7.1	0.011	x-ray
7.8	0.006	x-ray
34.9	0.077	Ae^-
42.3	0.264	x-ray
43	0.476	x-ray
48.7	0.147	x-ray
50	0.042	x-ray

Detectors that implement Gd as neutron converter material rely on Gd-neutron capture's reaction products to generate a signal. In thin solid-state detectors, like the ALPIDE, ICEs are the primary signal generating particles. However, also gammas, x-rays, and Auger electrons may contribute to signal generation. A high-Z material, Gd is prone to gamma interaction, which results in the emission of (photo-, Compton, and pair production) electrons and soft K-shell x-rays, which also generate signals in the detector. In a mixed neutron-gamma flux, gamma-interference with neutron signals may arise.

The next two chapters look at neutron detection with a Gd-based semiconductor detector, the ALPIDE. The first (Chapter 4) is a simulation study of thermal-neutron capture in Gd and ICE detection in the detector. The simulations use ideal neutron settings where the neutron source is undisturbed by gammas and consists of mono-energetic thermal neutrons, which have the highest capture cross-section. Electron detection due to gamma interferences in the Gd-foil is studied separately. The second (Chapter 5) puts the detector setup to the test in a real-life neutron environment, which is energetically mixed and infiltrated by gamma radiation. These two chapters aim to estimate the Gd-based ALPIDE's neutron detection efficiency; the former by counting detected ICE and relating the count to neutron absorptions and the latter, attempting to do the same, by filtering out the noise created by the messy neutron environment to get ICE signals alone.

Chapter 4

Simulated Data

Monte Carlo simulations of thermal-neutron capture is presented by this chapter. The simulations study neutron detection efficiency parameters of a Gd-based detector, such as Gd-foil thickness, sensor placement from the Gd-foil and the quality of the neutron source. Also gamma interactions in the Gd-foil giving rise to electrons is investigated.

4.1 Tools

The tools used to simulate and analyze data were Geant4 and ROOT, respectively. Geant4 is specifically developed for the purpose of particle tracking and provides a comprehensive collection of physics processes and databases, and covers a wide energy range (from HEP to eV). The simulation toolkit is based on the C++ programming language, which makes it a versitile and robust tool. Geant4 offers several output formats, one of which is ROOT. [27, 28, 29]

ROOT is a data analysis toolkit developed at CERN for the purpose of HEP experiments. It provides an effective method of analyzing large data files. Both toolkits, Geant4 and ROOT, are freely available for installation on their respective websites ([30] & [31]), alongside comprehensive user manuals.

4.2 Simulation Setup: Geant4 Geometry and Physics

The simulations used the neutron data G4NDL4.5., the gamma level data PhotonEvaporation4.3.2, and the flag G4NEUTRONHP_USE_ONLY_PHOTONEVAPORATION.

The physics list G4HadronPhysicsQGSP_BIC_HP was used for hadron physics. Activated phyics models for electromagnetic physics included G4RadioactiveDecayPhysics, G4EmLivermorePhysics and G4DecayPhysics.

A box of air measuring 30 cm x 30 cm x 30 cm was defined as the world volume. Within the world volume, a target and radiation source was constructed. Depending on the simulation study, the radiation source was either a mono-energetic beam or an isotropic particle source. The mono-energetic particle beam was made of particles travelling parallel to each other and perpendicular to the target. It was positioned 10 cm from and aimed directly towards the target. A certain number of particles with the same kinetic energy were emitted from random positions within the boundaries X $\in$[-5.5 mm, 5.5 mm] and Y $\in$[-5.5 mm, 5.5 mm] which made a 11 mm x 11 mm square. The mono-energetic beam was made of either neutrons or gammas. The neutron beam consisted of 100,000 25 meV neutrons. The gamma beam consisted of 1,000,000 photons. The energies used for the gamma were 0.5 MeV, 2 MeV, and 10 MeV.

The isotropic source was defined as a rectangular parallelepiped. Thermal neutrons (25 meV) were fired at random, position and angle wise, from the parallelepiped's surface. A number of 400,000,000 neutrons were fired from the surface to ensure that a sufficient number of neutrons would strike the target.

The target represented a neutron detector and comprised of three rectangular box volumes: two sensors and a foil. The sensors and the foil were layered in a sandwich configuration (i.e. sensor-foil-sensor). The sensors measured 30 mm x 15 mm x 50 μm and intended to represent ALPIDE, the sensor introduced in section 2.6. A fraction of the sensor volume consisted of an 11 μm thick aluminum layer (which represented readout electronics of the sensor). The remaining sensor volume was made of silicon. A fraction of this silicon volume was defined as a sensitive detector (SD). The sensor SD volume was 25 μm thick and positioned directly behind the aluminum layer. The sensors were positioned along the Z-axis, on opposite sides of origin, and with the aluminum sides (the sensors' front-side) facing each other. The sensors' position on the Z-axis depended on the simulation study.

The foil, like the sensors, was placed along the Z-axis, and had a surface area of 30 mm x 15 mm; the foil and sensors were perfectly aligned and covered the same-sized surface areas. The foil volume was also defined as a SD. The foil thickness and material varied depending on the simulation study. Thicknesses ranged from 5 μm to 30 μm and the foil material was either gadolinium (Gd) or lead (Pb).

Figure 4.1 illustrates a setup within the world volume where the beam is fired perpendicular to the detector target.

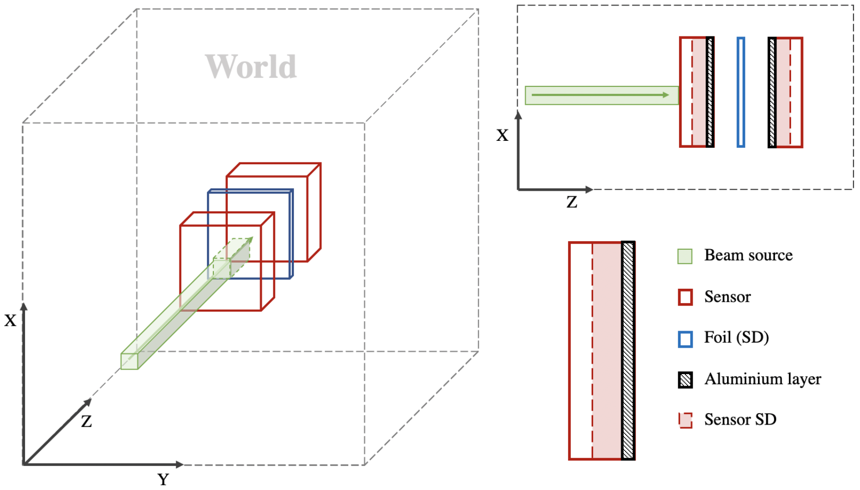

Figure 4.1: Left: The beam source fired perpendicular to the detector target (not to scale). Bottom right: configuration of sensor layers. Top right: XZ-view of beam-irradiated detector.

4.3 Simulations

4.3.1 Optimal Gd-Foil Thickness

A study of optimal converter foil thickness was conducted. The focus of the study was to observe the ICE detection probability for various converter thicknesses. The foil was set to an initial thickness of 5 μm, which was increased stepwise by 5 μm for a total of six simulations. The simulated thicknesses were 5 μm, 10 μm, 15 μm, 20 μm, 25 μm and 30 μm. While increasing the thickness, ALPIDE's position remained the same. The number of detected ICEs was investigated. The number of ICEs detected by the back-irradiated and the front-irradiated ALPIDE's SD was plotted as functions of the foil thickness. In the foil SD, neutrons were scored. Neutron-absorption probability was plotted with respect to foil thickness.

4.3.2 Neutron Detection Efficiency

The neutron detection efficiency was studied for an ideal setup, a realistic setup, and two in-between scenarios. The ideal setup aimed to optimize neutron detection efficiency, while the realistic setup was meant to emulate the (realistic) experimental setup introduced later in Chapter 5. For the ideal setup, the simulated ALPIDE was thinned down to 25 μm so that only the SD remained. The slimmed-down ALPIDE was placed 1 μm from the Gd-foil. After this, it was replaced with the original ALPIDE which was also positioned 1 μm away from the Gd-foil. The difference from the ideal setup was the additional aluminum layer between the SD and the Gd-foil. Taking a step closer to the realistic setup, the ALPIDE was positioned further away, a distance 2500 μm from the Gd-foil. The three setups mentioned above were irradiated by the mono-energetic thermal-neutron beam. The final, realistic setup was identical to the previously described, but instead of the mono-energetic beam, was irradiated by the isotropic thermal-neutron source.

For all the setups, neutron-capture in the Gd-foil was studied. The foil depth at which neutron capture occured was scored. This information was used to plot the neutron-capture profile with respect to the foil thickness. Also, the number of neutron captures resulting in ICE emission was scored. Furthermore, the energy spectrum of the reaction products was studied, and the yield per neutron-capture was calculated. ICEs emitted from the Gd-foil were tracked in the back-irradiated ALPIDE's SD, where the detected ICEs production energy (in the foil), kinetic energy, and energy loss were studied.

With the information provided by the foil SD, the ratio (C_1) of ICEs produced in the foil ($N_{ICE}(foil)$) to neutron captures resulting in ICE production (N_n) was found and defined as

$$C_1 = \frac{N_c}{N_{ICE(foil)}} \tag{4.1}$$

This ratio was used to calculate the neutron detection efficiency of the various setups. The neutron detection efficiency was defined as the ratio (in %) of detected neutrons (i.e., neutron captures resulting in ICE production) to incident neutrons (N).

$$\varepsilon = \frac{N_n}{N} \cdot 100\% \tag{4.2}$$

Nearly 100% of incident neutrons are captured in a 25 μm thick Gd-foil, so the number of incident neutrons was approximated as number of neutron captures (N_c) and the neutron detection efficiency was calculated with ICEs detected per neutron-capture

$$\varepsilon = C_1 \cdot \frac{N_{ICE}}{N_c} \cdot 100\% \tag{4.3}$$

The uncertainty of ε were considered purely statistical. Since the neutron capture count outweighed the number of detected ICEs by a great deal, only error of N_{ICE} was considerable, and

$$\sigma_\varepsilon = \sqrt{(\frac{d\varepsilon}{dN_{ICE}}\sigma_{N_{ICE}})^2} \tag{4.4}$$

4.3.3 Gamma-Interference

Simulations of gamma interactions in metal foils were conducted to study gamma-interference effects on detector measurements. Three different gamma energies were studied: 0.5 MeV, 2 MeV and 10 MeV; with two different metal foils: the 50 μm thick Pb-foil and the 25 μm thick Gd-foil. Electrons generated by gamma interactions in the foil were scored in both the back- and front-irradiated ALPDIE's SD. The detected electrons energy loss distribution and dominating creator process was studied for increasing gamma energies, and the number of electrons emitted from 50 μm Pb and 25 μm Gd was compared.

4.4 Results

4.4.1 Optimal Gd-Foil Thickness

Figure 4.2 illustrates neutron-capture probability with respect to foil thickness. The neutron-capture probability curve showed a rapid growth between Gd-foil thicknesses 5 μm and 10 μm, increasing by 30%. After 10 μm, the curve flattened out and showed little improvement in the range from 15 μm to 30 μm, only increasing by 10%. Figure 4.3 illustrates ICE detection probability measured by the front-irradiated and a back-irradiated ALPIDE. Both detection probability curves showed a similar growth up to Gd-foil thickness 5 μm. With front-irradiation, maximum ICE detection was reached with a 5 μm thick Gd-foil. With thicker foils the probability of detecting an ICE decreased. For the back-irradiated ALPIDE, the efficiency continued to increase after 5 μm. It continued to increase up to 10 μm, but at a decreasing rate as it started to plateau. Little improvement in the ICE detection probability was seen beyond thicknesses greater than 10 μm. Combined, the back- and front-irradiated ALPIDE observed the greatest ICE detection probability for a 5-10 μm thick Gd-foil.

4.4.2 Neutron Detection Efficiency

The depth at which neutrons were captured (the neutron-capture profile) in the 1 μm positioned ALPIDE is illustrated in Figure 4.4. The neutron-capture profile is normalized over all neutron captures and shows the percentage of neutrons captured at a given foil depth. The majority of the neutrons were absorbed within a few μm and the number of neutron captures decreased exponentially with foil thickness. Out of all the neutrons

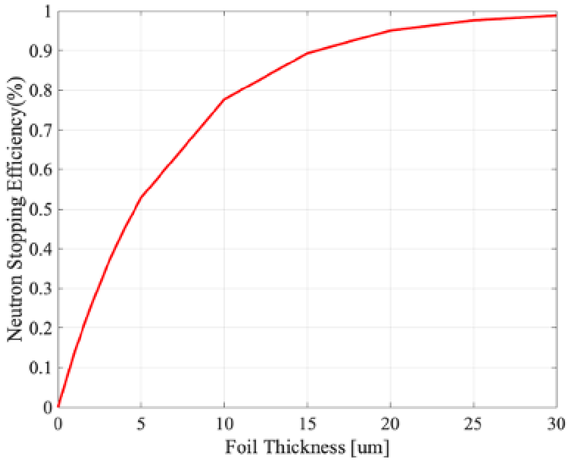

Figure 4.2: Neutron absorption probability as a function of Gd-foil thickness.

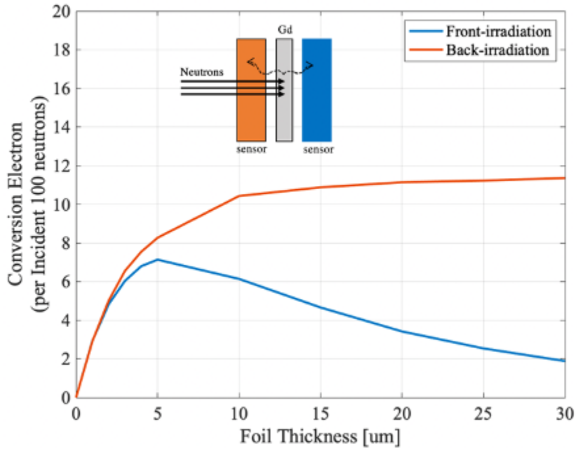

Figure 4.3: ICE detected per hundred neutrons-capture with respect to Gd-foil thickness for a front- and back-irradiated ALPIDE.

fired, 98% were absorbed by the Gd-foil, where 60% of these were after 7 μm and 80% after 10 μm.

Figure 4.5 illustrates the energy spectrum of the prompt gammas produced by Gd-neutron capture. The prompt-gamma yield per neuron-capture (nc^{-1}) was 5.33 nc^{-1}. The prompt gammas were emitted with energies up to 8 MeV and an average energy of 1.49 MeV. The most frequently emitted energies were less than 1 MeV and the single energy 3.7 MeV. The 3.7 MeV spectrum line corresponded to 0.65 nc^{-1} of the emitted prompt gammas. Features of the gamma energy spectrum were not as expected and are discussed in chapter 6.

Figure 4.6 illustrates the energy spectrum of the ICEs produced by Gd-neutron capture. The ICEs clearly showed a discrete energy distribution, which ranged up to 300 keV. The predominate spectrum line was located at 29 keV and showed a yield of 18 nc^{-1}, and spectrum lines in the 71-72 keV range collectively corresponded to an ICE yield of 27 nc^{-1}. The mean energy of the produced ICEs in the 0-300 keV range was 76 keV.

The yield per neutron capture was 0.82 nc^{-1} for ICEs and 5.33 nc^{-1} for prompt gammas. In other words, a batch of 100 captured neutrons resulted in 82 ICEs and 533 prompt gammas. Out of the absorbed neutrons, 69% produced at least one ICE and resulted in 1.18 ICEs on average (Figure 4.7). This value defines C_1

$$C_1 = 1/1.18 \tag{4.5}$$

The foil SD observations were similar for the first three setups irradiated with the mono-energetic neutron beam and are summarized in Table 4.1.

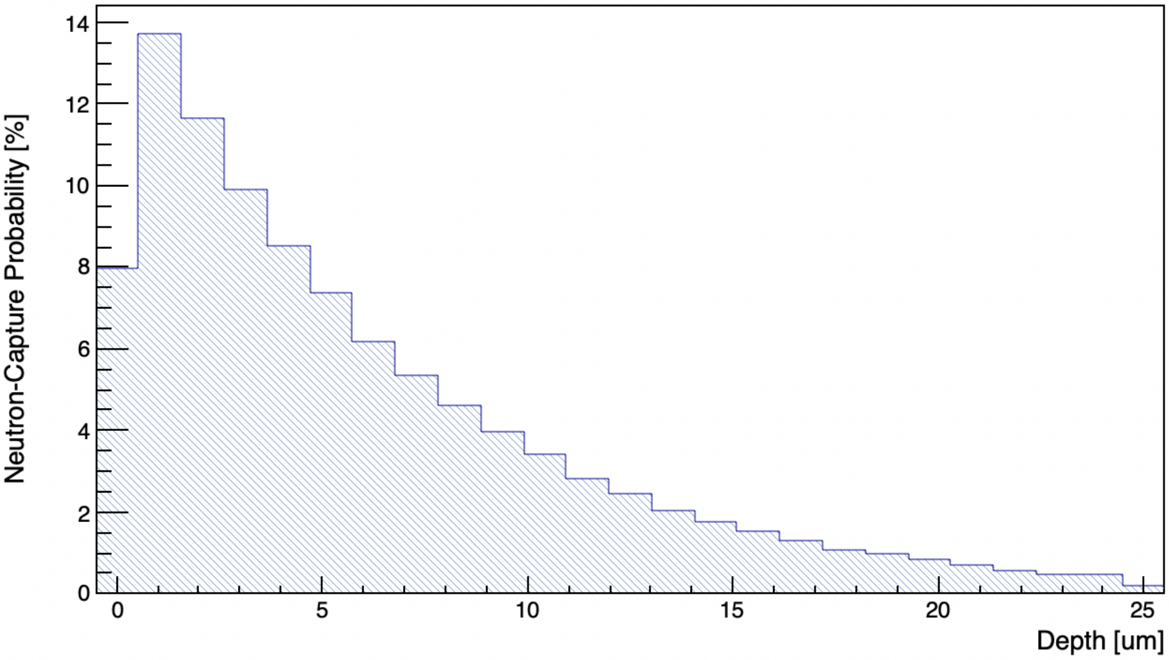

Figure 4.4: Neutron-capture profile normalized on neutron captures in the 25 μm Gd-foil irradiated by the thermal-neutron beam. The probability of neutron capture exponentially decreases with Gd-foil thickness. The integral over all histogram bins is 100%. (Bin size 1 μm)

Table 4.1: Summary, including neutron detection efficiency (ε), of the simulated data for the various setups. First four rows correspond to data collected by the foil SD and the last two rows correspond to data collected in the ALPIDE SD.

	Ideal (1 μm)	ALPIDE (1 μm)	ALPIDE (2500 μm)	Realistic (Iso-source)
ICE yield (nc^{-1})	0.815±0.001	0.824±0.001	0.826±0.001	0.821±0.001
Prompt-gamma yield (nc^{-1})	5.32±0.01	5.33±0.01	5.33±0.01	5.31±0.01
Neutron-captures producing ICEs (nc^{-1})	0.694±0.003	0.700±0.003	0.700±0.003	0.696±0.003
$1/C_1$	1.18±0.01	1.18±0.01	1.18±0.01	1.18±0.01
Detected ICEs (nc^{-1})	0.211±0.002	0.116±0.001	0.099±0.001	0.060±0.001
ε(%)	17.9±0.1	9.85±0.09	8.35±0.09	5.12±0.06

For the isotropic source, ICE and prompt-gamma yield per neutron capture, and percent of neutron-captures producing ICEs were similar to the beam-irradiated setups (see Table 4.1). The major difference between the setups was the neutron-capture profile of the foil irradiated by the isotropic neutron source (Figure 4.8). The isotropic source fired 400,000,000 neutrons out of which only 115,105 (0.03%) struck and were absorbed in the Gd-foil. The neutrons striking the foil did so from all directions and at all angles. Because of this, neutrons entered the foil from both sides, and the capture profile appeared symmetrical. The majority of neutrons were absorbed in the first μms of both sides of the foil. Fewer were absorbed in the center of the foil. The number of capture events decreased exponentially from both sides, like a mirrored version of the beam-irradiated foils capture profile.

The ICEs emitted from the foil were produced with a discrete energy distribution. Figures 4.9-4.12 illustrate energy distributions of the ICEs detected by the different setups. The discrete energy distributions of the ICEs' production energies are presented with subplots in their respective kinetic energy distribution figures.

In the ideal setup, with the thinned-down ALPIDE, only a 1 μm air gap separated the foil and the SD. Figure 4.9a shows the kinetic energy distribution of the ICEs detected by the ideal setup. The detected ICEs kinetic energy was continuous and had peaks that aligned with the corresponding production energy (subplot in Figure 4.9a). It was multi-modal with several sharp peaks which aligned with the discrete peaks of the energies produced inside the foil. The most frequently produced ICEs energies were 29 keV and those in the 70-72 keV range. In the SD, the most common production energies of the detected ICEs were those of the 70-72 keV range, not 29 keV. The intensity of 29 keV ICEs in the ALPIDE's SD was severely reduced from that observed in the foil SD. The average kinetic energy of the detected ICEs was 85 keV. Figure 4.9b illustrates the energy loss of the detected ICEs in the ALPIDE's SD. The deposited energies ranged up to to 200 keV and showed a bimodal distribution. The slightly taller peak was located around 70 keV, and the other, slightly lower peak was located roughly at 14 keV. The taller peak was attributed ICEs with production energies in the 29-90 keV range, while the higher-than 100 keV ICEs caused the other, slightly lower peak. The mentioned peaks of the energy loss distribution are highlighted in the subplots of Figure 4.9b. The ideal setup detected 0.21 ICEs per neutron capture and had a neutron detection efficiency of 18% (using C_1=1/1.18 and equation 4.3.2).

When the thinned-down ALPIDE was replaced with the original ALPIDE, which included the 11 μm thick aluminum layer, no ICEs with production energy of 29 keV were detected and those of energies in the 70-72 keV range were less frequent. The most frequently observed ICEs were those with production energy 131 keV (see subfigure of Figure 4.10a). The kinetic energy distribution of the detected ICEs showed a similar structure to that observed by the ideal setup, having multiple peaks. However, the peaks were less sharp and slightly shifted a few tens of keVs towards lower energies. The average kinetic energy was 97 keV. Figure 4.10b illustrates the energy loss distribution of the detected ICEs. Compared to the former setup, the distribution had a similar shape. However, the previously taller peak located at 70 keV was the lower of the two and was located a few tens of keVs lower, at roughly 50 keV. As before, the peak corresponded to the ICEs of lower production energies, between 70 and 90 keV; and the other peak, located at lower energies, corresponded to the higher production energies, from 131 keV and above. On top of blocking ICEs of low production energies and shifting the observed kinetic energy distribution, the additional aluminum layer reduced the number of detected ICEs per neutron capture, which was 0.12 nc^{-1}. As a result, the neutron detection efficiency of the setup was 10%.

Moving the ALPIDE 2500 μm away from the foil added an extra 2499 μm to the air gap separating the two. This resulted in a further decrease in the number of detected ICEs per neutron capture to 0.10 nc^{-1} and a detection efficiency of 8%. The detected ICEs' production energy, kinetic energy, and energy loss distribution were similar to those previously described but with reduced intensity. This was also the case when the isotropic neutron source irradiated the setup. Similar energy spectrums were also observed with the isotropic neutron source. Irradiated by the isotropic source, the SD detected 0.06 ICEs per neutron capture which gave a detection efficiency of 5%.

4.4.3 Gamma-Interference

Three, increasingly energetic, gamma beams (0.5 MeV, 2 MeV, and 10 MeV) were fired at the 50 μm Pb-foil and the 25 μm Gd-foil. The electrons emitted from the foils and detected by the back- and front-irradiated ALPIDE SDs were created by photon absorption, Compton scattering, and pair production. For the 0.5 MeV beam, the majority of electrons were created from photon absorption in the foil as this is the most probable process for low-energy gammas. In the 50 μm Pb-foil, a batch of 1000 gamma-rays resulted in 1.37 detected electrons, where 61% were photo and 39% were Compton electrons. In the 25 μm Gd-foil, 0.86 electrons per-mile gamma-ray was detected. Half of the detected electrons were created by photon absorption and the rest by Compton scattering. As expected, no electrons were produced by pair-production in either foil as the energy was too low for the process to take place.

Increasing the beam energy to 2 MeV resulted in approximately the same number of detected electrons for the Pb-foil (1.37 per-mile gamma) and slightly decreased for the

Gd-foil (0.69 per-mile gamma). The majority of electrons went from being photo to Compton electrons in both foils. For the Pb-foil, 84% of the detected electrons were Compton. The Gd-foil showed a similar percentage of Compton electrons, specifically 87%. With higher beam energy, electrons also originated from pair-production events. Pair-production electrons of the total number of detected electrons was 9% for the Pb-foil and 8% for the Gd-foil.

As expected, the 10 MeV gamma beam showed a greater pair-production electron yield now that the beam energy had entered the energy domain where pair-production is the dominating process. For the Pb-foil, 71% of the electrons originated from pair production, 28% from Compton scattering, and only 1% from photon absorption. Pair-production electrons were more significant in the Gd-foil, owing to 68% of the electrons detected. The other electrons were 31% Compton and 1% photo. The results of the gamma studies are summarized in Table 4.2.

For all the gamma beam energies, the 50 μm Pb-foil setup displayed an electron yield a constant factor approximately 2 greater than what was observed for the 25 μm Gd-foil setup. This factor defines C_2 where

$$C_2 = 1/2 \tag{4.6}$$

Gamma interactions vs. beam energy are illustrated in Figures 4.13-4.14 for the Gd-foil, and Figures 4.15-4.16 for the Pb-foil. The histograms in these figures show the energy loss distribution of the detected electrons. The energy loss distributions had a similar shape and range. They were right-skewed and unimodal with a single peak located in the low energy range, generally between 0 MeV and 0.04 MeV. The general trend was a larger number of detected electrons for higher beam energies. The most energetic beam (10 MeV) resulted in the most detected electrons.

Table 4.2: Total, photo, compton, and pair-production electrons detected by ALPIDE per-mille (‰) gamma incident on the metal foil for increasing gamma energy.

50 μm Pb-foil

Energy (MeV)	**Total (‰)**	**Phot. (‰)**	**Compt. (‰)**	**Pair (‰)**
0.5	1.37	0.83	0.54	0.00
2	1.37	0.09	1.15	0.13
10	1.71	0.01	0.48	1.22

25 μm Gd-foil

Energy (MeV)	**Total (‰)**	**Phot. (‰)**	**Compt. (‰)**	**Pair (‰)**
0.5	0.86	0.43	0.43	0.00
2	0.69	0.02	0.60	0.06
10	0.84	0.01	0.26	0.57

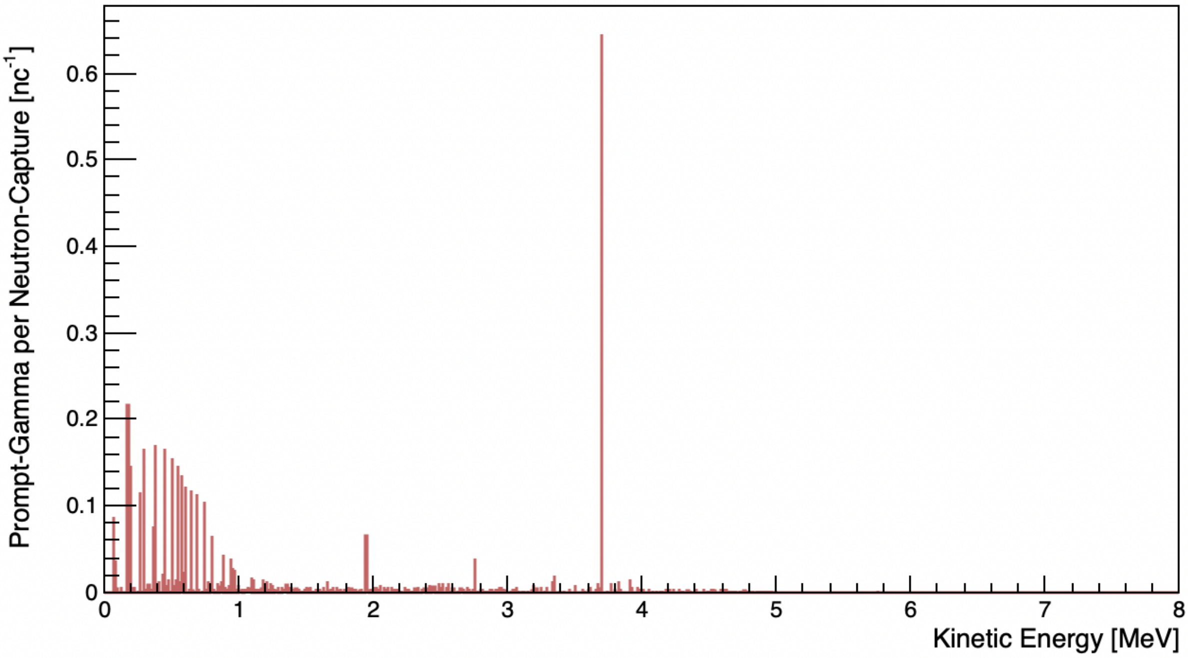

Figure 4.5: Kinetic energy distribution of prompt-gamma rays produced by thermal-neutron capture in the 25 μm Gd-foil. (Bin size 1 keV)

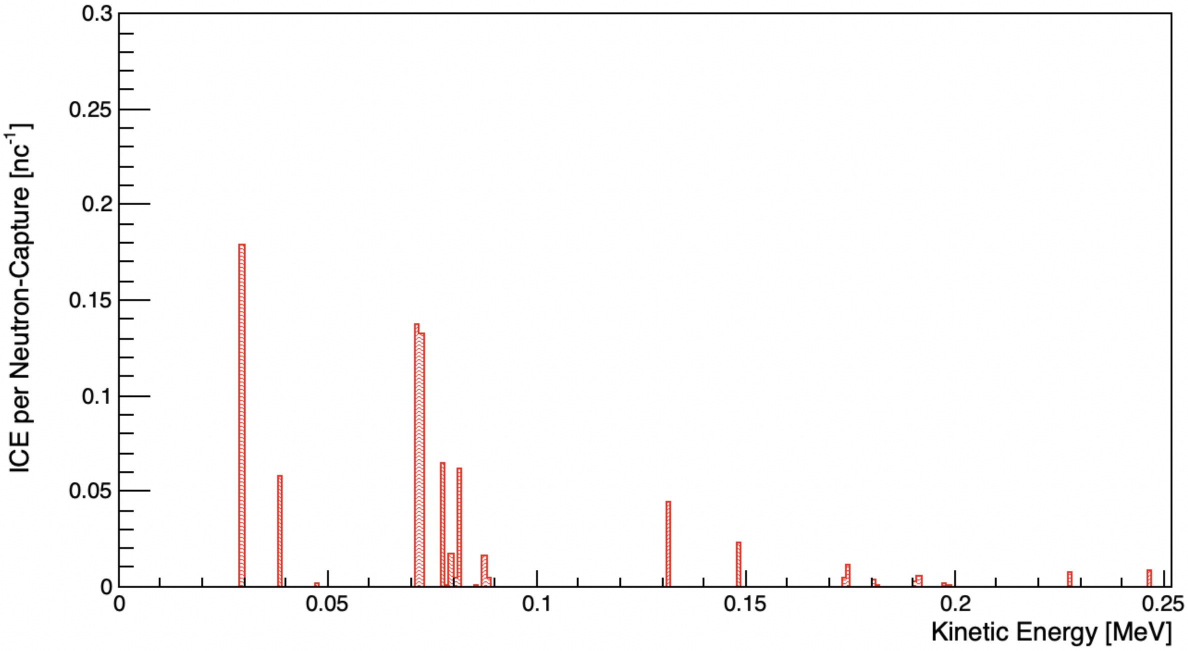

Figure 4.6: Kinetic energy distribution of ICEs produced by thermal-neutron capture in the 25 μm Gd-foil. (Bin size 1 keV)

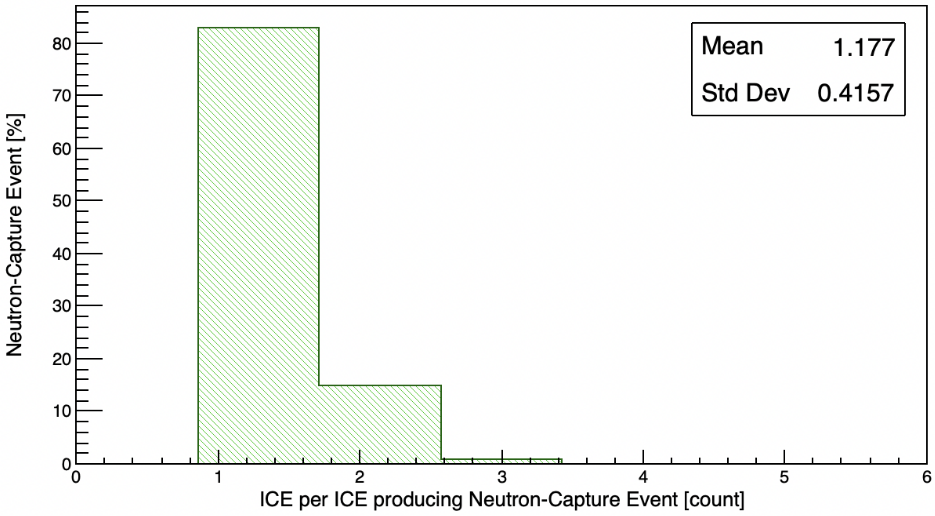

Figure 4.7: The number ICEs produced per neutron capture producing ICEs normalized over the latter.

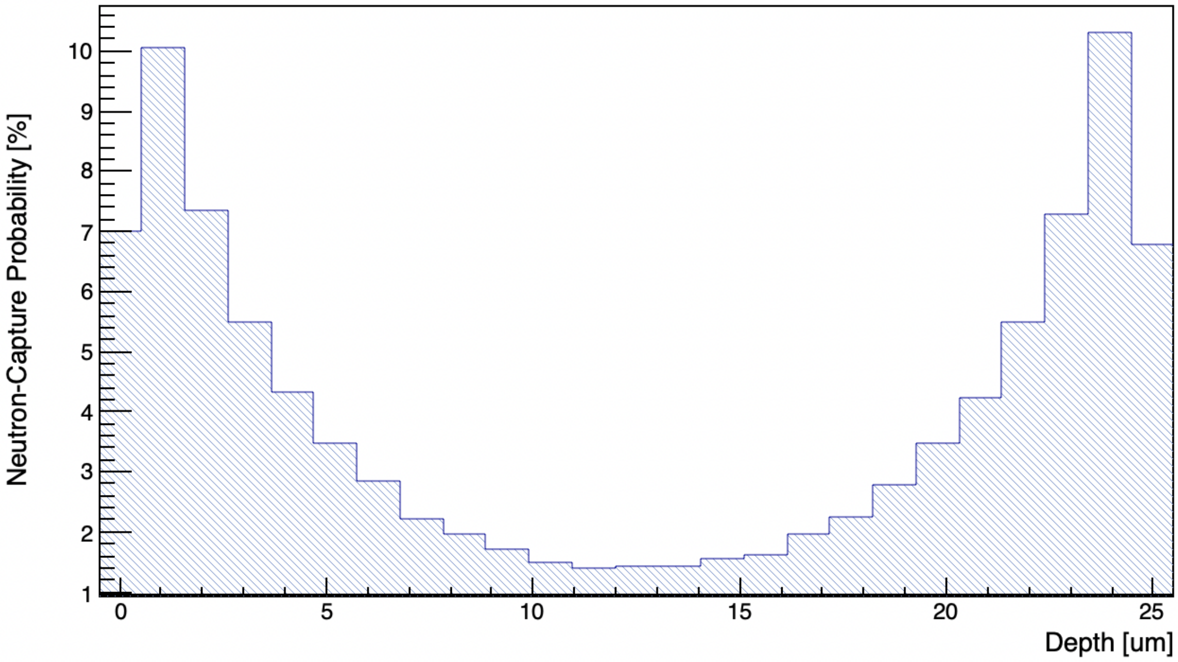

Figure 4.8: Neutron-capture profile in the 25 μm Gd-foil irradiated by the isotropic thermal-neutron source. (Bin size 1 μm)

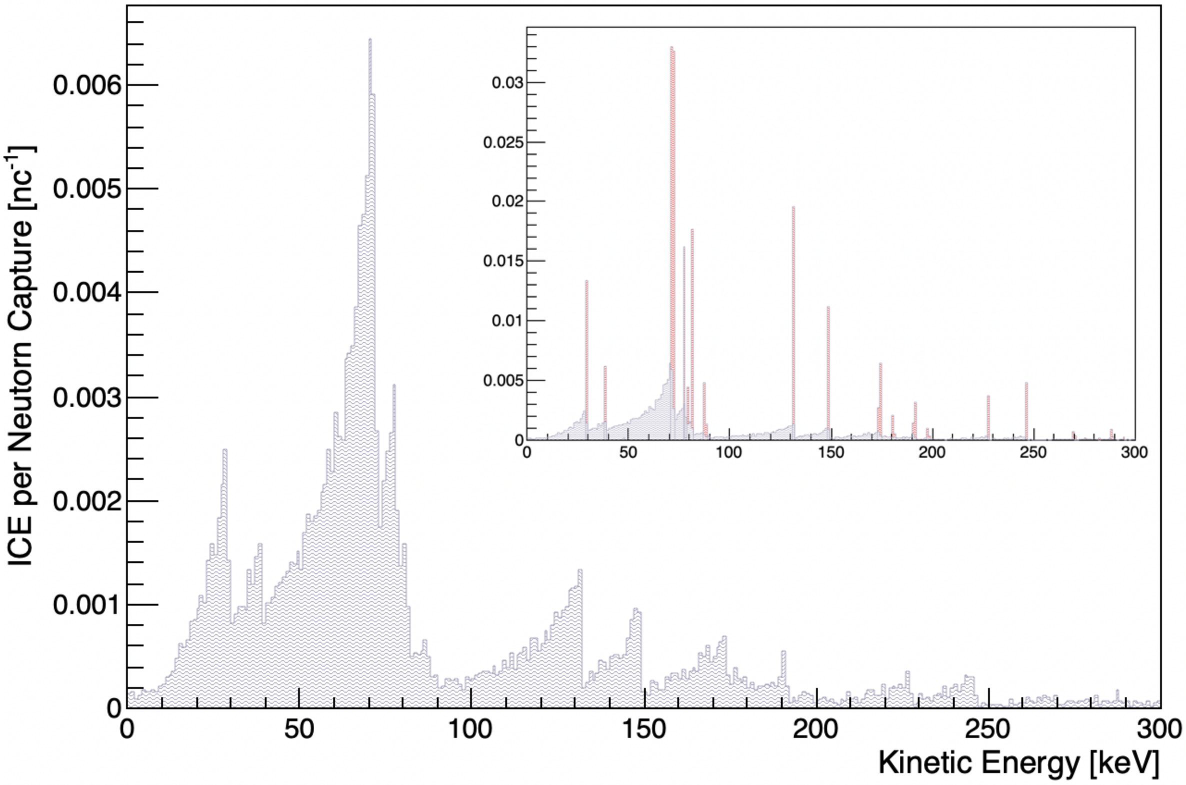

(a) Kinetic energy distribution. Subplot: Kinetic energy merged with corresponding production energy distribution.

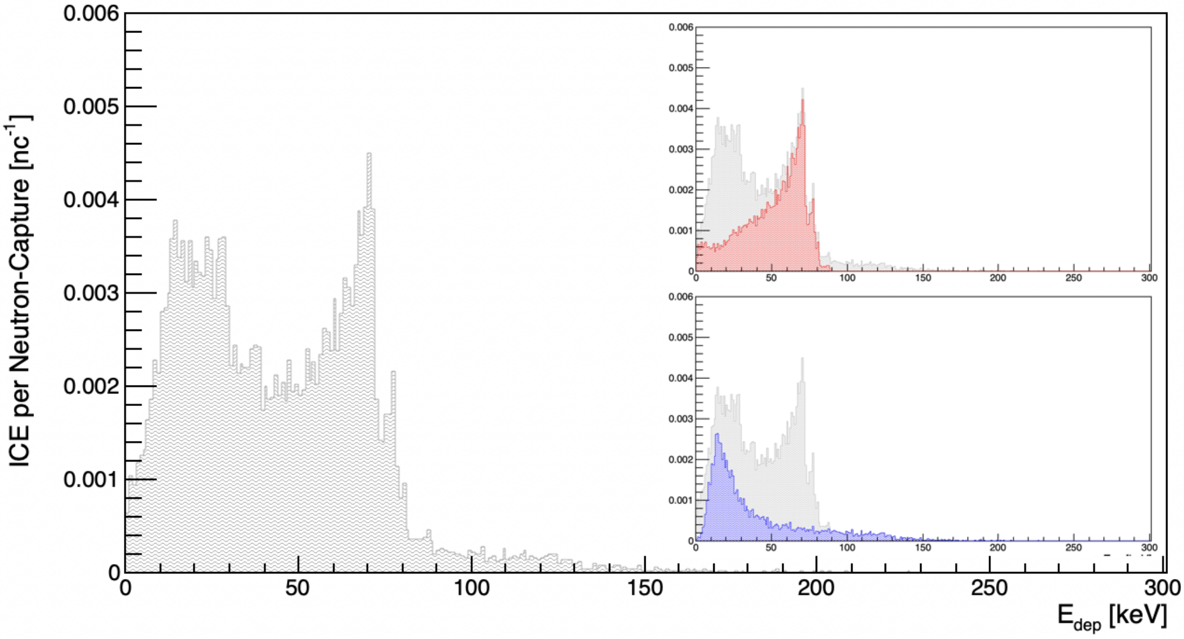

(b) Energy loss distribution. Subplots: Energy loss of ICEs with production energies between 29-90 keV (top) and higher than 131 keV (bottom).

Figure 4.9: ICEs energy distributions (bin size 1 keV) corresponding to the back-irradiated thinned ALPIDE positioned 1 μm from the Gd-foil (irradiated by the thermal-neutron beam).

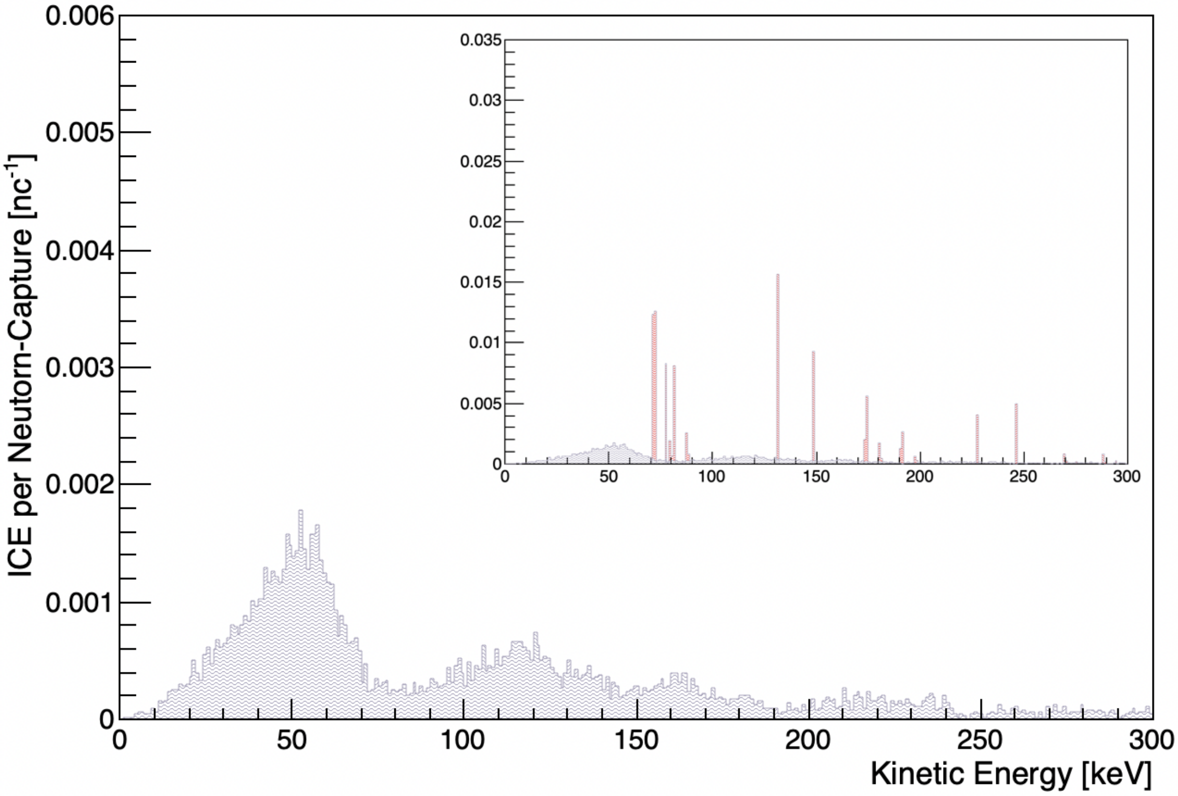

(a) Kinetic energy distribution. Subplot: Kinetic energy merged with corresponding production energy distribution.

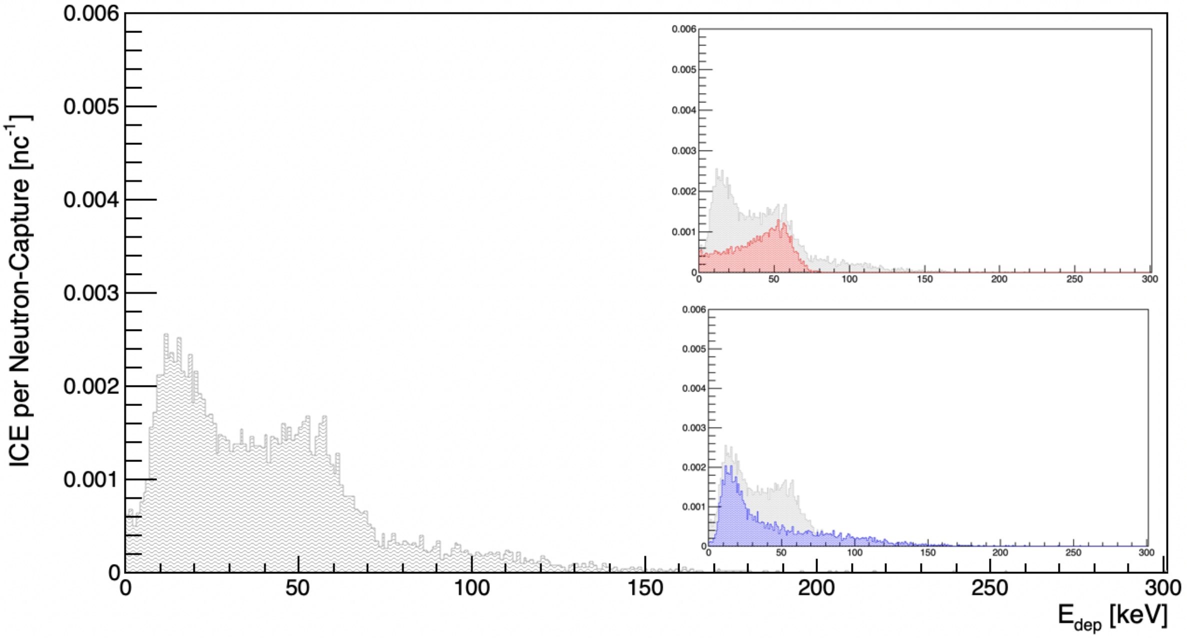

(b) Energy loss distribution. Subplots: Energy loss of ICEs with production energies between 70-90 keV (top) and higher than 131 keV (bottom).

Figure 4.10: ICEs energy distributions (bin size 1 keV) corresponding to the back-irradiated standard ALPIDE positioned 1 μm from the Gd-foil (irradiated by the thermal-neutron beam).

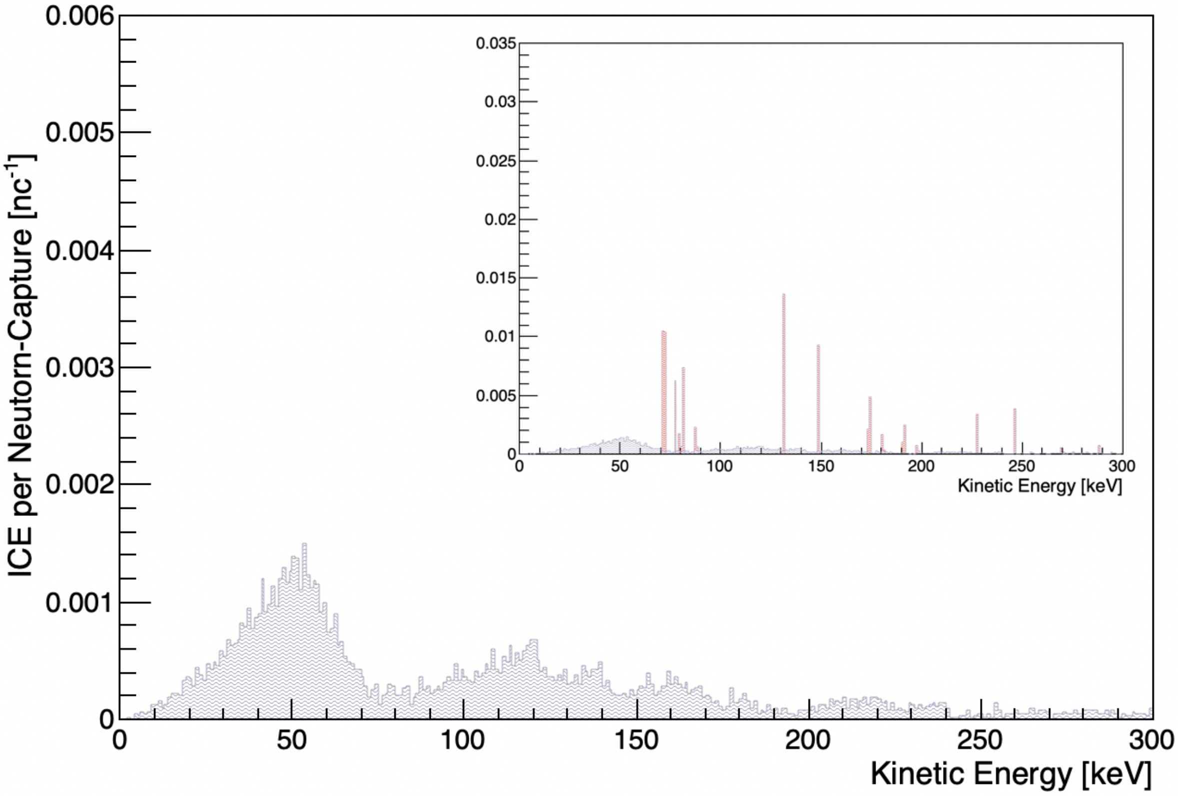

(a) Kinetic energy distribution. Subplot: Kinetic energy merged with corresponding production energy distribution.

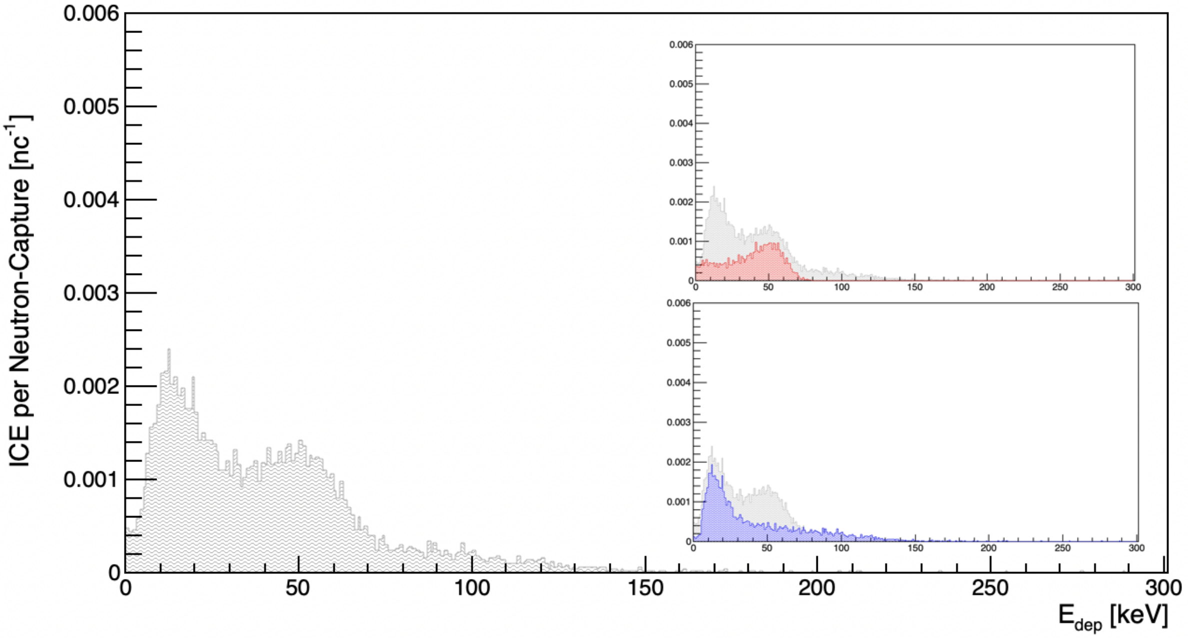

(b) Energy loss distribution. Subplots: Energy loss of ICEs with production energies between 70-90 keV (top) and higher than 131 keV (bottom).

Figure 4.11: ICEs energy distributions (bin size 1 keV) corresponding to the back-irradiated standard ALPIDE positioned 2500 μm from the Gd-foil (irradiated by the thermal-neutron beam).

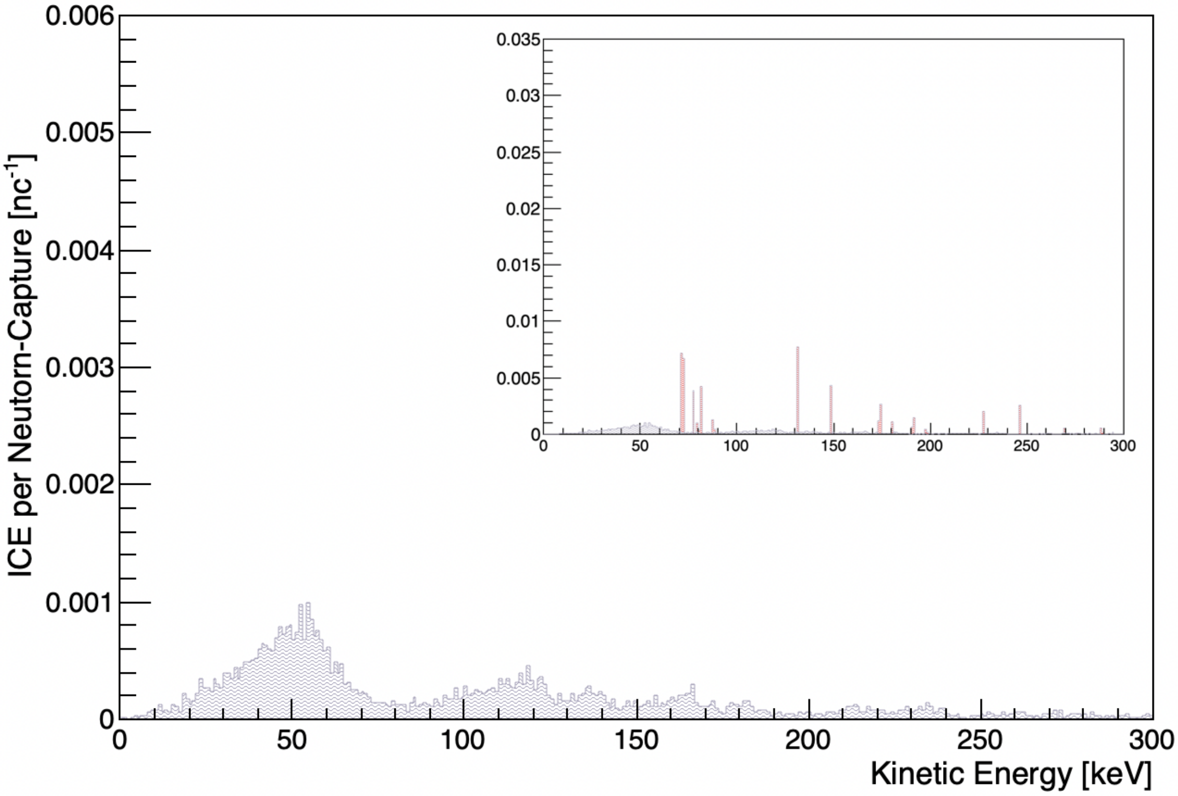

(a) Kinetic energy distribution. Subplot: Kinetic energy merged with corresponding production energy distribution.

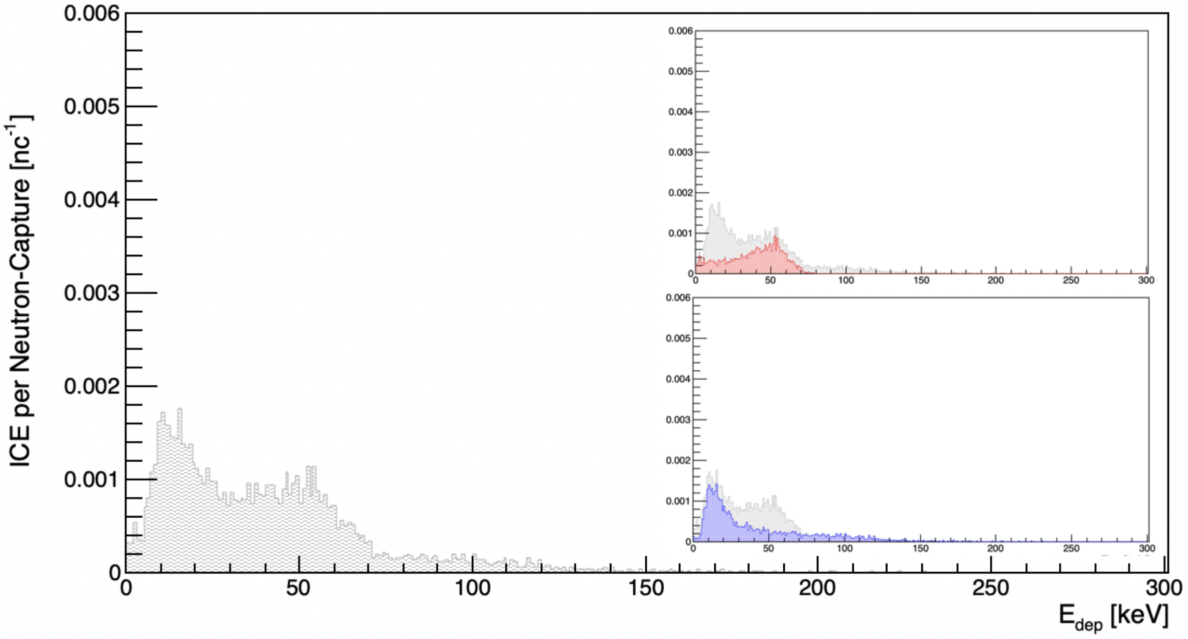

(b) Energy loss distribution. Subplots: Energy loss of ICEs with production energies between 70-90 keV (top) and higher than 131 keV (bottom).

Figure 4.12: ICEs energy distributions (bin size 1 keV) corresponding to the back-irradiated standard ALPIDE positioned 2500 μm from the Gd-foil (irradiated by the isotropic thermal-neutron source).

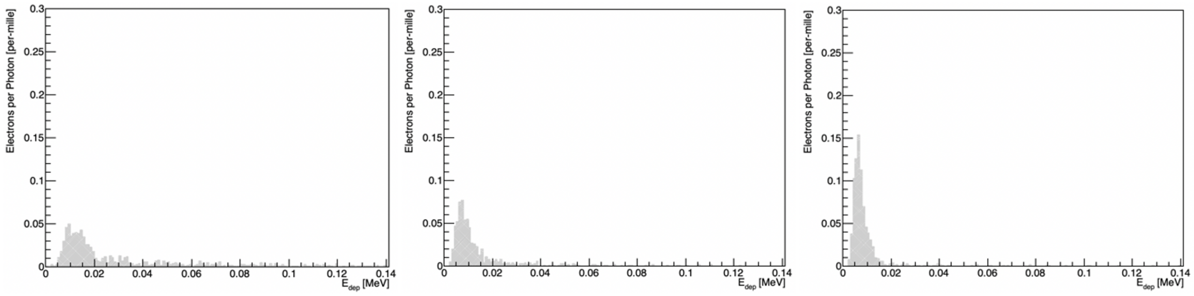

(a) 0.5 MeV *(b) 2 MeV* *(c) 10 MeV*

Figure 4.13: Detected electrons energy loss distribution for the 25 μm Gd-foil irradiated by the mono-energetic gamma beam

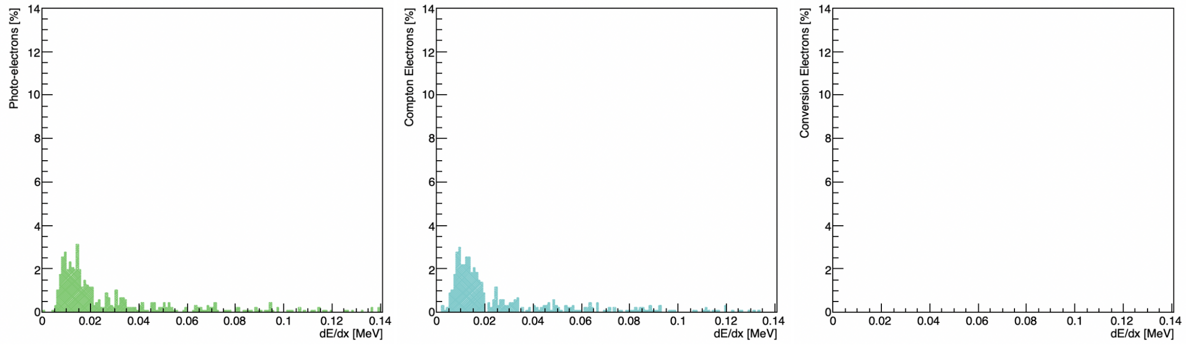

(a) photo *(b) compt* *(c) pair*

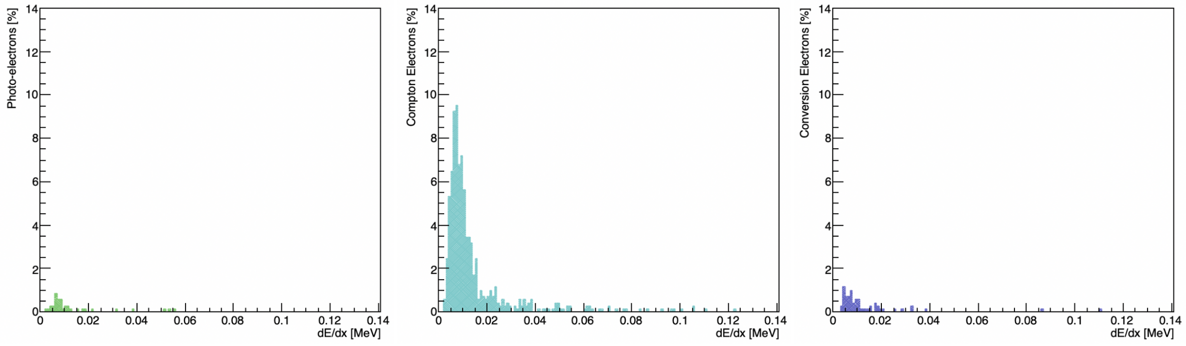

(d) photo *(e) compt* *(f) pair*

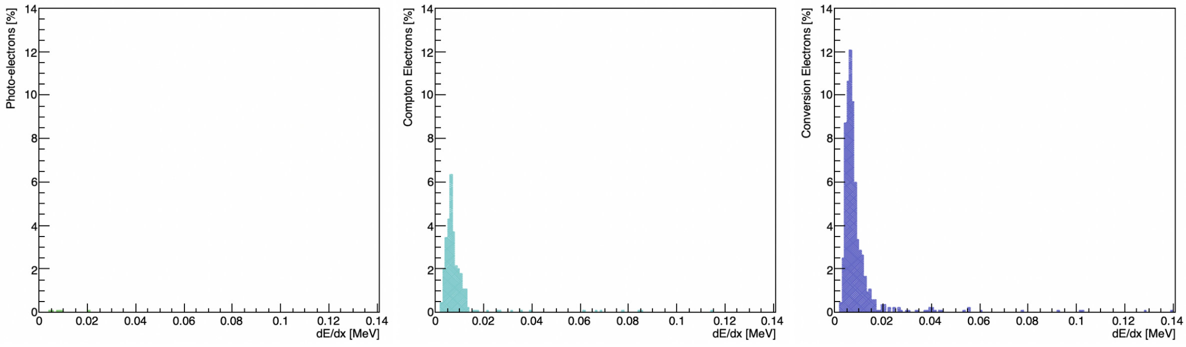

(g) photo *(h) compt* *(i) pair*

Figure 4.14: The 25 μm Gd-foil irradiated by the mono-energetic gamma beam: 0.5 MeV (a-c), 2 MeV (d-f), and 10 MeV (g-i)

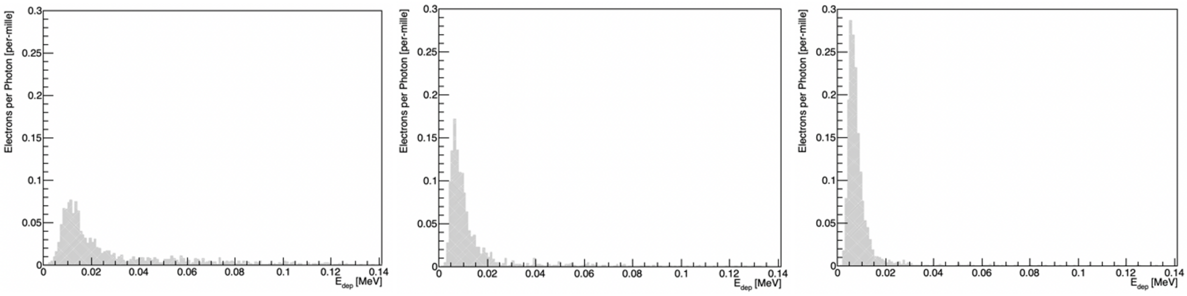

(a) 0.5 MeV (b) 2 MeV (c) 10 MeV

Figure 4.15: Detected electrons energy loss distribution for the 50 μm Pb-foil irradiated by the mono-energetic gamma beam

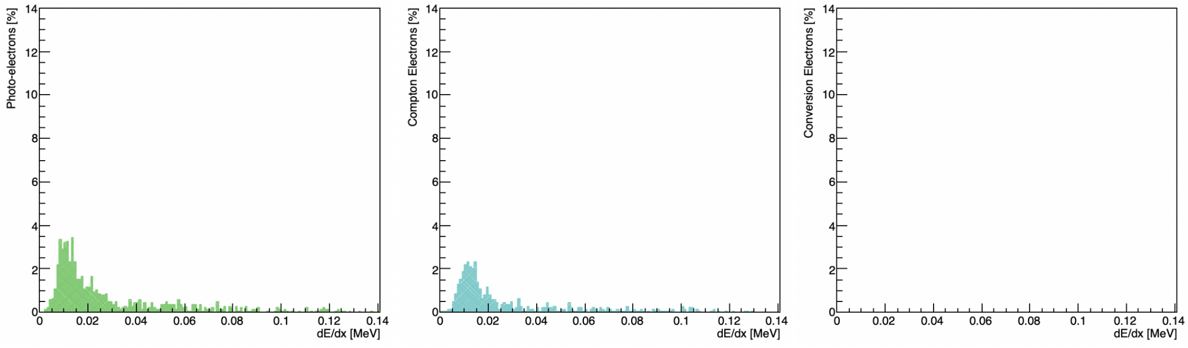

(a) photo (b) compt (c) pair

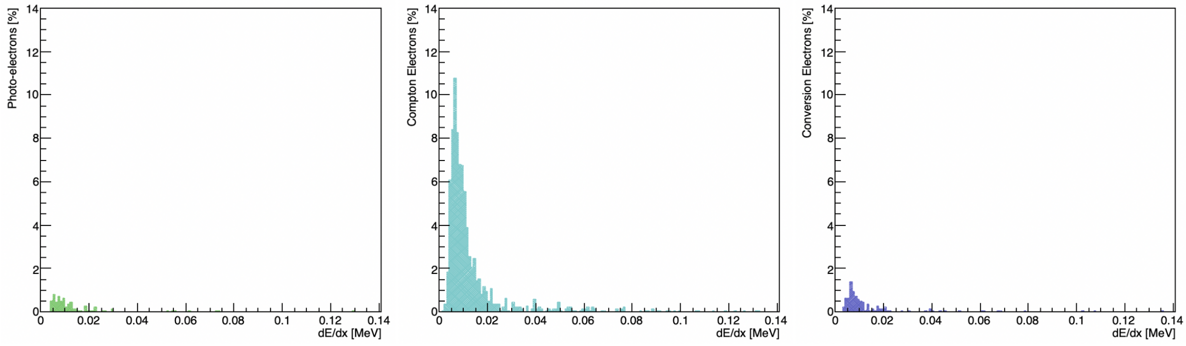

(d) photo (e) compt (f) pair

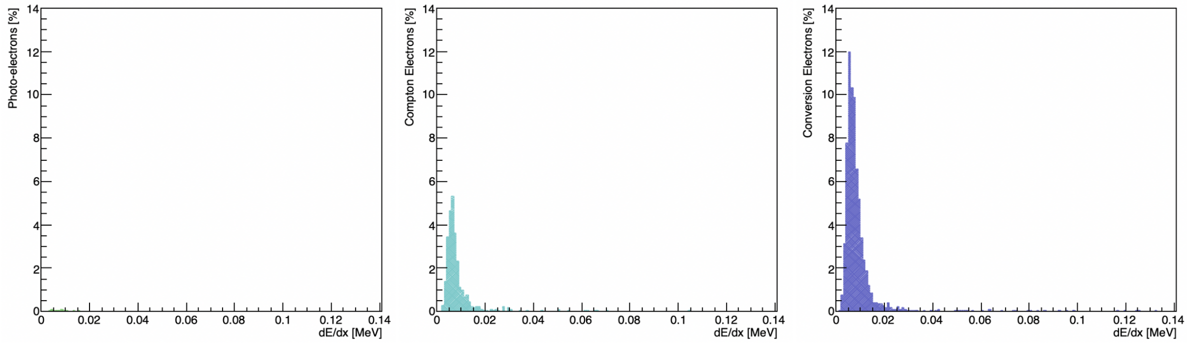

(g) photo (h) compt (i) pair

Figure 4.16: The 50 μm Pb-foil irradiated by the mono-energetic gamma beam: 0.5 MeV (a-c), 2 MeV (d-f), and 10 MeV (g-i)

Chapter 5

Experimental Data

A neutron detector was constructed and tested in a thermal neutron flux. The thermal neutron flux was artificially created by thermalizing the fast neutron flux surrounding an operating positron emission tomography (PET) cyclotron. The constructed detector implemented ALPIDE and a Gd-foil. Here, the results of these tests and the efficiency of the neutron detector are presented.

Different measurements were needed to calculate detection efficiency. Experimental data were acquired utilizing the ALPIDE with or without Gd-foil. A measurement with ALPIDE and a lead foil was performed to study the effects of gamma interactions in metal. The result of this measurement was used to correct for gamma interference in the Gd-covered sensor measurements. Furthermore, a measurement with a plastic film placed between the Gd-foil and ALPIDE was performed to test if electrons could be effectively stopped by plastic.

Foreword

Experimental data were acquired on the 25th of October 2020, during a period under exceptional circumstances, due to a worldwide pandemic. The pandemic introduced difficulties to the thesis, and most noticeably to the experimental aspect of the project. The original plan involved traveling to European Spallation Source (ESS) in Lund, Sweden, to test the detector setup under ideal conditions, utilizing their clean, monoenergetic thermal neutron beam. However, due to travel restrictions and other inconveniences brought by the pandemic, in early 2020, this was no longer an option, and alternative neutron sources had to be considered. The considered alternatives were the Budapest Research Reactor (BRR) [32] in Budapest, Hungary, and the JEEP II reactor [33] at Kjeller, Norway. Because of travel restrictions, the BRR was out of the picture. In April 2020, the IFE (Institute for Energy Technology) committee decided to permanently close operations at the reactor due to technical and economic conditions [34]. After some consideration, the PET-cyclotron of the local PET-center at Haukeland, in Bergen, was deemed the most practical neutron source at the time.

5.1 Tools and ALPIDE Measurement Setups

The Neutron Source: Neutrons From F-18 Production in a PET Cyclotron

A PET cyclotron was used as a neutron source. A PET cyclotron producing F-18, a radioactive isotope used for PET imaging, generates large amounts of radiation. The isotope is a product of a nuclear reaction involving a proton and an O-18 target

$$p +^{18} O \rightarrow^{18} F + n \tag{5.1}$$

The intensity the protons beam affects the neutrons' emission rate (i.e., the neutron flux). The neutrons emitted from the nuclear reaction are fast neutrons. A multitude of reports refers to the neutron flux surrounding PET cyclotrons during F-18 production [35, 36, 37, 38]. Inside the room which the cyclotron is placed, the neutron energy varies depending on where in the room it is measured. It is in the MeV range, and can be as much as 16 MeV [39]. In addition to fast neutrons, also bremsstrahlung, beta, and gamma rays are produced during cyclotron operation [40]. This additional radiation creates a mixed environment undesired from a neutron detector's viewpoint whose objective is to observe thermal neutrons.

The PET cyclotron used in this experiment was a *PETtrace* of GE Healthcare. The *PETtrace* cyclotron is located in a concrete bunker whose room size is 4x4.5 m^2, and the height is 2.5 m. The thickness of the concrete walls is about 1.6 m.

The radiation fields surrounding *PETtrace* has been documented [41]. Calculations have been performed for the radiation field accompanying F-18 production with a 40 μA beam current of 15 MeV protons. Operating *PETtrace* produces a flux of high-energy neutrons, which are attenuated in shielding materials such as silver (in the target container), copper, aluminum, silica, stainless steel, lead, and concrete (the bunker walls). The neutron fluxes are not very well thermalized especially close to the target area.

ALPIDE Measurement Setups

The neutron detector's fundamental components were ALPIDE (whose features are reported in section 2.6) and a 25 μm Gd-foil. A rectangular metal structure was used as a support frame onto which the ALPIDE-foil configuration was assembled. It had a thick base, four support rods, and two rectangular endplates with a hole in each corner. The support rods were inserted into the holes of the endplates. Two plates were slid onto the support rods. The first plate, a carrier board on which the ALPIDE chip was mounted, and the second, an aluminum (Al) plate with an ALPIDE sized window. A front- and side view of the metal frame with the ALPIDE carrier board and the Al-plate is reported in Figure 5.1 and 5.2. Approximately two-thirds of the Al-plate window (width-wise) was covered by the Gd-foil, which was fastened with plastic tape. Screws and plastic spacers were used to fasten and secure the carrier board, and the Al-plate to the metal frame. The distance between ALPIDE and the Gd-foil was 2.5 mm.

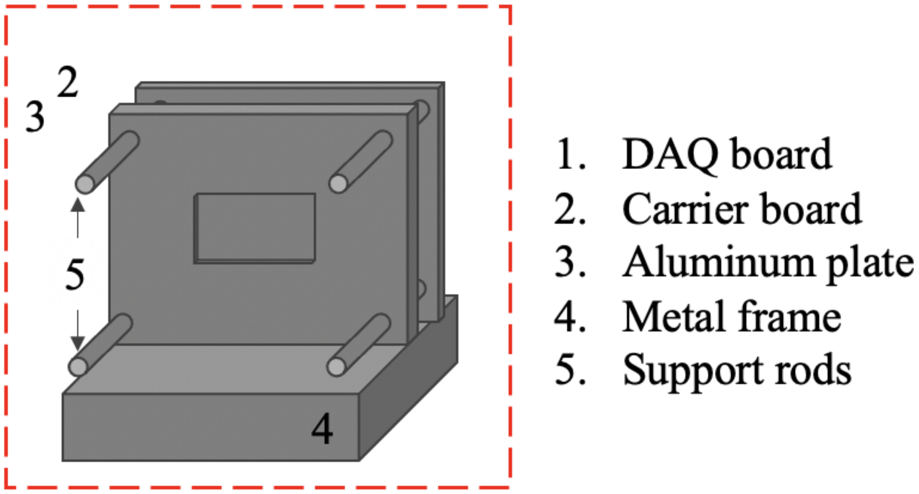

Figure 5.1: Front view of the metal fram used to support the ALPIDE carrier board and the Al-plate. From this angle, the Al-plate is infront of the carrier board.

Other materials were also used to cover the Al-plate window, including a 50 μm lead (Pb) foil and a thin plastic layer (whose specific material and thickness was not documented). When the Pb-foil was used, it was placed over the Al-plate window which was not covered by the Gd-foil. With both metal foils, the Al-plate window was completely blocked, and ALPIDE was covered entirely. When the plastic layer was used, the Pb-foil was removed and the plastic taped over the whole Al-plate window, with the Gd-foil still in place. The different layer configurations are illustrated in Figure 5.3.

The ALPIDE carrier board was connected to a DAQ board. The DAQ board was programmed to acquire data in bursts, where one burst contained 100 STROBEs, and the STROBE period was 50 μs. With these settings, the DAQ was effectively ON for

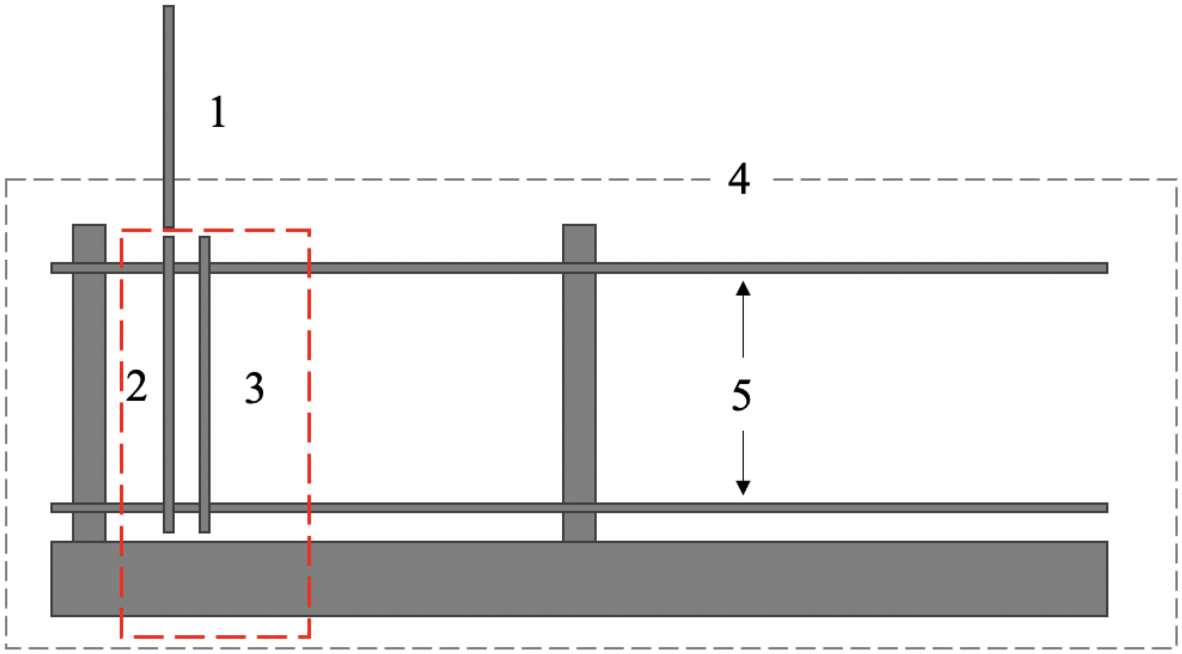

Figure 5.2: Side view of the metal frame used to support the ALPIDE carrier board and the Al-plate. (1) DAQ board, (2) carrier board, (3) Al-plate, (4) Metal frame, and (5) Support rods

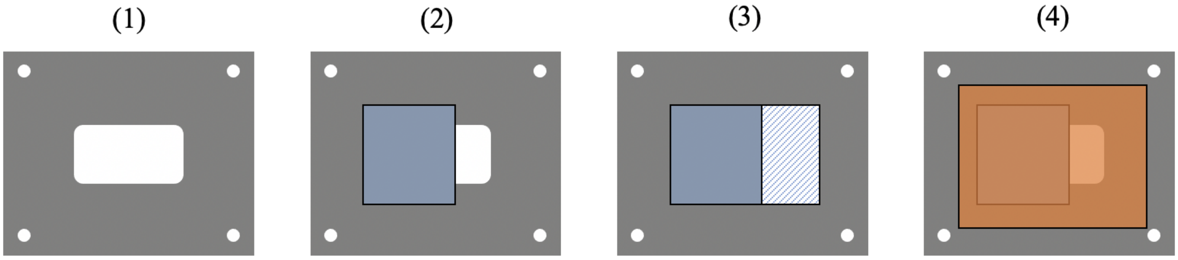

Figure 5.3: Layer configurations of the (1) Al-plate, with an ALPIDE sized window at its center; (2) two-thirds of the window covered by a 25 μm Gd-foil; (3) same as (2) and a 50 μm Pb-foil covering the remaining one-third; (4) same as (2) and a plastic layer covering both the Gd-foil and the remaining one-third.

50 μs $\cdot 100 = 5$ ms. After acquiring data, the DAQ was OFF for 100 ms to copy the data to the computer. Two types of measurements were executed with the prototype, preliminary and final measurements. The final measurements used a STROBE period as described above, and the preliminary measurements used a shorter STROBE period of 5 μs. No reverse bias (V_BB=0) was used. ALPIDE's configuration file is reported in Appendix B.

5.2 Method

5.2.1 Neutron Flux Testing and ALPIDE Measurements

The experimental data were acquired in two different sessions. The first lasted 5 hours and was spent getting acquainted with the PET bunker's neutron environment and taking preliminary measurements with ALPIDE. The second, also 5 hours long, was spent taking flux measurements and final measurements with ALPIDE.

Neutron Flux Measurements

Neutron Survey Meter Model 488A [42] was used to monitor the neutron flux produced by the *PETtrace*. It is a portable pulse count-rate meter based on a boron lined proportional counting detector tube to detect thermal neutrons. It comes with an attachable moderator and cadmium shield that extends the instrument's energy range and allows a swift estimate of the present neutron spectrum. Read on the 488A survey meter, the thermal-neutron sensitivity of the detector tube alone is 12, 120, 1200 or 120000 $n/cm^2/s$ (thermal). Its accuracy is $\pm 20\%$ of full-scale indication.

During the first experimental run, several flux measurements were taken in various locations. The flux was observed at 90°, 150°, and 180° with respect to the cyclotron (see Figure 5.4). The thermal-neutron flux, and sometimes the combined thermal-fast and fast-neutron count were measured. Fast neutrons were given in counts/m (which was converted to counts/s) and thermal neutrons were given in flux units ($n/cm^2/s$). For all the measurements, the proton beam current was operated at the lowest setting, 1 μA. At 90°, the thermal-neutron flux was larger than $12 \cdot 10^3$ $n/cm^2/s$ and the combined thermal-fast neutron count was larger than $1.3 \cdot 10^4$ c/s. In hopes of less intense neutron flux, the neutron survey meter was moved to an angle of approximately 150°, slightly behind the cyclotron where it measured a thermal-neutron flux of $9 \cdot 10^3$ $n/cm^2/s$ and a combined thermal-fast neutron count similar to the previous position. The neutron survey meter was then moved to 180°, directly behind the cyclotron, and measured the same thermal-neutron flux as the previous position. Neither the combined thermal-fast nor the fast-neutron count was measured at this position, and no more positions were explored due to time constraints. It was decided that ALPIDE measurements would take placed at 180°, behind the cyclotron.

A cave made of plastic boxes was built to prevent background radiation to interfere and possibly damage the ALPIDE chip. The cave's plastic walls also blocked thermal neutrons and thermalized fast neutrons so that mostly thermal neutrons roamed the space within. The thicknesses of the blocks were approximately 30 cm and 5 cm. One of the cave walls was built using the thinnest block and the other three walls and the lid

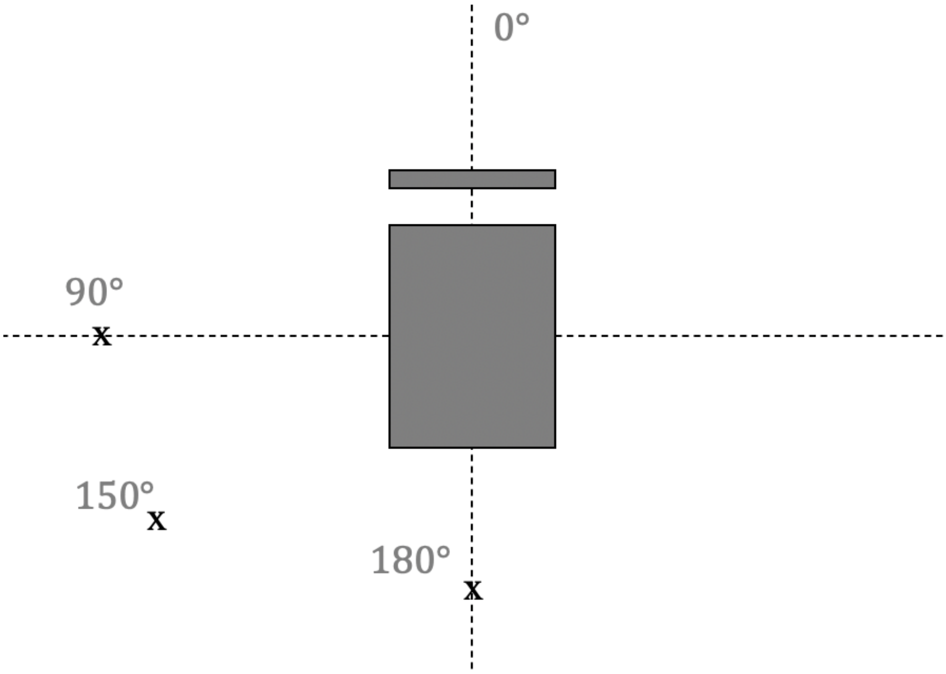

Figure 5.4: Position of neutron flux measurements with respect to the cyclotron body.

with the thicker blocks. The cave was built behind the cyclotron with the thinnest cave wall facing the cyclotron. An image of the cave setup is shown in Figure 5.5.

Inside the cave, the measured thermal-neutron flux was 5000 n/cm^2/s and the fast-neutron count was 833 counts/s.

Preliminary ALPIDE Measurements

Finally, ALPIDE was placed inside the plastic box for some preliminary measurements. A few were carried out, seeing that the session was nearing its end. The DAQ was programmed with a STROBE period of 5 μs, and the metal frame with ALPIDE was placed inside the plastic cave. The cave was slightly expanded to fit the setup inside since it was slightly bigger than the neutron survey meter. The neutron flux was measured with the neutron survey meter to check if the flux was affected by the increased cave volume. It was not. Two preliminary ALPIDE measurements were executed. The first was with the Gd-foil covering ALPIDE and the other with just ALPIDE, uncovered. The first measurements lasted for 36 min and the second for 14 min. These measurements showed encouraging results. The Gd-covered ALPIDE detected significantly more particles than the uncovered ALPIDE and confirmed that the Gd-foil could, to some extent, could be used to indicate thermal neutrons. At the end of the first session, ALPIDE setup was dismantled, and the plastic cave disassembled.

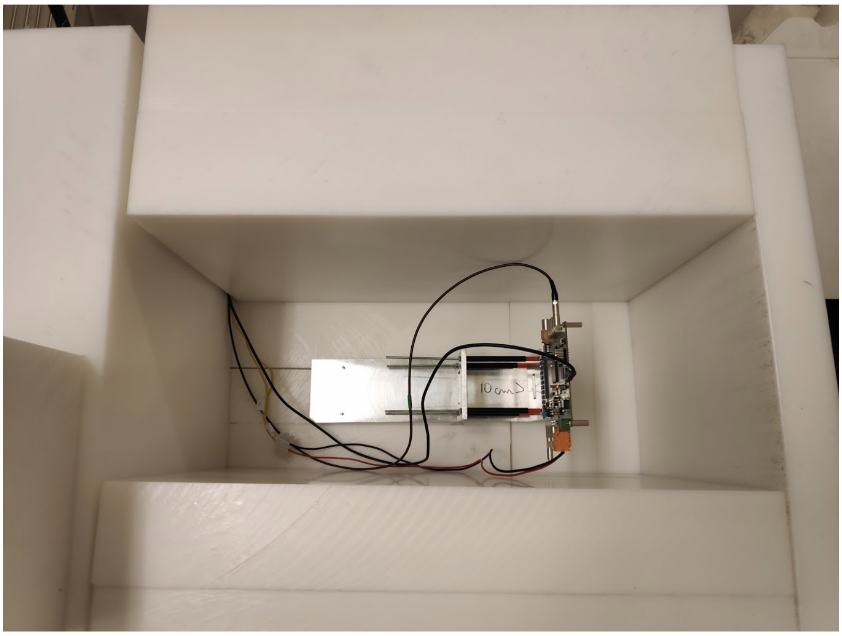

Figure 5.5: A photograph of the rectangular plastic cave built to thermalize fast neutrons and protect the prototype setup from radiation damage. The thicker walls were 30 cm, and the thinnest wall was 5 cm. Here, the thinnest wall is facing the cyclotron. (A thick plastic block was put on top and closed off the cave opening, also 30 cm thick.)

Final ALPIDE Measurements

During the second session, final ALPIDE measurements were carried out. First, a plastic cave was built, similar to the one of the first visit. This time, the thin cave wall faced the back of the room and away from the cyclotron. The neutron survey meters response time was set to “fast” and the scale to x1000. Inside the cave and with a beam current of 5 μA, the neutron survey meter observed a thermal-neutron flux of 7000 n/cm^2/s and a fast-neutron count 833 counts/s. The beam current was larger than the one used during the first visit, and as a result, so was the thermal-neutron flux. The fast-neutron count, 833 counts/s, seemed to be unaffected by the increased beam current and was the same as the first visit.

For the final set of ALPIDE measurements, the DAQ was programmed with a STROBE period of 50 μs. For the first measurement, the beam current was OFF, and ALPIDE was left uncovered. The measurement lasted for 10 min. For the second, two-thirds of ALPIDE was covered by the Gd-foil; for the thirds, two-thirds stayed covered by the Gd-foil while the Pb-foil covered the remaining one-thirds; and for the four and final, the Pb-foil was removed and the plastic layer applied over the Gd-foil and the uncovered ALPIDE area. These measurements utilized a beam current of 5 μA and lasted for 20 min. Only one measurement was carried out with each setup.

Effective run time

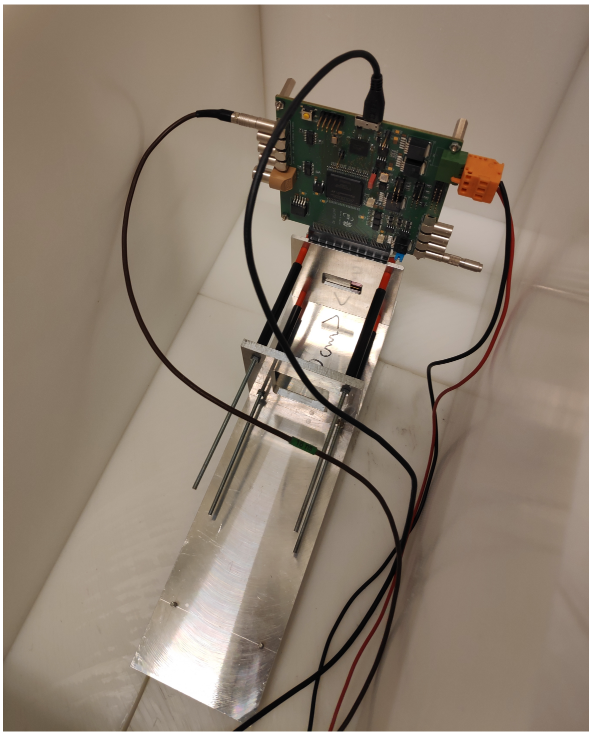

Figure 5.6: Inside the plastic cave, the metal frame with ALPIDE carrier board (not visible) connected to the DAQ (visible).

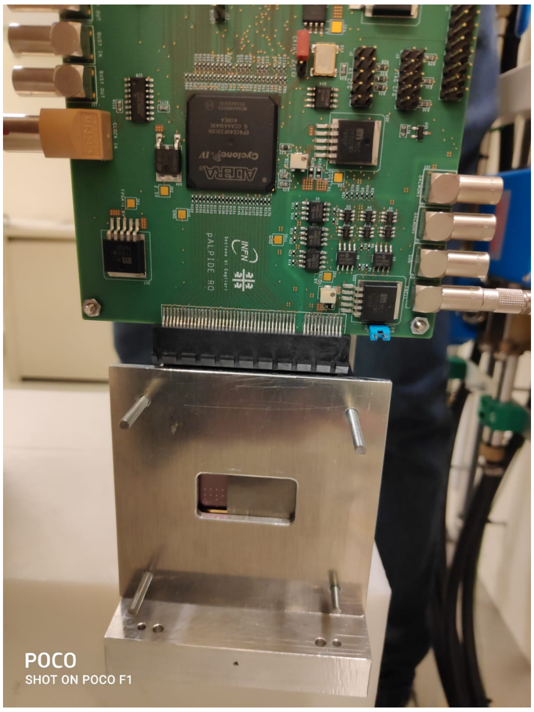

Figure 5.7: A close-up of the metal frame setup with the DAQ board (top) and the Al-plate in front of the ALPIDE carrier board (not visible).

Note that the amount of time spent collecting data was not the total run time of a measurement. The actual (effective) run time was calculated using the total run time and knowing the ON and OFF time intervals of the DAQ, which was 5 ms and 100 ms, respectively. The DAQ spent 5 ms + 100 ms reading and writing data from ALPIDE to the computer. The number of times the DAQ was effectively ON was the ratio between the total run time to (5 ms + 100 ms). Multiplying this by the DAQs effective ON time (5 ms) gave the effective run time

$$T_{eff} = \frac{T_{tot}}{5\,ms + 100\,ms} \cdot 5\,ms \tag{5.2}$$

5.2.2 Data Analysis

A ROOT script was used to visualize the data acquired with ALPIDE. The script generated a hit-map, a column (col) profile, a row profile, and a cluster-size distribution histogram.

The hit-map, a two-dimensional histogram, represented the ALPIDE's pixel matrix where one histogram bin was analogous to a pixel in the matrix. A "hit" was the same as an activated pixel. The hit-map showed pixels activated, and the color hue of the bin indicated the frequency at which a pixel was activated. The hit-maps horizontal axis represented pixel rows, and the vertical axis represented pixel columns.

A column (row) profile, a one-dimensional histogram, displayed the number of hits per second per column (row); it was a one-dimensional profile of the hit-map's horizontal (vertical) axis. The horizontal axis of a col (row) profile showed column (row) address, and the vertical axis showed hit rate per column (row) in units per second ($/s$).

The cluster-size distribution, a one-dimensional histogram, showed how many clusters of a certain size were produced during a measurement. One cluster corresponded to a particle signal in ALPIDE, a particle hit. The size of the cluster was related to the particles energy loss in ALPIDE's sensitive volume. The cluster-size distributions horizontal axis showed cluster sizes in unit pixel, and the vertical axis showed the cluster rate in units "per second per pixel" (/s/p). In the statistic box, "Integral" represented the cluster flux (/s/p) of cluster-size distribution and corresponded to particle hit rate.

The cluster flux was calculated by normalizing cluster entries on effective run time and the number of pixels in the ALPIDE pixel area of interest.

$$\phi = \frac{N'}{n \cdot T_{eff}} \tag{5.3}$$

where n was the number of pixels in the area of interest and N' was the number of clusters registered in that area during the effective run time T_{eff}. Cluster flux was used as a means to compare results of data collected by a specific ALPIDE pixel area. If the data had been collected with the same run time and pixel area, just the number of clusters would have sufficed. However, this was not the case, so N was normalized on time and pixels.

With the cluster flux, the number of registered clusters was extrapolated to ALPIDE's full pixel area for measurements where only a fraction of it was used. This was done by multiplying the cluster flux by the total number of pixels in ALPIDE n_{tot} and the effective run time :

$$N = \phi \cdot n_{tot} \cdot T_{eff} \tag{5.4}$$

Extrapolated cluster number represented the number of particles registered across ALPIDE's full pixel area. Extrapolated cluster numbers were found for the data corresponding to the Gd-covered, Pb-covered, and uncovered ALPIDE pixel areas. These values were used in calculations of the Gd-covered ALPIDE's neutron detection efficiency.

5.2.3 Neutron Detection Efficiency Calculations

The detection efficiency of the Gd-covered ALPIDE was defined as the ratio (in %) of registered neutrons to incident neutrons

$$\varepsilon = \frac{N_n}{N_i} \cdot 100 \tag{5.5}$$

and its uncertainty

$$\sigma_\varepsilon = \sqrt{(\frac{d\varepsilon}{dN_n} \cdot \sigma_{N_n})^2 + (\frac{d\varepsilon}{dN_i} \cdot \sigma_{N_i})^2} \cdot 100\% \tag{5.6}$$

The number of neutrons incident on ALPIDE was calculated based on the thermal-neutron flux measurements made by the neutron survey meter

$$N_i = \Phi \cdot A \cdot T_{eff} \tag{5.7}$$

where A was ALPIDE's pixel area (in cm^2) and Φ was the thermal-neutron flux as measured by the neutron survey meter (in cm^{-2}s^{-1}). The uncertainty of the ALPIDE area was deemed negligible, as its precision is down to the μm.

The number of registered neutrons (N_n) was calculated with the extrapolated cluster number of the Gd-covered, Pb-covered, and uncovered ALPIDE measurement (i.e., N^{Gd} ,N^{Pb}, and $N^{uncov.}$). Henceforth, extrapolated cluster number will be referred to as just cluster, for a simpler approach. Registered neutrons were assumed to be proportional to ICEs detected by ALPIDE

$$N_n = C_1 \cdot N_{ICE} \tag{5.8}$$

where C_1 was a constant describing the ratio of neutron captures to ICEs detected (equation 4.3.2). The number of ICEs detected by ALPIDE was calculated with two methods. For the first method, clusters generated in the ALPIDE area covered by Pb-foil were subtracted from the area covered by the Gd-foil. More specifically, gamma interference in the Gd-foil was corrected for by scaling the observed gamma interference in the Pb-foil to suit Gd. The scaling factor C_2 was used (equation 4.4.3).

$$N_n = C_1(N^{Gd} - C_2 \cdot N^{Pb}) \tag{5.9}$$

For the second method, the signals of the uncovered ALPIDE area were subtracted from the signals coming from the Gd-covered area. This corrected for external gamma rays, but did not take gamma interference with the Gd-foil into consideration.

$$N_n = C_1(N^{Gd} - N^{uncov.}) \tag{5.10}$$

The expression for N_n gives the number of neutrons registered by ALPIDE, had it been fully covered by the Gd-foil. N^{Gd} ,N^{Pb}, and $N^{uncov.}$ were extrapolated cluster numbers of the Gd-covered, Pb-covered, and uncovered ALPIDE measurements. The reason for using two methods was due to a poorly defined background source (which is discussed later in Chapter 6).

Uncertainty of the values used to calculate neutron detection efficiency are listed in Appendix A.

5.3 Results

In this section, results of the measurements are presented, and detection efficiency of the Gd-covered ALPIDE calculated. Data of ALPIDE measurements were visualized with histograms generated by the modified in-house script. The value of interest was cluster flux, which is stated in the cluster-size distributions statistics box as “Integral”. This feature was used to calculate the extrapolated cluster number of the areas of interest, which were the Gd-covered, Pb-covered and uncovered ALPIDE areas. With these, the neutron detection efficiency of the Gd-covered ALPIDE was estimated.

5.3.1 ALPIDE Measurements

The ALPIDE measurement where the cyclotron was OFF, and no neutrons were generated, is shown in Figure 5.8. In col and row profiles, one pixel stood out in the crowd. This pixel, with address (455,492), was considered defect and was filtered out in the preceding data sets.

Remaining results represent the measurements for which the neutrons source was ON.

Figure 5.9 illustrates measurements of ALPIDE without any foil or plastic covering. The hit-map and the col profile revealed a dead-pixel zone, where no hits were registered, in the region between column 991 and 1024. This dead-zone was not spotted in the previously presented data, where the neutron source was OFF, as the total number of hits were too low. The dead-zone was a trend throughout the measurements, and reduced the active pixel area by 512x(1024-991)= 16896 pixels. Hits were evenly distributed across columns and rows. A number of 62320 clusters was registered. These were distributed across a pixel area of 512x991 = 507,392 pixels and resulted in a cluster flux of (2.2±0.05)·10^{-3} $s^{-1}p^{-1}$. The cluster-size distribution ranged up to 80 pixels, was skewed right, and was multi-modal with three peaks. The majority of cluster sizes were smaller than 30 pixels and only a few took on sizes between 30 and 80 pixels. Two of the peaks were located in the range up to 5 pixel and the third and less prominent peak was located at 6 pixels. The multi-modality, peak positions, and range of the cluster-size distribution was similar for the proceeding measurements.

Measurements of the Gd-covered ALPIDE are illustrated in Figure 5.10. In contrast to the previous measurement, the hit distribution was no longer uniform, with more hits on one side of the pixel matrix than the other. In the col profile, the average hit rate per column was greater to the left of column 600 than that to the right. The cluster-size distribution displayed a total of 80288 clusters and were distributed across the full pixel area, yielding a cluster flux of (2.8±0.07)·10^{-3} $s^{-1}p^{-1}$.

The pixel area composed of rows 0-512 and columns 0-600, where the hit rate per column appeared the highest, was the Gd-covered pixel area, and contained 512x600 = 307,200 pixels. For the Gd-covered pixel area, 55776 clusters and a cluster flux of (3.2±0.08)·10^{-3} $s^{-1}p^{-1}$ were observed. The uncovered pixel area constituted columns 600-991 and rows 0-512 and contained a total of 512x(991-600)= 200,192 pixels. The total number of clusters was 24512, which corresponded to a cluster flux of (2.1±0.06)·10^{-3} $s^{-1}p^{-1}$.

Figure 5.11 illustrates the measurement of ALPIDE covered by the Gd-foil and the Pb-foil. As before, the full pixel area constituted 507392 pixels where those in columns 0-600 and rows 0-512 were defined as Gd-covered pixels. The Gd-covered pixel area accumulated 54335 clusters which resulted in a cluster rate of (3.1±0.08)·10^{-3} $s^{-1}p^{-1}$. The col profile displayed a greater hit rate for the Gd-covered columns (0-600). After column 600 the hit rate dropped. This drop indicated the column region where the Gd-foil and Pb-foil interfaced. The location of the Gd-Pb interface was not clearly defined by the col profile, but after column 800, the hit rate evened out. The Pb-covered pixel area was defined as the column region 800-991 and contained 97792 pixels. For the Pb-covered portion of the pixel area there was a total number of 11165 clusters and a cluster flux of (2.0±0.05)·10^{-3} $s^{-1}p^{-1}$.

Figure 5.12 illustrates the measurement of ALPIDE covered by the Gd-foil and the plastic layer. Like the uncovered ALPIDE, the hit rate per column appeared relatively stable over the whole column region, 0-991. The cluster flux was (2.1±0.05)·10^{-3} $s^{-1}p^{-1}$. The results were similar to that of the uncovered ALPIDE measurement (Figure 5.9).

5.3.2 Neutron Detection Efficiency

Inside the plastic cave the neutron survey meter measured a thermal neutron flux of 7000 n/cm^2/s. ALPIDE's surface area, corresponding to 507392 pixels, was 4.2 cm^2 and the effective run time was 57 s ± 1 s. This corresponded to $(1.7 \pm 0.6) \cdot 10^6$ incident neutrons (N_i).

The extrapolated cluster number for the Gd-covered, Pb-covered, and uncovered ALPIDE area were $(9.2 \pm 0.2) \cdot 10^4$, $(5.79 \pm 0.04) \cdot 10^4$, and $(6.2 \pm 0.2) \cdot 10^4$. Given by the first and second method, the number of registered neutrons and the resulting neutron detection efficiency are listed in Table 5.1.

Table 5.1: Neutron detection efficiency (ε) corresponding to the number of registered neutrons (N_n) as obtained by equation (eq.) 5.9 and 5.10.

Eq.	$\boldsymbol{N_n}$	ε **(%)**
(5.9)	$(5.35 \pm 0.17) \cdot 10^4$	**3.19±0.01**
(5.10)	$(2.52 \pm 0.25) \cdot 10^4$	**1.50±0.05**

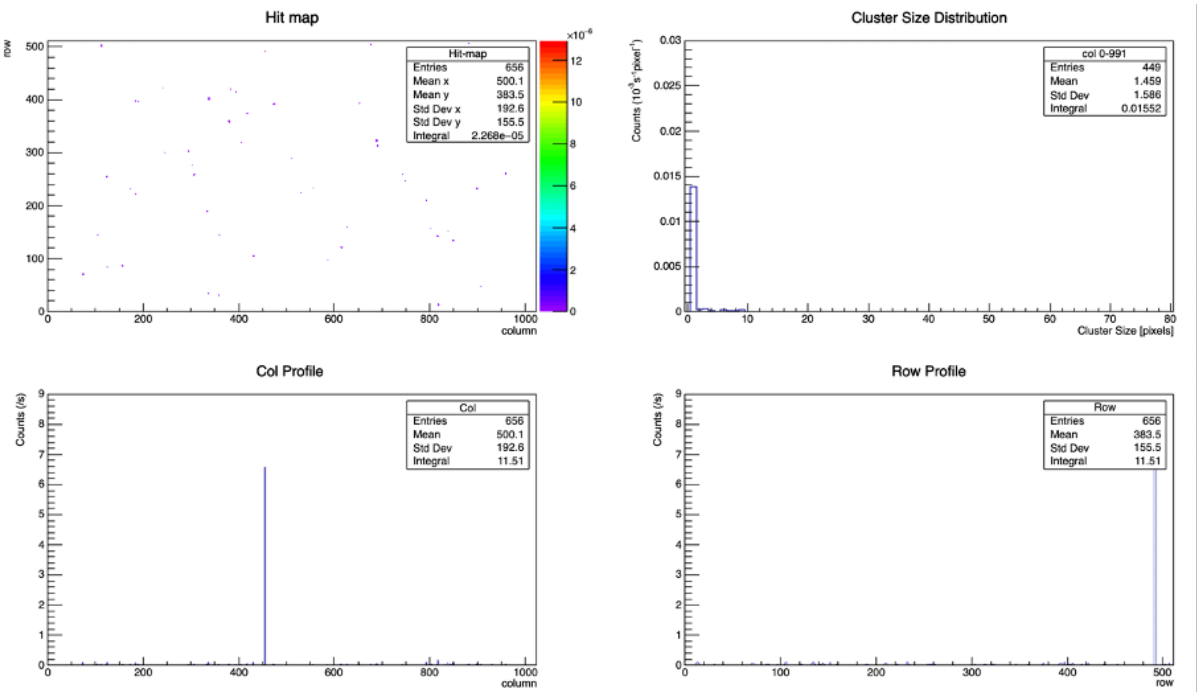

Figure 5.8: Defect pixel (455,492)

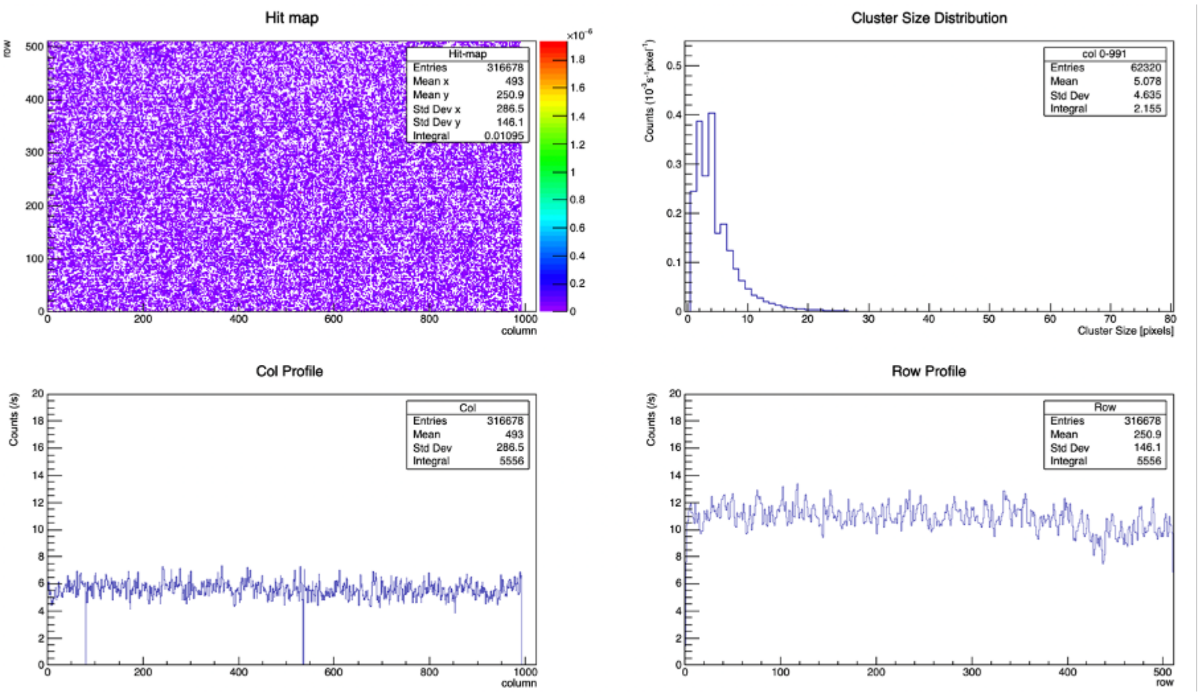

Figure 5.9: ALPIDE exposed to the neutron source without any covering layers.

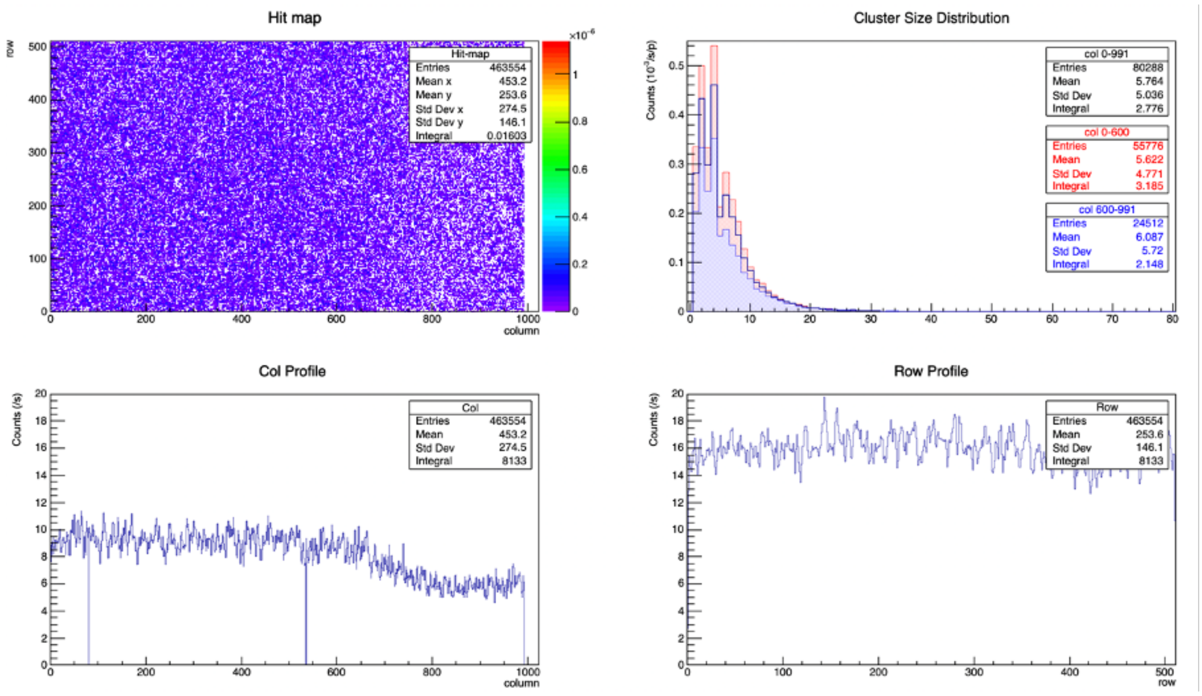

Figure 5.10: Pixels covered by the Gd-foil (left of col 600) displayed a higher hit rate than those who were not (right of col 600).

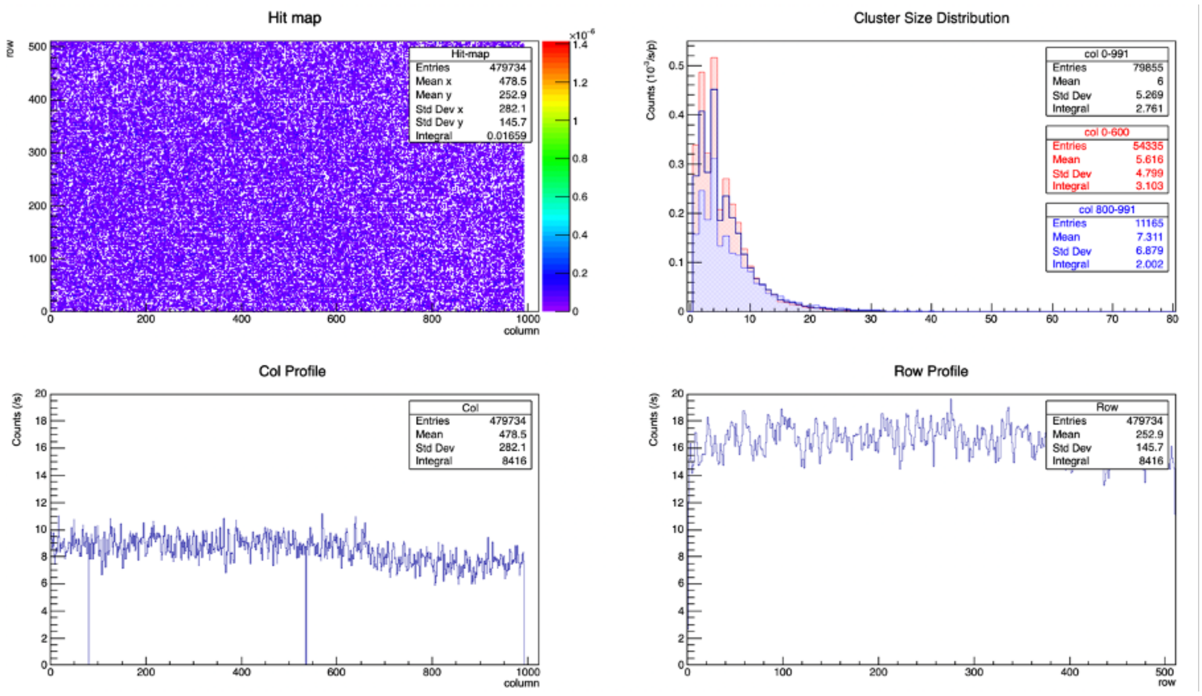

Figure 5.11: Pixels covered by the Gd-foil (left of col 600) displayed a higher hit rate than those who were covered by the Pb-foil (right of col 600).

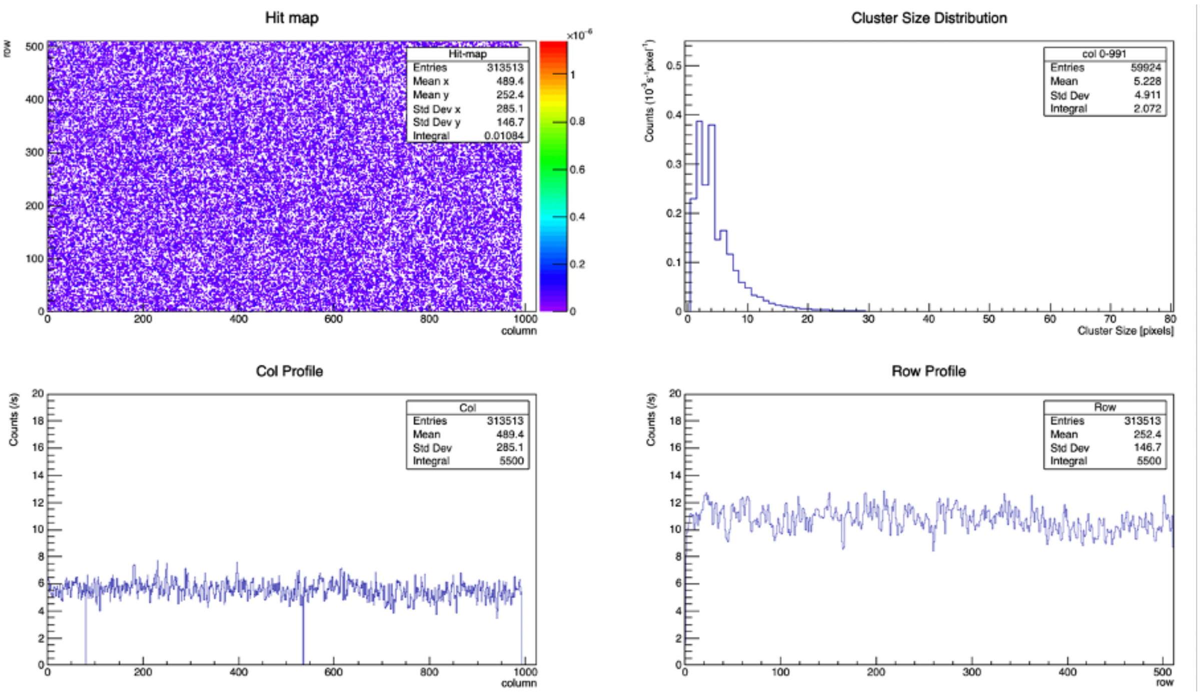

Figure 5.12: Pixels covered by the Gd-foil and the plastic layer (left of col 600) displayed similar hit rate as those who were covered by the the plastic layer only (right of col 600).

Chapter 6

Discussion

6.1 Overview

Neutron-Gd capture results in ICE and prompt-gamma ray emission. Reaction products of neutron capture can generate signals in semiconductor sensors and be used as neutron indicators. In this thesis, the particle sensor ALPIDE coupled with a 25 μm thick Gd-foil was simulated and tested experimentally to investigate ALPIDE's feasibility as a neutron detector. The main findings of the investigations concerned the Gd-based ALPIDE's neutron detection efficiency. The simulations were used to study parameters of the neutron detection efficiency. The highest simulated neutron detection efficiency was achieved for the setup with minimal material between ALPIDE's SD and the Gd-foil, and used a thermal-neutron beam; and the lowest for the setup with the most material separating ALPIDE's SD and the foil, and used an isotropic thermal-neutron source. In the neutron environment of the experimental tests, ALPIDE detected more signals with the Gd-foil than without it. The following sections give an in-depth interpretation of the main findings and other results, and discusses the studies' limitation.

6.2 Analysis

6.2.1 Simulations

The concluded optimal Gd-thickness was 5 μm considering both the front- and back-irradiated ALPIDE, which agree with results obtained in reference [43].

The simulated neutron-captures showed an ICE yield of 0.8 per neutron capture, which is relatively high in comparison to similar studies. K. Pfeiffer reports a simulated ICE yield of 0.66 [44]; and A. Harms and McCormack calculated 0.6 ICEs per neutron capture [26]. The high ICE yield of this thesis was discussed with Geant4 experts, who also confirmed that the physics models, flags, and data used for the simulations were appropriate. The cause of the high ICE yield simulated in this thesis' study is still uncertain.

The simulated prompt-gamma energy distribution did not fit expectations. The most concerning spectrum features were the spectrum line located at 3.7 MeV and the collection of spectrum lines below 1 MeV. These spectrum features do not occur in others simulations of Gd-neutron capture's prompt-gamma spectrum (Figure 3 in reference [45] and Figure 4 in reference [2]). Since the prompt-gamma rays were not the main focus of this work, the simulated spectrum's peculiar features were not investigated further.

The following paragraphs discuss the results of ICE detection in ALPIDE's SD, presented in Figures 4.4-4.12.

In the simulations, neutron captures occurred at all depths of the Gd-foil. The majority of neutrons were captured in the first 10 μm (Figure 4.4), meaning the majority of ICEs were produced in the first 10 μm.

The ideal setup simulated a thinned-down ALPIDE (only the SD) positioned 1 μm near the foil. ALPIDE's SD detected ICEs of all production energies. The production energies observed inside the foil (subplot of Figure 4.6) were also observed by the SD (subplot of Figure 4.9a). However, the number of detected ICEs was notably lower for the latter. The explanation for this is twofold. The first is isotropic ICE emission. The ICEs emitted in the opposite direction of the SD were, for obvious reasons, not detected. Second, ICEs with shorter penetration depths are less likely of emission if they are produced deeper inside the foil. The SD did not detect the ICEs with energies insufficient to escape the foil. The majority of the 29 keV ICEs is one such example. The detected production energy distribution (subplot of Figure 4.10a) clearly demonstrated the 29 keV spectrum line's reduced intensity. The detected ICEs' kinetic energy distribution appeared as a smeared-out version of their production energies (subplot of Figure 4.10a) due to energy loss inside the Gd-foil. The ICEs with lower energies traveling greater Gd-foil distances lost a greater amount of energy. As a result, the ICEs' kinetic energies were degraded, and the detected ICEs' kinetic energy distribution appeared continuous and smeared out. ALPIDE detected fewer ICEs than the thinned-down ALPIDE of the ideal setup, due to the presence of a 11 μm thick aluminum layer which caused energy loss in the ICEs. The penetration depth of 30 keV electrons in aluminum is less than 11 μm [46]. ALPIDE's aluminum layer effectively stopped all the 29 keV ICEs from reaching the

SD, which explains the absence of the 29 keV spectrum line of the detected production energy distribution in subplot of Figure 4.10a. ICEs with energies higher than 30 keV reached the SD, but still, not as many as with the ideal setup. Electron backscattering is another explanation for the reduced ICE count. The phenomenon occurs in aluminum where the percentage of backscattered 60-100 keV electrons lies between 13% and 15% [47]. With the aluminum layer stopping and scattering ICEs, the number of detected ICEs dropped by nearly 50%, compared to what was detected in the ideal setup. The ICEs escaping the aluminum layer did so with a reduced kinetic energy. In comparison to the ideal setup, the detected ICEs' kinetic energy distribution was shifted a few tens of keVs lower due to the energy loss in the aluminum layer (Figure 4.10a vs. Figure 4.9a).

As the electron average energy loss in air is minimal for distances traversed in the mm range [48], moving ALPIDE a couple of mm did not affect peak positions of the detected ICE's kinetic energy spectrum significantly (Figure 4.11a vs. Figure 4.10a). However, it did cause a further reduction in the number of detected ICEs, since the greater air gap increased the probability of ICEs scattering out of ALPIDE's reach.

The detection efficiency relied on the number of detected ICEs. The highest detection efficiency was observed with the ideal setup, where the most ICEs were detected. The detection efficiency shrunk as more material and greater distances were added between the SD and the foil. The lowest detection efficiency was observed when the isotropic thermal-neutron source irradiated ALPIDE. With neutrons coming in from all directions, the neutron-capture profile of the Gd-foil was symmetrical (Figure 4.8); meaning, 50% of the neutron-captures occurred on the foil side closest to ALPIDE and 50% on the side furthest away from ALPIDE. The ICEs produced on the far side were less likely of detection, as these traversed greater distances across the Gd-foil. Since this included half of the produced ICEs (half of the neutrons were captured on the far side), half was essentially lost for the SD. The isotropic thermal-neutron source severely affected the number of detected ICEs and reduced the detection efficiency by nearly 40% compared to what was obtained with the mono-energetic thermal-neutron beam.

Finally, the distributions of the different setups were relatively similar except for the peak amplitudes, which depended on the number and energies of the detected ICEs. In silicon, the projected range of 90-100 keV electrons is 21-26 μm [49]. The ALPIDE's (silicon) SD was 25 μm thick. Most of the ICEs with energies less than 100 keV were stopped and lost all their kinetic energy in the SD; their energy loss distribution (top subplot of Figure 4.9b-4.12b) was very similar to the kinetic energy distribution's peak corresponding to the same energies, up to 100 keV. Majority of the ICEs with energies larger than 100 keV fully penetrated the SD and lost only a small fraction of their kinetic energy. The energy-loss peak located in the lower keVs (bottom subplot of Figures 4.9b-4.12b) resembled the larger-than 100 keV ICEs' incomplete energy deposition. The distribution was Landau-shaped, which is the general case for electrons passing through an absorbing material (2.14).

6.2.2 ALPIDE Measurements

The first ALPIDE measurement had the cyclotron turned OFF and detected few signals. As expected, turning the cyclotron ON significantly increased the number of detected signals. Gammas rays were generated during cyclotron operation and most likely caused the higher signal count, despite ALPIDE's low gamma sensitivity [50].

In the Gd measurements, the Gd-foil covered two-thirds of ALPIDE's pixel area. The Gd-foil edge position was not certain and due to scattering the drop in hit rate per column was not sharp but smooth. Nevertheless, the col profile showed that the rate at which pixels were fired was greater for the Gd-covered ALPIDE area. Also, the cluster flux was higher, which meant that signals were generated at a higher frequency, since a cluster represented a particle hit. The Gd-measurement confirmed that the Gd-foil contributed to an increased number of detected signals in ALPIDE when exposed to thermal neutrons and that it could be used to detect neutrons.

When the Pb-foil was placed over the uncovered ALPIDE area, the hit rate per column increased, but the calculated cluster flux was lower than the cluster flux of the ALPIDE measurement without any foils. This meant fewer signals (clusters) were generated, hence the lower cluster flux; but the size of the cluster produced by each signal was larger (more pixels fired), hence the higher hit rate. The decrease of the signals detected was attributed to the Pb-foil shielding external gamma rays. Photons attenuated in the foil could have contributed to electron production. Low energy electrons generally produce large clusters and activate more pixels in ALPIDE. Thus, with a significant decrease in detected gammas and electrons' detection, the cluster flux would decrease, and the average cluster size would increase.

The gamma simulations, presented in Chapter 4.3 showed that the simulated ALPIDE could detect radiation produced by gamma-ray interactions in the Pb- and Gd-foil. In the simulations, more electrons were emitted from 50 μm Pb than 25 μm Gd. In the experimental measurements, if the electrons registered by ALPIDE had originated from gamma-rays alone, the Pb-covered pixel area would have shown a greater cluster flux. However, the particle flux remained greater on the Gd-covered side. Though this was not the Pb measurement's motivation, it proved that the pixel area under the Gd-foil detected more neutron-generated signals than gamma-generated signals. The true motivation was to correct for gamma-interactions in the Gd-foil. This was done by scaling down the flux observed under the Pb-foil with constant C_2, which was derived from the gamma simulations. Underestimating the constant would mean an overestimate and thus overcorrection of the gamma interference in Gd. Consequently, overestimating the interference would mean the calculated detection efficiency would be lower than actually true.

The measurement results where plastic separated the Gd-foil and ALPIDE was similar to the measurement where only ALPIDE was used and no Gd-foil. This confirmed that the plastic layer effectively stopped radiation emitted from the Gd-foil.

6.2.3 Neutron Detection Efficiency

The experimentally obtained neutron detection efficiencies were lower than any of the simulated. One explanation, the simulated ICE yield was higher than what is stated in literature, causing a higher neutron detection efficiency than those obtained experimentally. Also, the experimental measurements were restricted by an electron charge threshold (specified in Appendix B), meaning that a certain amount of energy had to be deposited in one of ALPIDE's pixels to generate a signal. There was no such threshold in the simulations, and all amounts of energy deposits were registered, leading to a higher neutron detection efficiency with respect to the experimental data. And, the experimental measurements involved a more complex radiation environment, meaning overcorrections of interfering signals could have led to lower experimental neutron detection efficiencies.

Error bars of the simulation studies were relatively small compared to the ALPIDE measurement's. Uncertainties (error bars) of the simulated data were assumed purely statistical, as the systematic error of Geant4 lies with the accuracy of the activated physics models and nuclear data. For the experimental measurements, the neutron survey meter contributed to systematic errors and the cluster counts to statistical errors.

6.3 Limitations

The experiment's most limiting factor was the poorly defined radiation environment. As seen in the simulations, the ALPIDE setup, being flat and two-dimensional, had a neutron detection efficiency dependent on incident neutron angle. The neutron detection efficiency was lower in the isotropic neutron source simulations than any of the simulations using a perpendicular neutron beam. A correction factor for the incident neutron angle could have been approximated with simulations by testing multiple beam directions and normalizing the achieved neutron detection efficiencies on that achieved with a perpendicular beam. The experimental neutron flux was assumed isotropic, but in truth, its parameters, like energy spectrum and direction, were unknown, which made approximating such a correction factor challenging. Due to the neutron source's unknown nature, the experimental measurements were not corrected for various incident neutron angles. Also the gamma flux's features were unknown, which made corrections thereof difficult. Repeating the measurements in a well-defined neutron beam would yield a higher and more accurate neutron detection efficiency. This was not possible due to the Covid situation.

As the ALPIDE's radiation environment was quite complex, a complete analysis of the cluster size distribution would require more studies. However, the cluster size distribution was useful because it provided the registered cluster fluxes, which were used to calculate the Gd-covered ALPIDE's neutron detection efficiency.

Another limitation was time. In the experiment, only one ALPIDE was used. With two ALPIDEs, one on each side of the foil, more ICEs could have been detected, which would have increased the neutron detection efficiency. This was not done due to the shortage of time.

Chapter 7

Conclusion

Several simulations were conducted on neutron-capture in Gd and neutron detection efficiency parameters of a silicon sensor, ALPIDE, coupled with a Gd-foil. The simulations showed that

- nearly 100% neutron capture could be achieved with a 25 μm thick Gd-foil;
- the ideal Gd-foil thickness was 5-10 μm, if using two sensors, one on each side of the foil;
- the number of ICEs per neutron capture was 0.82, and gamma per neutron capture was 5.32.

Simulations also showed that ALPIDE's neutron detection efficiency, when using a 25 μm thick Gd-foil,

- reached a maximum of 18%, when the sensor was thinned down to 25 μm and positioned as close as realistically possible (1 μm) to the Gd-foil;
- was 10%, when ALPIDE's aluminum layer was included;
- was 8%, when ALPIDE was positioned further away from the Gd-foil (2.5 mm);
- was 5%, when an isotropic thermal-neutron source irradiated the Gd-foil.

The silicon sensor known as ALPIDE was designed for particle tracking in high energy physics experiments. ALPIDE is effectively sensitive to charged particles but not to neutrons. The project presented in this thesis was a "proof of principle" study assessing the feasibility of ALPIDE as a neutron detector when coupled with a Gd converter foil. Proof that ALPIDE can detect thermal neutrons was demonstrated by attempting neutron measurements with ALPIDE where one measurement incorporated a Gd-foil, and the other did not. The measurements were distinguishable. The ALPIDE measurements were executed in a poorly defined radiation environment created by a F-18 producing PET cyclotron. The Gd-based ALPIDE's neutron detection efficiency was calculated with two methods which resulted in (3.19±0.01)% and (1.5±0.05)%. The efficiency depended on incident neutron angle. This was not corrected for due to the neutron flux's unknown features.

The results of this thesis indicate the potential of ALPIDE as a neutron detector. The ALPIDE measurements verified neutron detection with a Gd-foil possible, and the simulations enlightened the optimization potential of ALPIDE's neutron detection efficiency.

Outlook

Thinning-down of ALPIDE is currently being looked into, and so far, thicknesses of 30-40 μm have been achieved. For future projects the ALPIDE measurements should be repeated in a neutron beam line using a thinned ALPIDE.

A local research group at UiB is planning the development of a high resolution and a high detection efficiency Gd-ALPIDE based neutron detector for thermal neutron imaging. The detector will consist of multiple Gd-ALPIDE layers which aim to optimize neutron detection efficiency, schematic design in Figure 7.1. The findings of this thesis provide insight regarding the optimization of such a Gd-ALPIDE layered detector's efficiency. Its efficiency would benefit from a 5-10 μm thick Gd-foil and a thinned-down ALPIDE, aluminum front side away from the foil.

A 5 μm Gd-foil roughly captures 50% of neutrons impinging the foil and emits ICEs from both sides with a similar intensity. With two such foils and a thinned-down ALPIDE on both sides of each foil, approximately 100% of the impinging neutrons would be captured and a neutron detection efficiency of 18% might be achieved.

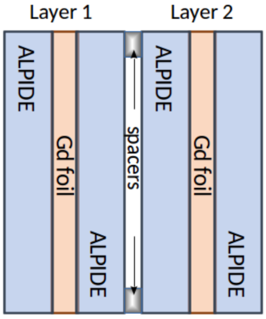

Figure 7.1: Schematic design (not to scale) of two layers of the multi Gd-ALPIDE layered detector aiming to enhance the neutron detection efficiency.

Appendix A

Uncertainty Calculations of Experimental Data

Effective run time:

$$\sigma_{T_{eff}} = \frac{\sigma_{T_{tot}}}{5ms + 100ms} \cdot 5ms \tag{A.1}$$

Cluster flux:

$$\sigma_{\phi} = \sqrt{(\frac{d\phi}{dT_{eff}} \sigma_{T_{eff}})^2 + (\frac{d\phi}{dN'} \sqrt{N'})^2} \tag{A.2}$$

Extrapolated cluster number:

$$\sigma_N = \sqrt{(\frac{dN}{d\phi} \sigma_{\phi})^2 + (\frac{dN}{dT_{eff}} \sigma_{T_{eff}})^2} \tag{A.3}$$

Incident neutrons:

$$\sigma_{N_i} = \sqrt{(\frac{dN_i}{d\Phi} \cdot \sigma_{\Phi})^2 + (\frac{dN_i}{d_{T_{eff}}} \cdot \sigma_{T_{eff}})^2} \tag{A.4}$$

Detection efficiency uncertainty of the first method

$$\sigma_{N_n} = \sqrt{(\frac{dN_n}{dN^{Gd}} \cdot \sigma_{N^{Gd}})^2 + (\frac{dN_n}{dN^{Pb}} \cdot \sigma_{N^{Pb}})^2} \tag{A.5}$$

and the second method

$$\sigma_{N_n} = \sqrt{(\frac{dN_n}{dN^{Gd}} \cdot \sigma_{N^{Gd}})^2 + (\frac{dN_n}{dN^{uncov.}} \cdot \sigma_{N^{uncov.}})^2} \tag{A.6}$$

Appendix B

ALPIDE Configuration File and Noise Threshold Plots

B.1 Configuration File of ALPIDE Measurements

```
VRESETP 0
VRESETD 147
VCASP 86
VCASN 50
VPULSEH 170
VPULSEL 121
VCASN2 62
VCLIP 0
VTEMP 0
IAUX2 0
IRESET 0
IDB 29
IBIAS 64
ITHR 56

MODECONTROL 33
FROMU_CONFIG1 32
FROMU_CONFIG2 1990
FROMU_PULSING1 20
FROMU_PULSING2 500
CMUDMU_CONFIG 48
```

```
FIRMWARE 0x247e0611
TRIGGERDELAY 0
PULSEDELAY 40

NTRIGGERS 50
MASKSTAGES 4096
CHARGESTART 0
CHARGESTOP 50
```

B.2 Threshold and Noise Plots

The ALPIDE chip with ITHR 56 (as stated above) had an average electron charge threshold of 122 electrons (Figure B.1. That is, 122 electrons were needed in one of ALPIDE's pixels for the pixel to register a signal. Without an external radiation source, ALPIDE showed a noise signal where the average cluster size was 4.8 pixels (Figure B.3). Electron charge threshold and noise was distributed evenly across the whole pixel matrix, save small pixel areas which coincided with the location of ALPIDE's interface pads where the noise was slightly greater (Figure B.2 and B.4, respectively).

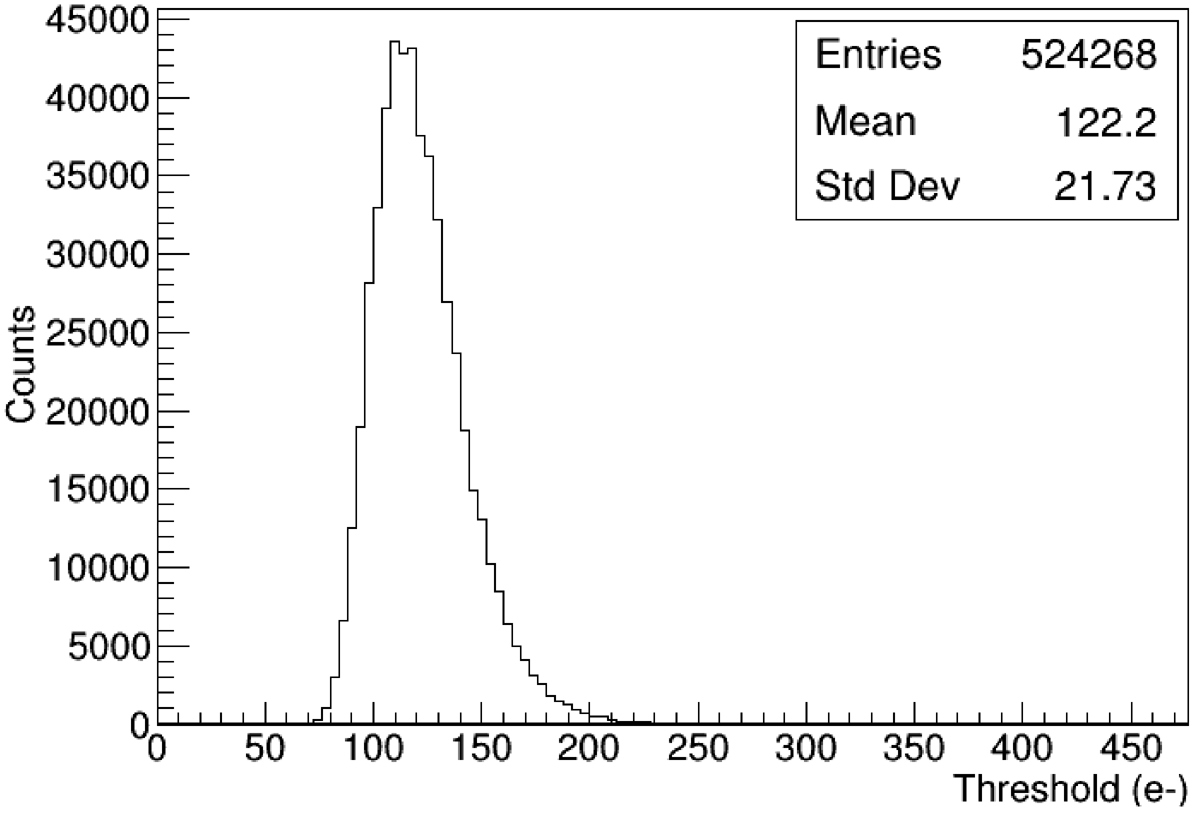

Figure B.1: Electron charge threshold with ITHR 56. Average threshold 122 electrons.

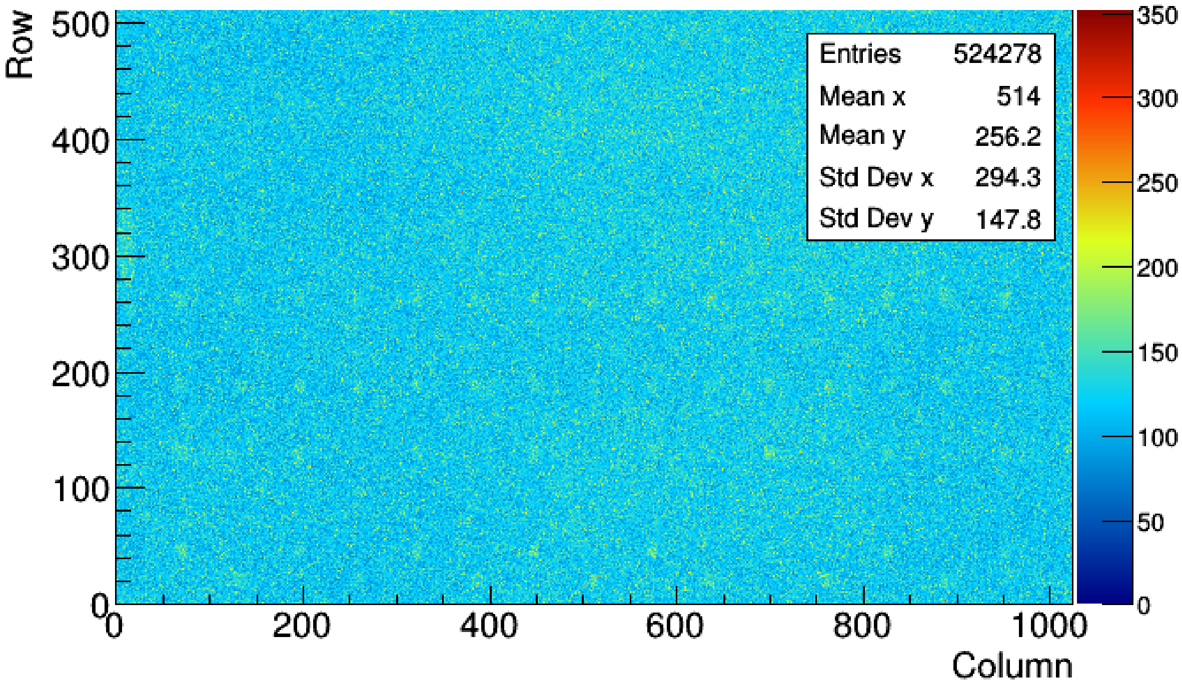

Figure B.2: Electron charge threshold across the pixel matrix. Yellow/Green areas indicate larger threshold and correspond to location of interface pads used for wire bonding.

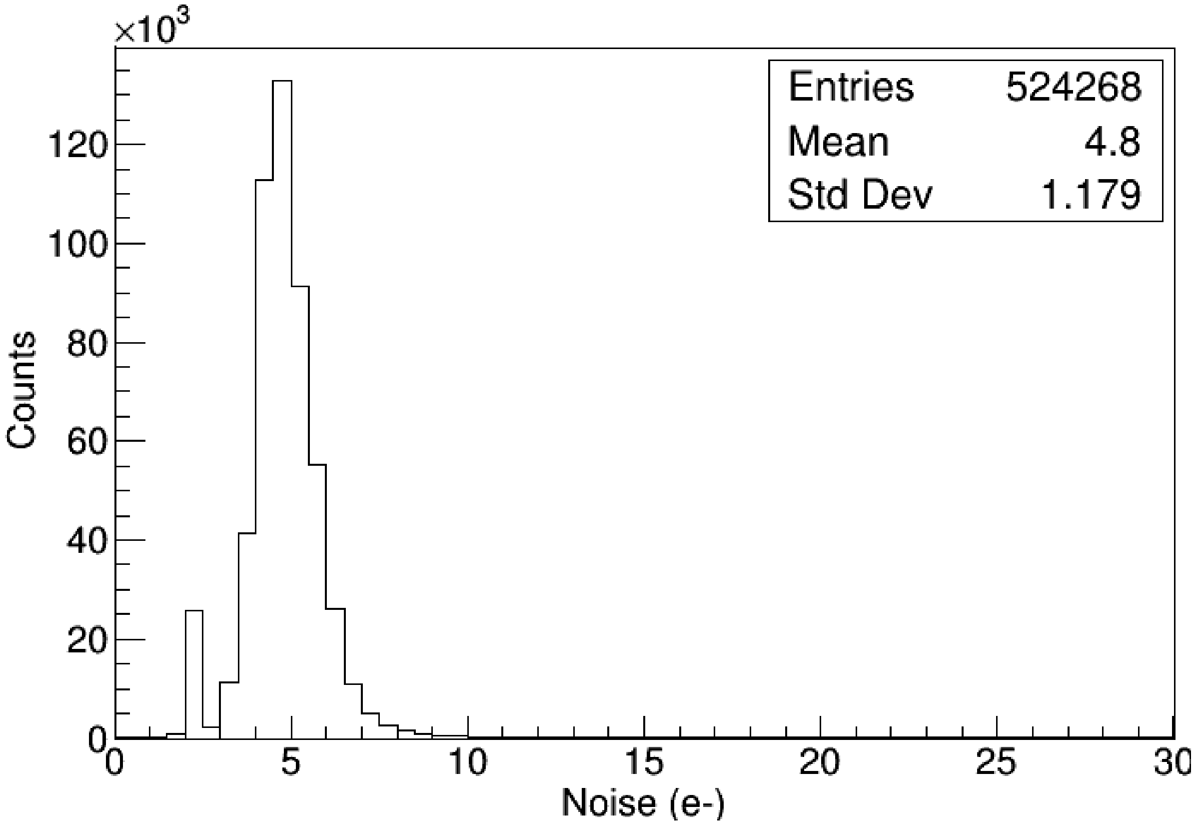

Figure B.3: Cluster size distribution of noise.

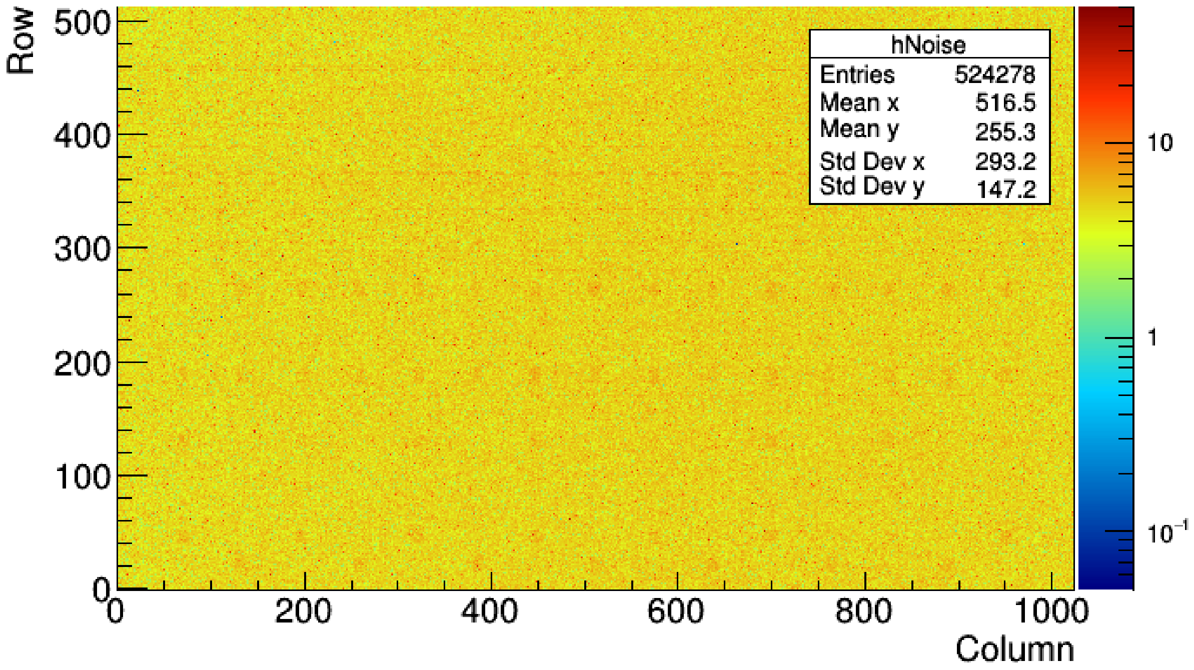

Figure B.4: ALPIDE noise distribution across the pixel matrix. The larger orange areas indicate the location of the interface pads used for wire bonding and show a greater noise signal.

Bibliography

[1] D. A Abdushukurov. *Gadolinium foils as converters of thermal neutrons in detectors of nuclear radiation*. eng. Hauppauge, N.Y., 2010.

[2] J. Dumazert et al. “Gadolinium for neutron detection in current nuclear instrumentation research: A review”. In: *Nuclear Inst. and Methods in Physics Research, A* 882 (2018), pp. 53–68.

[3] Dana A Shea and Daniel Morgan. *The Helium-3 Shortage: Supply, Demand, and Options for Congress*. eng. Library of Congress. Congressional Research Service, 2010.

[4] Gianluca Aglieri Rinella. “The ALPIDE pixel sensor chip for the upgrade of the ALICE Inner Tracking System”. eng. In: *Nuclear instruments & methods in physics research. Section A, Accelerators, spectrometers, detectors and associated equipment* 845 (2017), pp. 583–587. ISSN: 0168-9002.

[5] V.K. Shen et al. *NIST Standard Reference Simulation Website*. Accessed: 2020-10-10. URL: https://physics.nist.gov/PhysRefData/Star/Text/appendix.html.

[6] William R Leo. *Techniques for nuclear and particle physics experiments : a how-to approach*. eng. Berlin, 1994.

[7] Tatjana Jevremovic. “Neutron Physics”. In: *Nuclear Principles in Engineering*. Boston, MA: Springer US, 2009, pp. 281–376. ISBN: 978-0-387-85608-7. DOI: 10.1007/978-0-387-85608-7_7. URL: https://doi.org/10.1007/978-0-387-85608-7_7.

[8] N. Soppera et al. *JANIS 4: An Improved Version of the NEA Java-based Nuclear Data Information System*. The CENDL-3.2, ENDF/B-VIII.0 and IRDFF-II Nuclear Data Library. 2014. URL: http://www.oecd-nea.org/janisweb/book/neutrons/.

[9] Tatjana Jevremovic. “Nuclear Theory”. In: *Nuclear Principles in Engineering*. Boston, MA: Springer US, 2009, pp. 71–113. ISBN: 978-0-387-85608-7. DOI: 10.1007/978-0-387-85608-7_3. URL: https://doi.org/10.1007/978-0-387-85608-7_3.

[10] Kaito Hagiwara et al. "Gamma-ray spectrum from thermal neutron capture on gadolinium-157". eng. In: *Progress of Theoretical and Experimental Physics* 2019.2 (2019). ISSN: 2050-3911.

[11] Walter D Loveland et al. *Modern Nuclear Chemistry*. eng. New York: John Wiley & Sons, Incorporated, 2017. ISBN: 9780470906736.

[12] Glenn F Knoll. *Radiation detection and measurement : Glenn F. Knoll*. eng. New York, 2000.

[13] T Tabata et al. "An empirical equation for the backscattering coefficient of electrons". eng. In: *Nuclear instruments & methods* 94.3 (1971), pp. 509–513. ISSN: 0029-554X.

[14] Syed Naeem Ahmed. *Physics and Engineering of Radiation Detection*. eng. San Diego: Elsevier Science & Technology, 2007. Chap. 2. ISBN: 9780120455812.

[15] Nick Connor. *Total photon cross sections*. 2019. URL: `https://www.radiation-dosimetry.org/wp-content/uploads/2019/12/total_photon_attenuation.png`.

[16] Ervin B Podgorsak. *Radiation Physics for Medical Physicists*. eng. Cham, 2016.

[17] *PN Junction Diode*. URL: `https://www.electronics-tutorials.ws/diode/diode_3.html`.

[18] A Lorenz. *Review of neutron detection methods and instruments*. eng. Lawrence Livermore Laboratory, 1973.

[19] S.R Messenger et al. "Nonionizing energy loss (NIEL) for heavy ions". eng. In: *IEEE transactions on nuclear science* 46.6 (1999), pp. 1595–1602. ISSN: 0018-9499.

[20] S Kushpil. "Characterization of ALPIDE Monolithic Active Pixel Sensor for the ALICE Inner Tracking System Upgrade Using the PS Facility at CERN". In: (2018), 8532940. 4 p. DOI: `10.1109/NSSMIC.2017.8532940`. URL: `https://cds.cern.ch/record/2672113`.

[21] Miljenko Šuljić et al. "Monte Carlo simulation of charge collection processes in Monolithic Active Pixel Sensors for the ALICE ITS upgrade". In: *Nucl. Instrum. Meth. A* 950 (2020), p. 162882. DOI: `10.1016/j.nima.2019.162882`.

[22] Simon Kristian Huiberts. *Characterization of the ALPIDE chip with Helium-4 ions for Proton Computed Tomography*. eng. 2018.

[23] ALICE ITS ALPIDE development team. *ALPIDE operational manual*. 2016. URL: `http://www-subatech.in2p3.fr/~electro/projets/alice/dimuon/mft/pdf/ALPIDE-4-operations-manual_draft20160601.pdf`.

[24] Miljenko Suljic. "Study of Monolithic Active Pixel Sensors for the Upgrade of the ALICE Inner Tracking System". Presented 02 Feb 2018. Nov. 2017. URL: `https://cds.cern.ch/record/2303618`.

[25] Yoshinori Sakurai and Tooru Kobayashi. “Experimental Verification of the Nuclear Data of Gadolinium for Neutron Capture Therapy”. eng. In: *Journal of Nuclear Science and Technology: Proceedings of the International Conference on Nuclear Data for Science and Technology* 39.sup2 (2002), pp. 1294–1297. ISSN: 0022-3131.

[26] A.A Harms and G McCormack. “Isotopic conversion in gadolinium-exposure neutron imaging”. eng. In: *Nuclear instruments & methods* 118.2 (1974), pp. 583–587. ISSN: 0029-554X.

[27] J Allison et al. “Geant4 developments and applications”. eng. In: *IEEE transactions on nuclear science* 53.1 (2006), pp. 270–278. ISSN: 0018-9499.

[28] J Allison et al. “Recent developments in Geant4”. eng. In: *Nuclear instruments & methods in physics research. Section A, Accelerators, spectrometers, detectors and associated equipment* 835.C (2016), pp. 186–225. ISSN: 0168-9002.

[29] S Agostinelli et al. “Geant4—a simulation toolkit”. eng. In: *Nuclear instruments & methods in physics research. Section A, Accelerators, spectrometers, detectors and associated equipment* 506.3 (2003), pp. 250–303. ISSN: 0168-9002.

[30] *Geant4*. Accessed: 2020-10-30. URL: `https://geant4.web.cern.ch/`.

[31] *ROOT Data Analysis Framework*. Accessed: 2020-10-30. URL: `https://root.cern.ch/`.

[32] *The Budapest Research Reactor*. Accessed: 2020-10-23. URL: `https://www.bnc.hu/BRR`.

[33] *The JEEP II Reactor*. Accessed: 2020-10-23. URL: `https://ife.no/en/laboratory/jeep-ii-reactor-at-kjeller-norway/`.

[34] *The JEEP II Reactor Shutdown Announcement*. Accessed: 2020-10-23. URL: `https://ife.no/forskningsreaktoren-pa-kjeller-stenges/`.

[35] Roberto Méndez Villafañe et al. “Study of the neutron field in the vicinity of an unshielded PET cyclotron”. In: *Physics in medicine and biology* 50 (Dec. 2005), pp. 5141–52. DOI: `10.1088/0031-9155/50/21/013`.

[36] N. E. Hertel et al. “Neutron measurements in the vicinity of a self-shielded pet cyclotron”. In: *Radiation Protection Dosimetry* 108.3 (Feb. 2004), pp. 255–261. ISSN: 0144-8420. DOI: `10.1093/rpd/nch026`. eprint: `https://academic.oup.com/rpd/article-pdf/108/3/255/4519167/nch026.pdf`. URL: `https://doi.org/10.1093/rpd/nch026`.

[37] Khalil Amgarou et al. “Neutron spectrometry in a PET cyclotron with a Bonner sphere system”. In: *Radiation protection dosimetry* 126 (June 2007), pp. 371–5. DOI: `10.1093/rpd/ncm077`.

[38] R Pevey et al. “Shielding for a cyclotron used for medical isotope production in China”. In: *Radiation protection dosimetry* 115 (Feb. 2005), pp. 415–9. DOI: 10.1093/rpd/nci206.

[39] M.A.S. Lacerda et al. “Use of the MCNPX to calculate the neutron spectra around the GE-PETtrace 8 cyclotron of the CDTN/CNEN, Brazil”. In: *Applied Radiation and Isotopes* 83 (2014). Proceedings of the XIII International Symposium. XXIII National Congress on Solid State Dosimetry. Ocoyoacac, Mexico, October 15 – 19, 2012, pp. 235–241. ISSN: 0969-8043. DOI: https://doi.org/10.1016/j.apradiso.2013.07.022. URL: http://www.sciencedirect.com/science/article/pii/S0969804313003126.

[40] Yoshimune Ogata et al. “Distribution of Thermal Neutron Flux Around a PET Cyclotron”. eng. In: *Health physics (1958)* 100.5 Suppl 2, Operational Radiation Safety (2011), S60–S66. ISSN: 0017-9078.

[41] Jan Olof Bergström. *PETtrace - Unsheilded machine: summary of source terms, radiation fields and radwaste production (2004)*. eng. Revision 0.4. 2004.

[42] *"Iinstruction Manual for Neutron Survey Meter Model 488A"*.

[43] P. Kandlakunta and L.R. Cao. “Neutron conversion efficiency and gamma interference with gadolinium”. In: *Journal of Radioanalytical and Nuclear Chemistry* 300(3) (2014), pp. 953–961.

[44] D. Pfeiffer et al. “First measurements with new high-resolution gadolinium-GEM neutron detectors”. In: *JINST 11 P05011* (2016).

[45] Praneeth Kandlakunta and Lei Cao. “Gamma-ray rejection, or detection, with gadolinium as a converter”. In: *Radiation Protection Dosimetry* (Mar. 2012). DOI: 10.1093/rpd/ncs031.

[46] F. Lukiyanov et al. “Depth range of primary electrons, electron beam broadening, and spatial resolution in electron-beam studies”. In: *Bulletin of the Russian Academy of Sciences: Physics* 73 (Apr. 2009), pp. 441–449. DOI: 10.3103/S1062873809040029.

[47] E H Darlington. “Backscattering of 10-100 keV electrons from thick targets”. In: *Journal of Physics D: Applied Physics* 8.1 (Jan. 1975), pp. 85–93.

[48] M.J. Berger et al. *ESTAR, PSTAR, and ASTAR: Computer Programs for Calculating Stopping-Power and Range tables for Electrons, Protons, and Helium Ions*. 2019. URL: https://www.nist.gov/pml/stopping-power-range-tables-electrons-protons-and-helium-ions.

[49] Orhan Gürler et al. “Calculation of Projected Range of Electrons in Some Elemental Solids and Gases”. eng. In: *Japanese Journal of Applied Physics* 44.12 (2005), pp. 8630–8634. ISSN: 1347-4065.

[50] F. Colamaria et al. “Study of the photon rejection of the ALPIDE pixel detector for medical applications”. In: *2019 IEEE 8th International Workshop on Advances in Sensors and Interfaces (IWASI)*. 2019, pp. 1–6. DOI: 10.1109/IWASI.2019.8791306.